Imaging the cochlear response to injury

Dr Phillip James Patrick Sale

MBBS(Hons), BMedSci

Submitted in total fulfilment of the requirements of the degree of Doctor of Philosophy

Department of Otolaryngology, Faculty of Medicine

University of Melbourne

Australia

October 2019

Thesis Summary

There are many sites and methods of therapeutic interventions in the ear, but common to most, if not all of them is the risk of degradation of cochlear or vestibular function. This is despite the fact that these interventions are designed particularly to aid function of these organs.

The principal aim of this thesis is to explore non-destructive methods of examining the cochlea's response to attempted therapeutic interventions. Conventional histopathological techniques that have formed the basis of cochlear research over past decades involve potential disruption of anatomical relationships, distortion of fine structures and a lack of a 'whole cochlear' picture of the pathological response.

Three imaging modalities were selected that were either novel to hearing research or had previously been limited only to descriptive anatomical studies. These imaging techniques were combined with therapeutic interventions that in the clinical setting have the potential to improve or augment hearing.

The first experiment of this thesis demonstrated that while continuous drug delivery to the round window membrane may achieve its primary endpoint (BDNF drug effect in the cochlea, in this case), the technique itself involves a risk of cochlear injury which may limit the safety and thus utility of this delivery technique. A combination of destructive and non-destructive imaging techniques was utilised to explore the pathophysiology of this injury.

The second experiment investigated the capabilities of heavy-metal augmented μCT in assessing the cochlea's response to implant insertion through

characterisation of cochlear endolymphatic hydrops, intrascalar tissue response, changes in vestibular end organ volumes and three-dimensional assessment of implant position. A number of techniques were developed that have been utilised in already published research as well as forming the basis of future study.

The third experiment investigated the capability of an emerging imaging technique, TSLIM, to provide more than just anatomical information. With the idea that changes in vascular permeability in the lateral wall of the cochlea may be responsible for changes in scala media observed in Experiment 2, we developed a technique to visualise the permeability of the blood-labyrinthine barrier with spatial resolution sufficient to demonstrate differential vascular permeability in the fibrocyte subregions of the lateral cochlear wall. Furthermore, this technique could be applied to image these changes in the whole cochlea in one instance.

The results and techniques presented in this thesis will inform hearing and other researchers of the applicability of these imaging techniques to their research questions to push hearing research beyond histopathology and the mid-modiolar section.

Declaration

This is to certify that:

1. *(i) This thesis comprises only my original work towards my PhD except where indicated in the Preface*
2. *(ii) Due acknowledgement has been made in the text to all other material used*
3. *(iii) This thesis is less than 100,000 words in length, exclusive of tables, bibliographies and appendices*

Preface

The following unchanged multi-author paper was included in this thesis:

Sale PJP, Uschakov A, Saief T, Rowe DP, Abbott CJ, Luu CD, Hampson AJ, O'Leary SJ, Sly DJ (2017). Cannula-based drug delivery to the guinea pig round window causes as lasting hearing loss that may be temporarily mitigated by BDNF. Hear Res. 2017; 356: 104-115. DOI: 10.1016/j.heares.2017.10.004.

- In addition to fulfilling the criteria for authorship, I would like to acknowledge the contributions of: AO with LSCM, TS with whole-mount dissections, DR with animal surgery, CA, CL with OCT, DS with auditory testing and concept, SOL with analysis and AH with animal care and editing.

With regards to other experiments included in this thesis, I would like to acknowledge:

Experiment 2 – Dr Henrik Smeds for animal surgery, Amy Hampson for animal care and electrophysiology, Stephanie Mansour for Amira work, Dr Benedicta Arhatari for μCT advice and setup, Dr Luke Campbell for Matlab coding, Helen Feng for electrode manufacture, Dr Hayden Eastwood for μCT processing.

Experiment 3 – Dr Luke Campbell for Matlab coding and instrument control coding, Amy Hampson for animal care and surgery, Dr David Rowe for animal surgery and Dr Jonathon Lo for TSLIM assistance.

Acknowledgement

This thesis could not have been completed without the ongoing support of supervisors and colleagues within the Department of Otolaryngology.

More specifically, thank you to Professor Stephen O'Leary, Professor Mark Cook and Dr David Sly for their supervision of this thesis. Heartfelt thanks to Dr Hayden Eastwood for guidance and insight into the research process. Thank you to Dr Nathan Creber, Dr Luke Campbell, Dr Jonathon Lo, Dr David Rowe, Amy Hampson, Scott Chambers, Rodney Millard, Dr Aaron Uschakov and Prue Nielsen for their ceaseless assistance and unique skillsets.

I would like to gratefully acknowledge the financial support received from the Surgeon Scientist Programme supported by the Garnett Passe and Rodney Williams Memorial Foundation.

Table of contents

List of Figures

List of Tables

List of Abbreviations Used

LSCM LASER Scanning Confocal Microscopy

TSLIM Thin-Sheet LASER Imaging Microscopy

µCT Micro Computed Tomography

RWM Round Window Membrane

ABR Auditory Brainstem Response

MRI Magnetic Resonance Imaging

ROS Reactive Oxygen Species

CCD Charge Coupled Device

CMOS Complementary Metal Oxide Semiconductor

LSFM Light Sheet Fluorescence Microscopy

MAR Metal Artefact Reduction

FBP Filtered Back Projection

OCT Optical Coherence Tomography

AP Artificial Perilymph

BDNF Brain Derived Neurotrophic Factor

SP Summating Potential

CAP Compound Action Potential

RGBa Red/Green/Blue/alpha

OSL Osseous Spiral Lamina

SS-OCT Swept Source Optical Coherence Tomography

TD-OCT Time Domain Optical Coherence Tomography

SD-OCT Spectral Domain Optical Coherence Tomography

FD-OCT Frequency-Domain Optical Coherence Tomography

BLB Blood-Labyrinthine Barrier

EP Endocochlear Potential

IR Iterative Reconstruction

TEM Transmission Electron Microscopy

1 Introduction

1.1 Concept

There are many sites and methods of therapeutic interventions in the ear, but common to most of them is the risk of degradation of cochlear or vestibular function. This is despite the fact that these interventions are designed particularly to aid function of these organs. Intratympanic injection of gentamicin to ablate the vestibular organs in Mèniére's Disease may cause unintended damage to cochlear function (King, Salt, Kel, Eastwood, & O'Leary, 2013). Stapedotomy for hearing-restoration in otosclerosis may cause a profound sensorineural hearing loss (Ruhl, Hong, & Littlefield, 2013). Introduction of a cochlear implant electrode to restore hearing may destroy residual native hearing (Burghard, Lenarz, Kral, & Paasche, 2014; S. J. O'Leary, Monksfield, Kel, Connolly, Souter, Chang, Marovic, O'Leary, Richardson, & Eastwood, 2013a). These, and other, unexpected consequences of therapeutic interventions are the subject of this thesis.

A decrease in the mobility of the round window membrane (RWM) can have significant effects on hearing both in humans (T. E. Linder, Ma, & Huber, 2003) and other animals (Nageris, Attias, Shemesh, Hod, & Preis, 2012). With significant efforts being made to utilise the RWM as a conduit for drug delivery, the finding by Nordang, et al (2003), that application of glucocorticoids to the RWM can cause significant thickening of the membrane is concerning. We will examine the effects of alternative RWM drug delivery techniques on the anatomy of the RWM and hearing for this reason.

Endolymphatic hydrops after cochlear implantation has been recognised in the past (Handzel, Burgess, & Nadol, 2006), but the relationship of hydrops to hearing-preservation and other pathological changes after cochlear implantation is not clear. Extending the assessment of hydrops, tissue-response and electrode position into the third dimension could provide indications as to the relevance of this injury-response to prevention of further hearing loss after cochlear implantation.

Animal models of endolymphatic hydrops would suggest that one factor involved in generation of hydrops is breakdown, or alteration of function in the stria vascularis and its blood-labyrinthine-barrier. Further evidence for this link has been identified using MRI (Tagaya et al., 2010), but the spatial resolution of MRI means that the exact site and mechanism of this contribution to hydrops is not well-defined. More detailed spatial information needs to be obtained to determine that vascular permeability in the lateral wall of the cochlea is part of the response to cochlear implantation that results in endolymphatic hydrops.

This review will focus on several responses to trauma in the inner-ear apparatus that could be responsible for inadvertent, iatrogenic degradation of hearing secondary to therapeutic procedures in the ear. Furthermore, conventional and contemporary methods of imaging of the ear will be examined and their utility in the identification and quantification of otopathology discussed in the context of developing new techniques for three-dimensional imaging of iatrogenic injury.

1.2 Cochlear Injury

1.2.1 Relevant Anatomy and Physiology

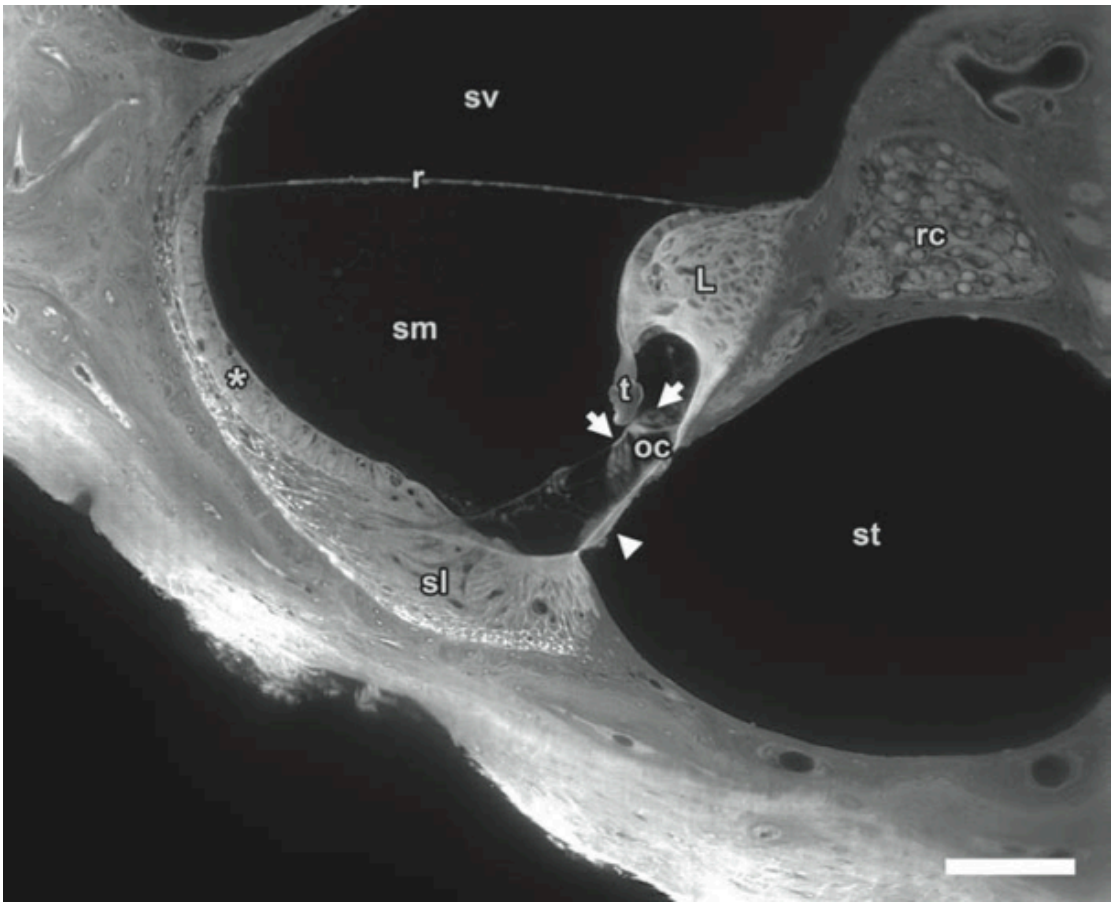

Figure 1-1 - TSLIM image of the scala media and associated structures. Adapted from Buytaert, et al (2013).

1.2.1.1 Endolymphatic and Perilymphatic Scalae

The three fluid spaces of the cochlea are the scala vestibuli, scala media and scala tympani. The scala media is the endolymph-filled fluid-space of the cochlear duct, containing the organ of Corti and supporting structures that transduce mechanical energy from pressure waves induced in the adjacent perilymph into electrochemical movements across the membranes of the sensory hair cells.

Endolymph is a positively charged (+80-90mV) fluid with a high concentration of potassium ions (150mM). The potential difference across the hair-cell membrane is increased further by the negative-charge of the intracellular fluid of the hair cells (-50mV). This large electrochemical gradient provides the impetus for rapid influx of potassium ions when tip-linked ion channels are actuated by mechanical distortion of the cochlear duct (Wangemann, 2006). Endolymph is produced primarily by the stria vascularis in the lateral cochlear wall, but additional sites of production within the vestibular organs are proposed (Ciuman, 2008).

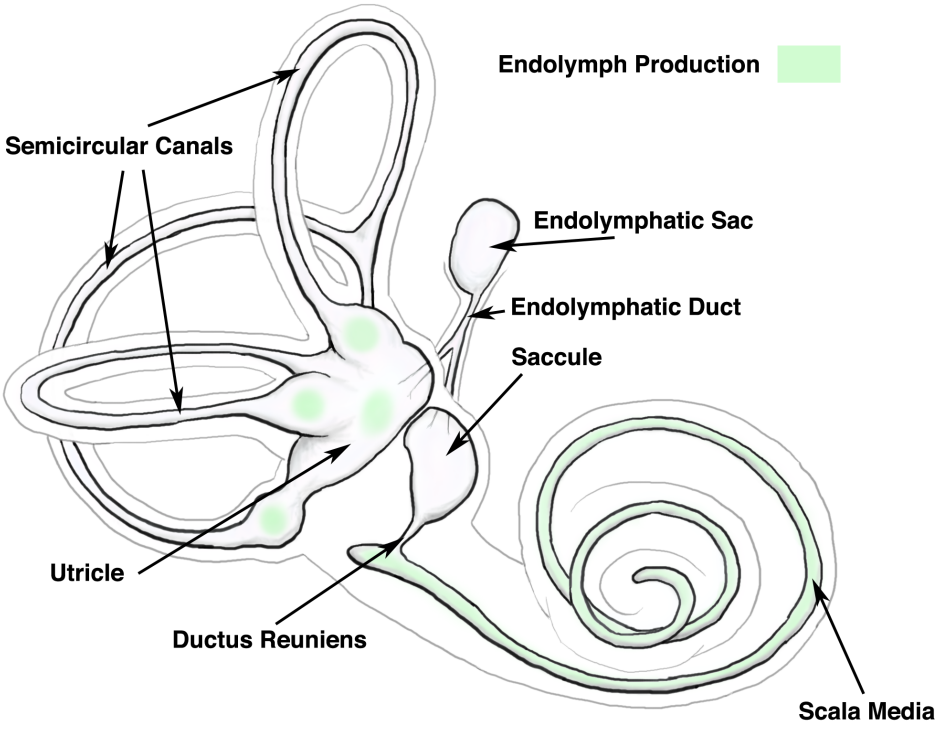

Figure 1-2 - Membranous labyrinth, demonstrating known and likely sites of endolymph production.

The scala vestibuli and tympani contain perilymph, which is similar in makeup to extracellular fluid elsewhere in the body. Perilymph fills these spaces, which

communicate through a small channel at the helicotrema, as well as bathing the endolymph-containing membranous labyrinth of the vestibular organs.

1.2.1.2 Round Window Membrane

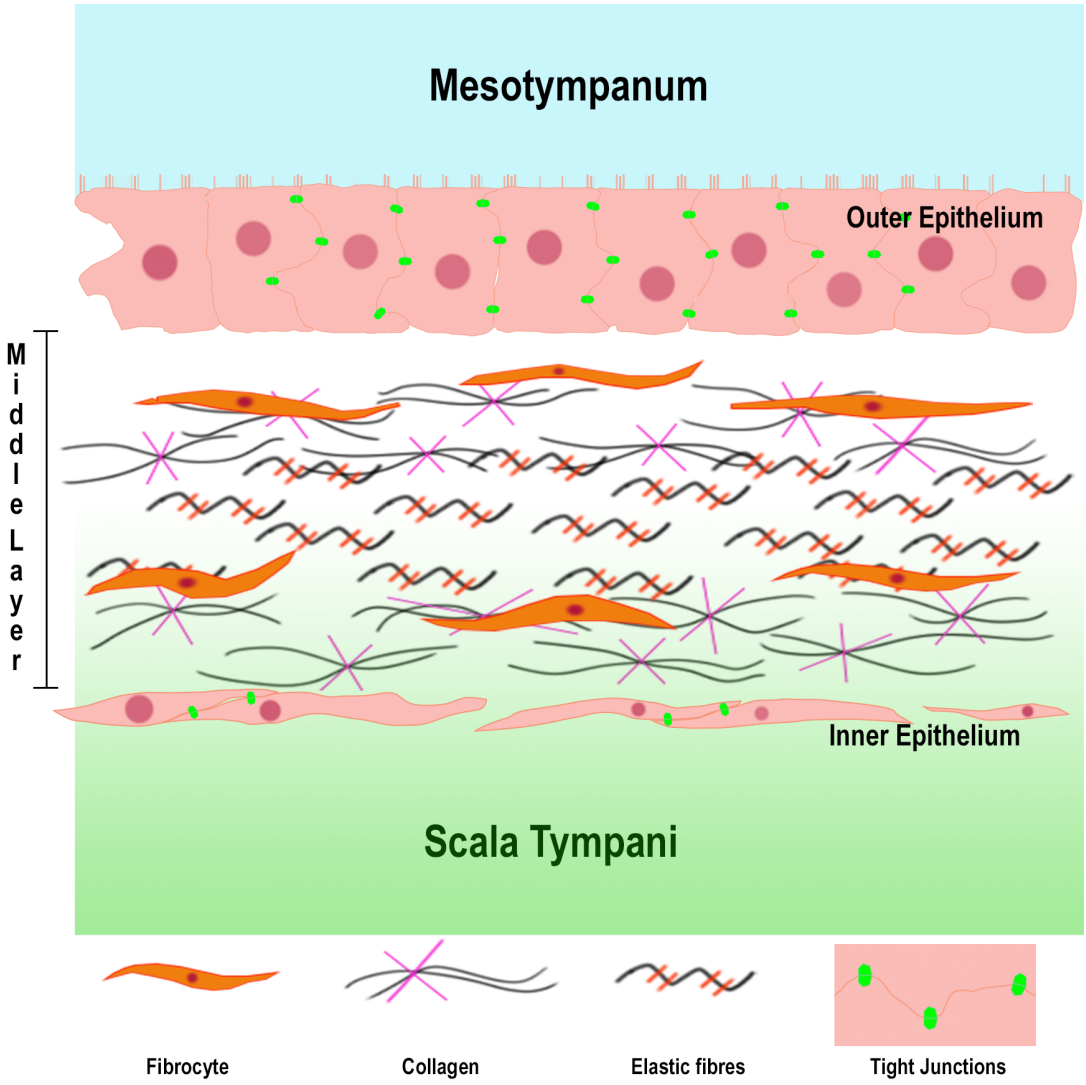

Figure 1-3 - Cross-section through the central portion of the mammalian Round Window Membrane

The round window membrane (RWM) (Figure 1-3) is a three-layered structure separating the perilymph of the scala yympani from the middle-ear cavity. The middle ear surface of the membrane consists of a low-cuboidal epithelium with extensive interdigitations, microvilli and large numbers of tight junctions. The

interdigitations mean that the epithelium is described in different texts as having one or two layers (Hellström, Johansson, & Anniko, 1988; Lundman, Bagger-Sjoback, Holmquist, & Juhn, 1989). The middle-layer of the RWM consists of collagen, elastin and fibroblasts. Blood and lymphatic vessels are sparse in the central portion of the membrane. The scalar surface is a squamous endothelium with tight-junctions between adjacent endothelial processes. The cells are only loosely organised, with large intercellular intervals allowing perilymph contact with the middle, fibrous layer of the RWM. The outer layer thus provides most competent barrier and is permeable to small particles such as horseradish peroxidase (described later), but not albumin in a state of health (Hellström et al., 1988). The rim of the RWM at its insertion into the bony niche is thicker than the centre of the membrane and contains further blood vessels, lymphatics, macrophages and small glandular structures emptying onto the external surface (Engmér, Laurell, Bagger-Sjöbäck, & Rask-Andersen, 2008).

The RWM provides a method of pressure-relief from the scala tympani to facilitate the transduction of movement of the stapes footplate into basilar membrane displacement along the tonotopically organised organ of Corti. Absence or impairment of this pressure-relief mechanism has a significant impact on cochlear conductive function (see *Disruption of cochlear mechanics*).

1.2.1.3 Lateral Cochlear Wall

The lateral cochlear wall refers to the site of attachment of the basilar membrane and Reissner's membrane to the lateral wall of the cochlea, as well as the spiral ligament (Figure 1-1sl) and stria vascularis (Figure 1-1- *). The stria vascularis

is a three-layered structure key to the production of endolymph, formation of the blood-labyrinthine-barrier (BLB) and maintenance of the endocochlear potential (EP). The three layers of the stria vascularis from the endolymphatic surface are the marginal (Figure 1-4 – 'M'), intermediate (Figure 1-4 – 'I') and basal (Figure 1-4 'B') cell layers. Both the marginal and basal layers have large numbers of intercellular tight-junctions that limit paracellular permeability. The intermediate cells are joined to the basal layer and each other by gap junctions (Figure 1-4 – 'G') made up largely of connexins 26 and 30 (Cohen-Salmon et al., 2007).

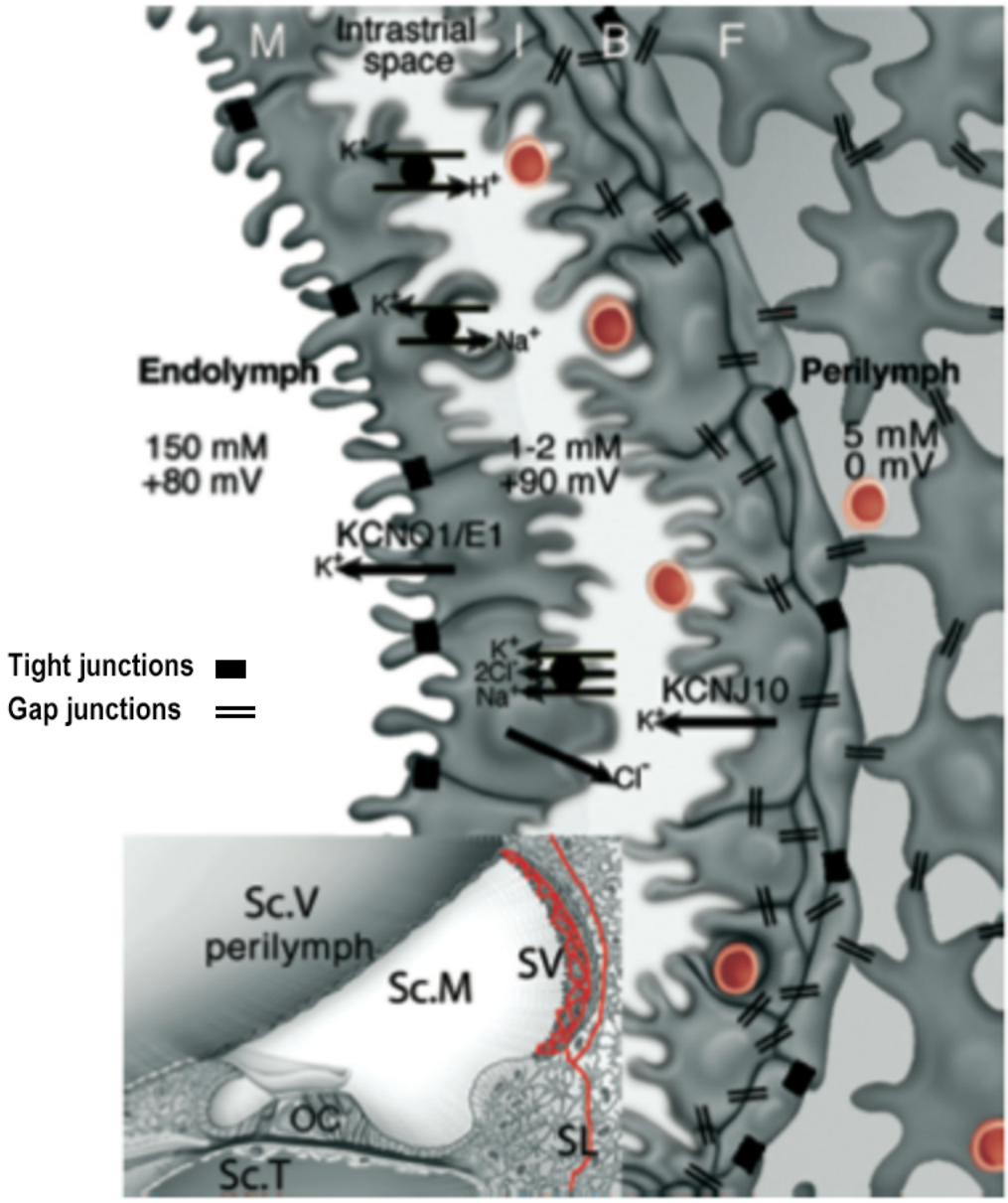

Figure 1-4 - From Cohen-Salmon, et al (2007). Generation of the EP across the stria vascularis. Numbers in mM and mV refer to the concentration of Potassium ions and the electrochemical potential, respectively.

Between the intermediate and marginal layers is the intrastrial space, containing large numbers of strial capillaries surrounded by their pericytes and processes of perivascular-resident macrophage-type melanocytes (Figure 1-4 and Figure 1-5) that together make up the BLB. The BLB is important in maintaining the

isolation of the Intrastrial space from blood, whilst still allowing blood delivery to these metabolically demanding tissues. The EP is formed at the intermediate surface of the intrastrial space through active transport of potassium ions into the Intrastrial space. Potassium is then actively transported from the ontrastrial space to endolymph by the marginal cells.

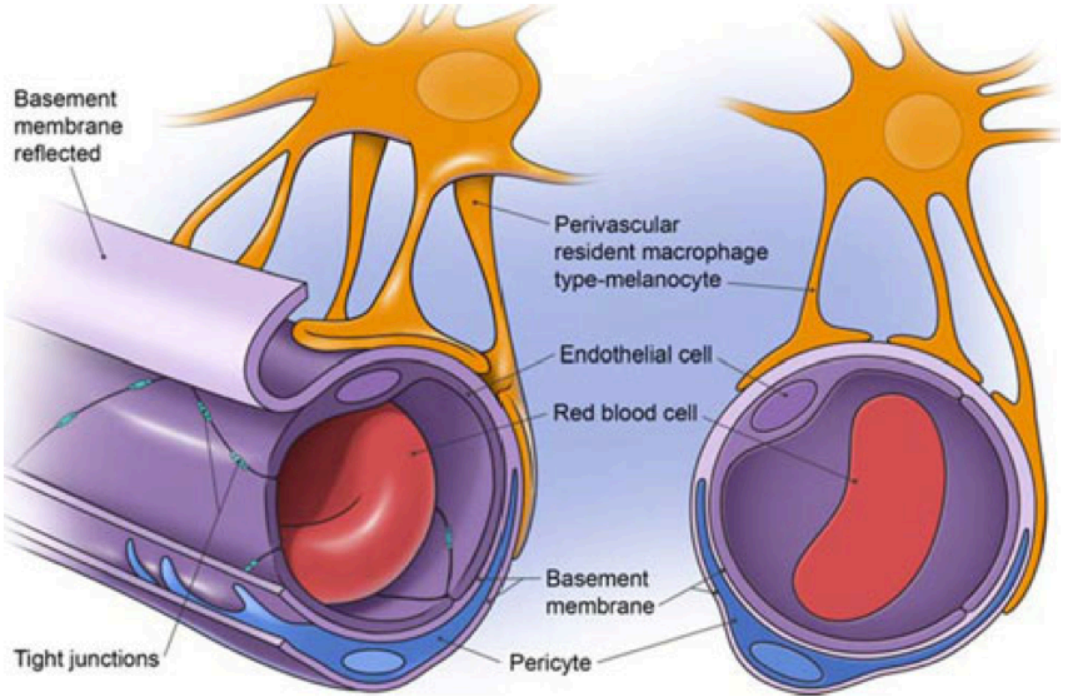

Figure 1-5 - Adapted from Neng, et al (2013) - structure of the blood-labyrinth barrier in the intrastrial space of the stria vascularis.

1.2.2 Responses to Injury

1.2.2.1 Oxidative-Stress and Inflammation

Oxidative-stress refers to cellular damage due to a reactive oxygen species (ROS) such as superoxides and hydroxyl free radicals, amongst others. ROS are produced throughout the body both as by-products of oxidative-phosphorylation in mitochondria (Böttger & Schacht, 2013) as well as by other intracellular enzymes such as cytochrome P450 (Bedard & Krause, 2007). ROS are also produced deliberately by the nicotinamide adenine dinucleotide phosphate (NADP) oxidase group of enzymes (Bedard & Krause, 2007) and perform a number of essential cellular functions. ROS are frequently utilised as intracellular signalling molecules (Mujica-Mota, Lehnert, Devic, Gasbarrino, & Daniel, 2014), and are important in innate immunity through the 'respiratory burst' response of neutrophils and monocytes to pathogens. Furthermore, a role for ROS in chemotaxis and facilitation of leukocyte migration has subsequently been identified (Cook-Mills, 2006).

The critical role of ROS in the pathogenesis of many forms of acquired hearing-loss is well recognised. ROS have been identified as key to losses related to cisplatin (Lautermann, Crann, McLaren, Schacht, & Kruszka, n.d.), aminoglycoside antibiotics (S. H. Hong et al., 2006), noise-trauma (Vlajkovic, Lin, Wong, Wackrow, & Thorne, 2013) and ischaemic (Morawski et al., 2003; Ohlemiller, Wright, & Dugan, 1999) events. Hearing-loss after exposure to ionising radiation involves multiple pathways of injury, with ROS and reactive nitrogen species (RNS) being key in many (Mujica-Mota et al., 2014).

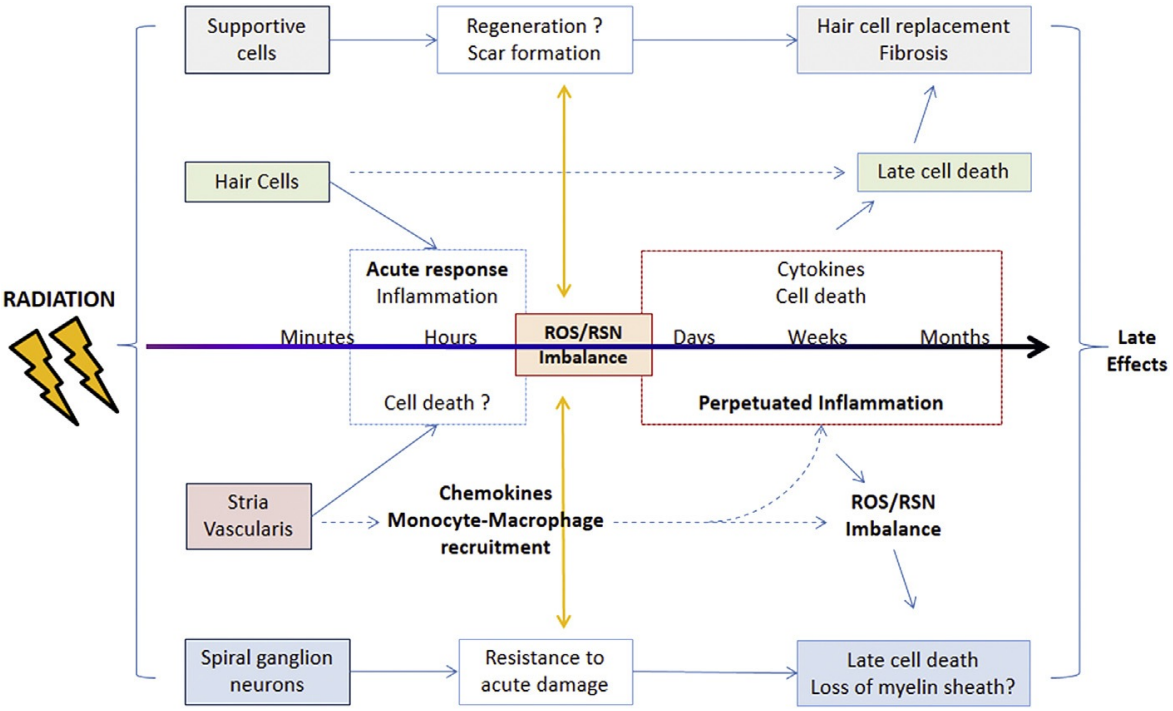

Figure 1-6 - Adapted from Mujica-Mota, et al (2014). Multiple pathways involved in sensorineural hearing loss after exposure to ionising radiation. Excess of ROS/RON is key to all mechanisms pictured.

NADP-oxidase enzyme NOX-3 is expressed in the cochlea more than in any other mammalian tissue studied thus far. It is localised to the organ of corti, vestibular sensory epithelia and spiral ganglia and is upregulated after administration of cisplatin, with subsequent superoxide-excess (Bánfi et al., 2004). Other NADP-oxidase enzymes, NUOX-1 and DUOX-2 have been found to be upregulated after noise trauma in rats, which adds further to superoxide-excess generated by outer hair cell (OHC) mitochondria. This excess can further reduce the oxygen supply to the overdriven OHC via production of 8-isoprostaglandin F2-alpha from lipid peroxidation (Ohinata, Miller, Altschuler, & Schacht, 2000), causing reduced cochlear blood flow ("The Role of Oxidative Stress in Noise-Induced Hearing Loss," 2018).

Excess of ROS has the potential to induce apoptosis of cells within the auditory apparatus. Attempts have been made at interrupting this chain with some success, with some groups targeting the ROS imbalance by attempting to reduce the metabolic demand of the cochlea in the injured state through hypothermia (Smith, Eshraghi, Whitley, Van De Water, & Balkany, 2009). Some have identified benefits with glutathione and n-acetyl-cysteine (NAC) treatment after injury to increase scavenging of ROS (Fetoni, Ralli, Sergi, & Parrilla, 2009; Ohinata, Yamasoba, Schacht, & Miller, n.d.).

Other groups have looked further down the cascade, aiming to block apoptotic signaling pathways in the face of ROS excess. The p38 mitogen-activated protein kinase (MAPK) and c-jun N-terminal kinase (JNK) apoptotic pathways (Tabuchi et al., 2011) have been targeted, either through direct inhibition, or via glucocorticoid receptor (GR) mediated inhibition (Canlon, Meltser, Johansson, & Tahera, 2007; Vivero et al., 2008).

1.2.2.2 Changes in Vascular Permeability and Strial Function

The stria vascularis is key to the generation and maintenance of the endocochlear potential (EP) and the cochlear endolymph. Derangements of function of the stria vascularis are implicated in many forms of sensorineural hearing loss, through failure of the endocochlear potential (F. Zhang et al., 2013a), changes in endolymph volume (Sakagami, Tomiyama, Fukazawa,

Umemoto, & Kubo, 1995), or the introduction of ototoxic compounds into the endolymphatic space (Li & Steyger, 2011).

As described earlier, the complex of strial capillary endothelial cells joined by tight-junctions, their basement membrane, pericytes and perivascular-resident macrophage-type melanocytes together make up the blood-labyrinth-barrier (BLB)(Figure 1-5). This barrier prevents passive movement of solutes and toxins into the endolymphatic space, facilitating active generation of the EP and endolymph (Juhn, Kim, Schachern, Tsuprun, & Adams, 2016; Neng, Zhang, Kachelmeier, & Shi, 2012; M. Suzuki, Yamasoba, Ishibashi, Miller, & Kaga, 2002).

Imaging of blood flow and vascular permeability in the stria vascularis has been achieved using various methods during the past 40 years. The stria vascularis has been well-characterised in cadavers (Kimura, Schuknecht, 1970, n.d.) and other animals (Reale et al., 1975; Takahashi, Kimura, & Ewertson, 1970) using Transmission Electron Microscopy (TEM) by many groups, with perimortem intravascular infusion of lanthanum nitrate utilised as a marker of increased vascular permeability (Figure 1-7) in the stria vascularis (X. Liu et al., 2013). Lanthanum nitrate is used as its electron-density makes it apparent on TEM. Lanthanum ions also move slowly across tight-junctions, with the rate at which it breaches cellular barriers providing a proxy measurement of 'tightness' or 'leakiness' of a barrier on TEM (Rask-Andersen, Bredberg, Lyttkens, & Lööf, 1981).

Histological methods of demonstrating increased strial vascular permeability have commonly involved the use of horseradish-peroxidase (HRP) or Evans Blue (EB).

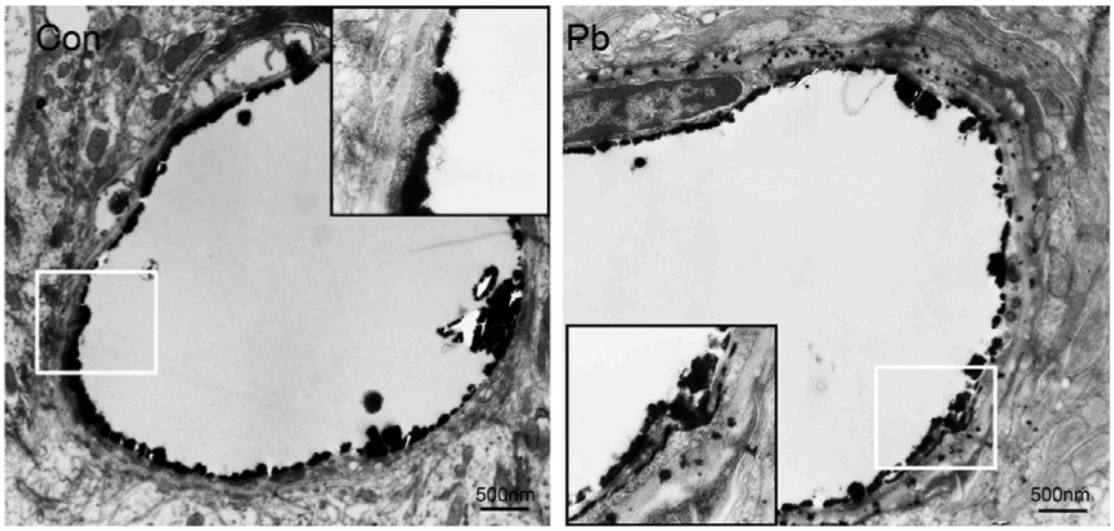

Figure 1-7 - From Liu, et al (2013) - TEM Images of strial capillaries demonstrating intravascular retention of lanthanum nitrate in control animals (Left - Con), with leakage of lanthanum after exposure to toxic levels of lead (Right - PB)

Horseradish peroxidase is a 44kD, ~5.5nm diameter enzyme used as a tracer through oxidation of a substrate. Substrates can be chromogenic to allow visualisation on light microscopy or quantification using spectrometry, where compounds utilised include chloronaphthol (4-CN), tetramethylbenzidine (TMB) and diaminobenzadine (DAB). DAB is also electron-dense, allowing visualisation using electron microscopy (Hukee & Duvall, 1985), while other substrates can be combined with conventional electron microscopy stains such as osmium tetroxide to generate a sufficiently electron-dense reaction product (Winther, 1971). Chemiluminescent substrates can also be used, to allow automated quantification of reaction product by photometric means.

Concerns have been raised about the suitability of HRP for capillary transport experiments because of the relatively-rapid transit of HRP across the endothelium when compared to other lipid-insoluble compounds of similar size (Santos-Sacchi & Marovitz, 1980) such as ferritin. Some suggest that HRP itself may alter capillary permeability due to its toxicity (Ross, Nuttall, & Wright, 1977; Santos-Sacchi & Marovitz, 1980).

Evans Blue is a 980 Dalton azo-dye compound that binds irreversibly to albumin at up to a 10:1 molar ratio (Rawson, 1943). It has been utilised for many years as a tracer for albumin, and thus plasma, loss from the intravascular compartment. It is often quantified through tissue digestion and then quantitative spectrophotometry, either directly or using fluorescence (Xu, Qaum, & Adamis, 2001). Evans Blue fluorescent properties also allow localisation of tracer on confocal scanning laser microscopy (Abraham, Deli, Joo, Megyeri, & Torpier, 1996), conventional fluorescence microscopy (Cheol Hee Choi et al., 2012; Jang et al., 2011; Schmutzhard et al., 2012; T. Suzuki et al., 2008), or through Light-Sheet Fluorescence techniques as discussed later.

MRI has also been used in recent years to assess the competence of the BLB, both through assessment of the rate of passage of gadolinium-based contrast agent (GBCA) from the intravascular to perilymphatic space (Floc'h et al., 2013) and the leakage of GBCA into the scala media, which is normally impermeable to GBCA (Zou, Pyykkö, Bretlau, Klason, & Bjelke, 2003).

1.2.2.3 Endolymphatic Hydrops

Endolymphatic hydrops (EH) is expansion of the endolymphatic space of the membranous labyrinth. EH has been accepted to be the fundamental pathological process involved in the clinical entity of Mèniére's Disease (Pierce & Antonelli, 2012); a debilitating condition characterised by episodic vertigo, progressive sensorineural hearing loss and tinnitus.

The mechanism through which EH causes episodic vertigo is debated to this day, with theories of microscopic ruptures of the distended endolymphatic system being popular. These ruptures would cause local mixing of the ionically distinct endolymph and perilymph, depolarising the neuroepithelium of vestibular end organs.

The mechanism by which EH causes acute deterioration of hearing thresholds during episodes is thought to be displacement ('biasing') of the basilar membrane towards the scala tympani, causing deflection of the hair-bundle away from the kinocilium with resulting hyperpolarisation of the inner hair cell. Displacement of the basilar membrane into the scala tympani has been observed in endolymphatic hydrops, particularly in the apical portions of the cochlea which tonotopically represent the lower frequencies of hearing most affected by Mèniére's (Xenellis, Linthicum, Webster, & Lopez, 2004).

More recent work has seen the identification of EH in other clinical pictures such as sudden sensorineural hearing loss (SSNHL) (Shimono et al., 2013), perilymphatic fistula (Nomura, Hara, Funai, & Okuno, 1987), congenital syphilis

(Belal & Antunez, 1980), and acute noise-exposure (Salt, 2004). Cochlear endolymphatic hydrops has also been noted on histopathological examination of human temporal bones after cochlear implantation (Tien & Linthicum, 2016).

Moreover, it has been established that endolymphatic hydrops need not affect all portions of the membranous labyrinth (Egami et al., 2013), nor even cochlea, equally (Bachor & Karmody, 1995).

From first principles, expansion of the endolymphatic space will occur after overproduction of endolymph, reduced removal of endolymph, or a combination thereof. Numerous animal models of endolymphatic hydrops exist, often employing a method of stimulating endolymph production through immunogenic (Pyykkö, Zou, Poe, Nakashima, & Naganawa, 2010; Sakagami et al., 1995), scala media injection (Brown, Chihara, & Wang, 2013) or hormonal methods. A combination of these methods, such as Lipopolysaccharide and Aldosterone (Takumida, Akagi, & Anniko, 2009) is also proposed by some groups. Ablation of the endolymphatic sac or interruption of its duct (Konishi, 1977; Sakagami et al., 1995; Warmerdam, Schröder, Wit, & Albers, 2003) is occasionally performed to reduce endolymph absorption at this site, while a combination of techniques may be utilised to perturb both sides of the endolymph volume equation (Dunnebier, Segenhout, Wit, & Albers, 1997). Models of isolated cochlear endolymphatic hydrops are fewer, due to the difficulty involved in surgical access (Kimura, Schuknecht, Ota, & Jones, 1980) to the site of likely cochlear endolymphatic outflow through the ductus reuniens (DR).

Endolymphatic hydrops has traditionally been identified using electrophysiological measures or conventional histopathology, though recent years have seen the demonstration of more contemporary imaging techniques.

Electrophysiological identification of EH is performed using electrocochleography, where near-field recordings are made of the electrical responses of the organ of Corti and auditory nerve in response to auditory stimuli. Two portions of the electrocochleograph are typically utilised to support a diagnosis of EH.

The summating potential (SP) is the calculated sum of the cochlear microphonic responses to stimuli of alternating polarity. This direct current charge can reflect the resting position of the basilar membrane and organ of corti, and thus the resting state of tip-link actuated ion channels. An enhanced SP is thus thought by many to be the result of Basilar Membrane biasing due to EH (Gibson, 2009) (Figure 1-8). The compound action potential (CAP) follows the SP and is the sum of the alternating current response of cochlear nerve fibres to the stimulus.

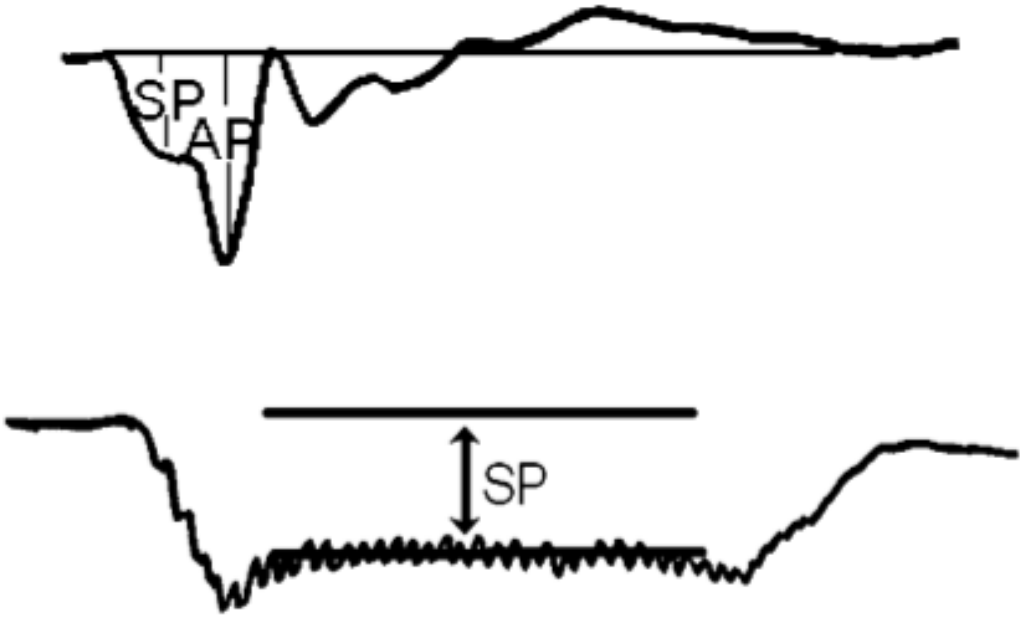

Figure 1-8 - From Gibson, et al (2009). Top image demonstrates a summed electrocochleography recording in response to a pair of alternating-phase clicks, with SP and CAP (AP) marked. The bottom image demonstrates the SP in response to a tone-burst.

In acute endolymphatic hydrops, the SP should increase with the degree of displacement of the basilar membrane, while the CAP may be unchanged. Measurement of the ratio of SP/CAP for a click stimulus is thus frequently used to aid diagnosis of EH (Conlon, 2000). The absolute voltage of the SP in response to a tone can also be used (Gibson, 2009).

The assessment of the presence or absence of EH on a histopathological slide is generally a qualitative measure. Fixed, embedded tissue is sliced and mounted, with note made of the position of Reissner's membrane and perhaps the position of the basilar membrane (Figure 1-9). Slices can be obtained through the vestibule, demonstrating distension of the membranous saccule and utricle and approximation of the membranous saccule to the stapes footplate.

Unfortunately, this technique will only allow assessment of EH in a single plane for each organ and is also susceptible to artefactual changes in membrane length (see *Fixation and Processing Artefacts*).

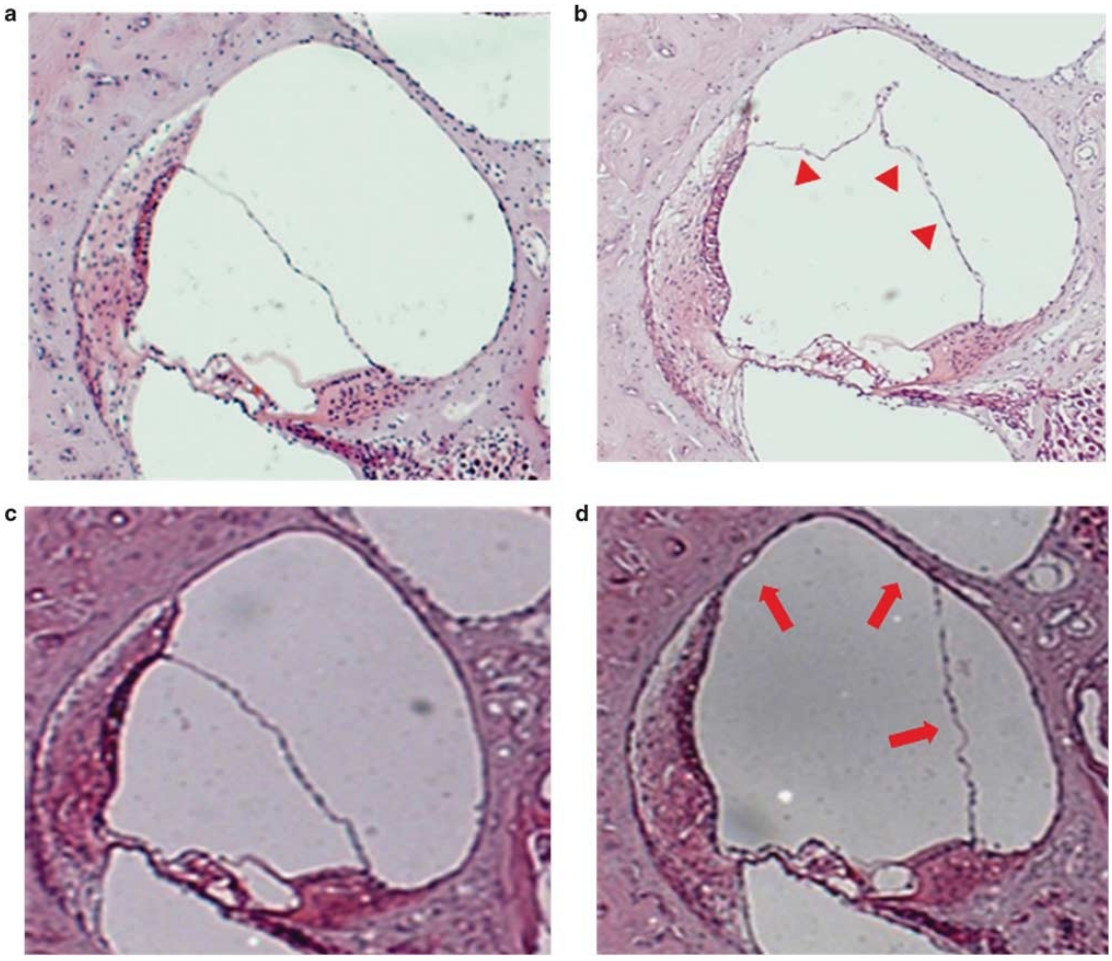

Figure 1-9 - From Egami, et al (2013) - Histological assessment of endolymphatic hydrops: (a) Control, (b) Surgical ablation of the endolymphatic sac, (c) infusion of Desmopressin, (d) Combined effect of surgical ablation and desmopressin infusion.

Magnetic Resonance Imaging (MRI) has been used both experimentally (Zou, Poe, Bjelke, & Pyykkö, 2009) and clinically (Fukuoka et al., 2010; Iida et al., 2013; Nakashima et al., 2009; Pyykkö, Nakashima, Yoshida, Zou, & Naganawa, 2013; Seo, Kim, Choi, & Lee, 2013) in the semi-quantitative assessment of EH. Visualisation of EH using MRI relies on the differential permeability of the endolymphatic and perilymphatic compartments of the labyrinth to gadolinium-

based contrast agents (GBCA). GBCA can be administered intravenously, as is their typical use, but perilymphatic uptake of GBCA is higher after transtympanic injection of GBCA (Iida et al., 2013; Naganawa et al., 2014).

More recently, Optical Coherence Tomography (discussed in detail in *Interferometry - Optical Coherence Tomography*) has been utilised to visualise the position of Reissner's membrane in murine and guinea-pig models of EH (Kakigi et al., 2013).

1.2.2.4 Disruption of cochlear mechanics

A consensus has not been found on the effect of the simple presence of a cochlear implant electrode on cochlear mechanics. Huber's group (Huber, Hoon, Sharouz, Daniel, & Albrecht, 2010) found no significant effect of electrode insertion on intraoperative measurements of stapes and round window motion on auditory stimuli. Like the Huber group, Donnelly (Donnelly et al., 2009), used LASER vibrometry to assess stapes movements before and after electrode insertion and noted an effect on mechanics at lower frequencies.

The influence of the quantity and location of cochlear implant tissue response on cochlear mechanics and residual hearing after cochlear implantation has not been thoroughly investigated. Choi (Chul-Hee Choi & Oghalai, 2005) modelled the effects of fibrosis in the scala tympani and fixing the basilar membrane on cochlear mechanics and suggested that fibrosis altering fluid dynamics of the scala tympani would affect cochlear mechanics at low frequencies, whilst fixation of the basilar membrane would see effects closer to the base of the cochlea. This

modelling fits with the ideas of O'Leary (S. J. O'Leary, Monksfield, Kel, Connolly, Souter, Chang, Marovic, O'Leary, Richardson, & Eastwood, 2013b) and data collected by Burghard (Burghard et al., 2014), who found that increasing volumes of tissue-response to a cochlear implant electrode in the scala tympani correlated with degradation of hearing-thresholds apical to the extent of the tissue response. Kiefer (Kiefer, Böhnke, Adunka, & Arnold, 2006) also modelled basilar membrane fixation due to electrode impingement and found no effect on apical regions of the basilar membrane far removed from the position of the electrode.

The round window membrane (RWM) is another site involved in therapeutic interventions that can have its function altered. Experimental fixation of the round window causes a significant cochlear conductive hearing loss in guinea-pigs (Nageris et al., 2012), with similar losses seen in human patients with congenital or acquired immobility or obliteration of the RWM (T. E. Linder et al., 2003). These findings may be relevant both to the round-window-insertion technique of cochlear implantation and the utilisation of the RWM as a drug-delivery site.

Most assessments of tissue-response to a cochlear implant electrode are limited to a small number of sections (Farhadi et al., 2013), or only mid-modiolar sections (S. J. O'Leary, Monksfield, Kel, Connolly, Souter, Chang, Marovic, O'Leary, Richardson, & Eastwood, 2013b). The Burghard group (Burghard et al., 2014) performed assessments at a greater number of sites using a grinding-polishing technique, but this technique will still generate, in essence, discontinuous data.

1.3 Imaging Techniques

The inner ear of mammals is a complex, three-dimensional structure where position and orientation of structures have strong implications for their function. Three-dimensional imaging of the cochlea is thus desirable when examining otopathology.

Although a three-dimensional dataset is often visualised using planar slices, the ability to generate a slice in any desired plane is of considerable benefit. This can be seen when aligning a slice to the plane of a semicircular canal to identify a dehiscence (Belden, Weg, Minor, & Zinreich, 2003; Rosowski, Songer, Nakajima, Brinsko, & Merchant, 2004; Vanspauwen et al., 2006) or aligning a slice to a particular point on the frequency-place-map of the mammalian cochlea. Three-dimensional datasets will even allow the examination of curved structures using arbitrary planes, such as a plane placed along the length of the ductus reuniens of the inner ear (Figure 1-10).

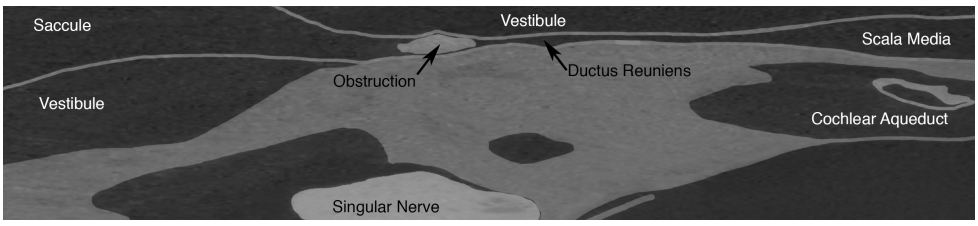

Figure 1-10 - Arbitrary curved plane generated along the length of the ductus reuniens of the guinea-pig cochlea demonstrating ductus obstruction. Overdrawn Micro-CT data.

Three-dimensional data also becomes important when considering the volume of structures, or when the integrity of structures is to be examined.

When constructing a three-dimensional dataset, there are two basic methods of constructing a volume. A volume can be reconstructed from a stack of planar slices, or a volume can be tomographically reconstructed from a series of projections of the area of interest. Some techniques, such as non-helical linear-detector computed tomography use of a combination of both principles to generate an image volume.

1.3.1 Conventional Histological Techniques

Histology (Greek words: ἱστός histos "tissue", and -λογία -logia "science") refers to the techniques of fixing, sectioning and staining of tissues for examination; generally using a light microscope. Histological examination, in the presence of well-prepared material and good equipment, provides levels of cellular detail surpassed only by electron microscopic techniques. The technique is widespread and highly adaptable. With the advent of immunohistochemistry and immunofluorescence techniques, subcellular components can be visualised. The costs involved in judicious (see *Discontinuous Data)* histopathological examination are also relatively low. Histopathological examination remains the gold-standard for examination of most otopathology, but there are some pitfalls; particularly when examining some of the responses to injury relevant to this thesis.

1.3.1.1 Discontinuous Data

The vast majority of tissue processed for histological examination is discarded. Slices of the specimen of varying thickness are obtained at slicing intervals such that less than two per-cent of the tissue volume may actually be examined[1]. Pathological processes occurring between slices must thus be inferred from the appearance of the slices taken before and after that interval. There is no absolute requirement for any tissue to be discarded during histological

[1] Taking an institutional example where resin-embedded cochleae are processed with a slice thickness of 2μm, with an interval between used slices of 125μm.

processing, but the time and cost involved in processing all tissue is a significant disincentive.

1.3.1.2 Processing Time

Many imaging techniques have significant advantages in terms of processing time when compared to conventional histological techniques.

Once cochlear tissue is obtained for conventional histology, a number of processes are performed in sequence:

Fixation

Decalcification

Orientation

Embedding

Cutting and mounting

Staining

Scanning

These processes in sequence see an interval of at least one month between harvesting of tissue and the collection of any usable data. Different imaging modalities will allow elimination of one or more of these processes. Micro-CT imaging, for example, requires only fixation prior to scanning, meaning that data

on bony structures can be obtained within two days of harvesting tissue. This is an extreme example, however, with most imaging modalities requiring some additional processing for optimal image acquisition.

1.3.1.3 Fixation and Processing Artefacts

Detailed examination of the structures of the inner ear, whether using conventional histology or contemporary imaging techniques relies upon rapid and thorough processes of fixation of the bony and membranous structures therein.

Acceptable intervals between death and fixation of the inner ear for microscopic examination have decreased as the power of microscopic techniques has increased. Changes in hair-cell morphology visible on scanning electron microscopy (SEM) have been noted in humans within between 15 (Osborne, Comis, Johnson, & Jeffries, 1989) and 40 minutes (A. Wright, 1980) after cessation of circulation with a negative-correlation between time to fixation and quality of fixation for both electron microscopy (Nadol & Burgess, 1985) and light microscopy (Rutledge, 1969).

Varied techniques of fixation have been used in the preservation of human and animal temporal bones. Any technique of fixation should address three goals, those being the arrest of autolysis by the body's own enzymes released at death, prevention of extrinsic degradation by microorganisms and alteration of the physical characteristics of the tissues to improve their resilience during destructive preparation.

Cross-linking, aldehyde fixative solutions are used frequently. They act by cross-linking lysine residues of adjacent proteins and anchoring them to cytoskeletal elements, thus making the tissues resistant to proteolytic enzymes and stiffening their overall structure. The most frequently used compounds are formaldehyde and glutaraldehyde. Formaldehyde has an advantage in that its lower molecular weight leads to more rapid diffusion through tissues, while glutaraldehyde's length and additional active site produces a more resilient product. Mixtures of the two compounds are used in some fixatives to good effect, examples of this being Karnovsky's Fixative (Karnovsky, 1965) or the more concentrated Britta's Fixative (Engstrom, Hillerdal, & Hillerdal, 1990).

Precipitating, or 'denaturant' fixatives, such as ethanol, methanol, acetone or acetic acid, act by reducing the solubility of proteins in tissue as well as altering their tertiary structure, causing precipitation and aggregation.

Oxidising agents, such as osmium tetroxide can also be used as tissue fixatives (Nielson & Griffith, 2017). Similar to the cross-linking action of aldehyde fixatives, osmium tetroxide can oxidise side chains of structural proteins at multiple sites, cross-linking the proteins. Osmium tetroxide-fixed tissue is relatively impenetrable to further osmium tetroxide, meaning that it is not useful for fixation of thicker specimens. Osmium tetroxide also tends to precipitate proteins when used as a primary fixative, limiting the suitability of the fixed-tissue for immunohistochemical processes.

Tissue-shrinkage and hardening is a problem with most denaturing and cross-linking fixatives. This becomes particularly problematic when shrinkage rates vary tissue-to-tissue in the same specimen, causing anatomical distortion. This

fact is further discussed by Brunschwig and Salt (Brunschwig & Salt, 1997), who discuss the impact of changes in length of Reissner's Membrane produced by the use of different tissue-fixatives (Figure 1-11) in the histological assessment of endolymphatic hydrops.

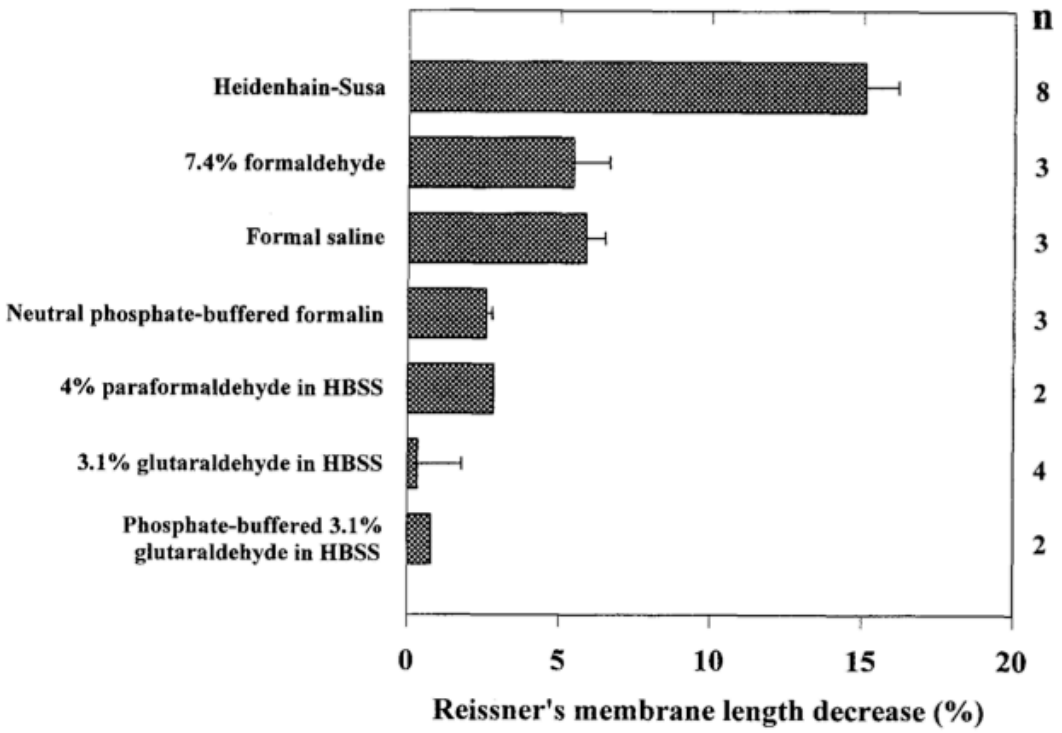

Figure 1-11 - Lengthwise shrinkage of Reissner's membrane during fixation with various fixatives - from Brunschwig and Salt (1997)

Because of the rapid degeneration of the membranous structures of the inner ear post-mortem, expedient treatment with fixative is required to preserve these structures for microscopic examination. In experimental animals, this is often achieved through intravascular perfusion with fixative solution (Uzun, Curthoys, & Jones, 2009). This is occasionally supplemented by perilymphatic perfusion of fixative solution through the round and oval windows (Anniko & Lundquist, 1977; Osborne et al., 1989; Osborne & Comis, 1990; Spicer & Schulte, 1996) and

sometimes opening of the helicotrema (Bohne & Harding, 1997). Violating the perilymphatic space before tissue is properly fixed means that assessment of volumes of the perilymphatic spaces and the positions of their enclosing membranes cannot be reliably performed. Perfusion of the perilymphatic space prior to and during fixation could also alter the position of intrascalar tissues such as the tissue-response to a cochlear implant electrode.

After fixation, long-term preservation of the tissue is the major issue. Tissues may be kept in the fixative for a reasonable period of time, but the toxic nature of many fixatives means that working with these tissues is dangerous to the health of the handlers. Long immersion in fixatives also leads to degradation in surface proteins utilised as binding sites in Immunohistochemistry. Tissues can be dehydrated in graded alcohols, but this can result in further shrinkage and deformation of fine soft-tissues (Lim, 1980), making measurements of fluid compartments less reliable.

Slicing and mounting of tissue on slides introduces the possibility of significant distortion of the sliced tissue. This is more significant in the process of frozen-sectioning, where tissue is embedded in a mixture of polyethylene glycol (PEG) and polyvinyl alcohol (PVA) that is a viscous, but pourable liquid at room temperature. At -20 Centigrade, the material is solid and of similar consistency to soft tissue at that temperature. Cutting is performed on a microtome chilled to -20 Centigrade. Although frozen-sectioning generally involves thicker slicing than resin or wax embedded tissue, the embedding material softens quickly and becomes very pliable, meaning that slices can easily roll, fold, tear or become otherwise distorted when being transferred from block to slide.

1.3.2 Contemporary Techniques

1.3.2.1 Light-Sheet Fluorescence Microscopy

Light-sheet fluorescence microscopy (LSFM) is an umbrella term encompassing a number of techniques (Santi et al., 2018) such as orthogonal-plane fluorescence optical sectioning (OPFOS), thin-sheet LASER imaging microscopy (TSLIM) and selective-plane illumination microscopy (SPIM).

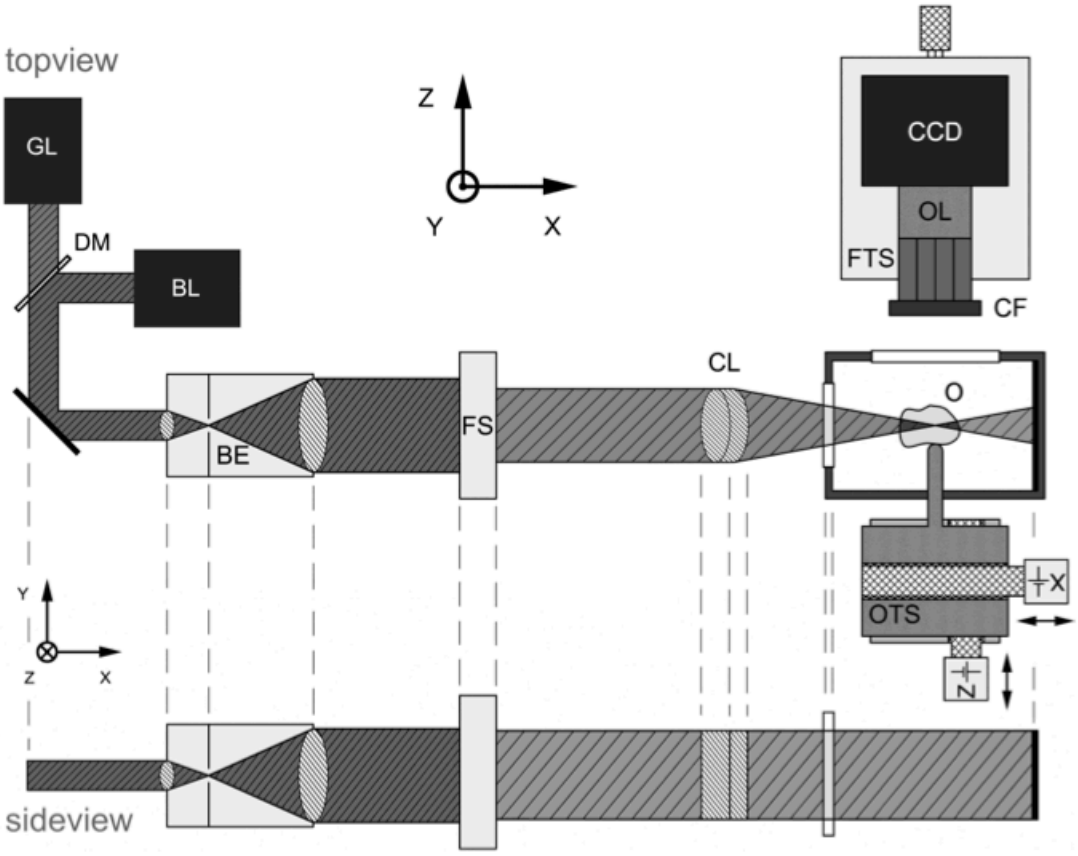

Figure 1-12 - From Buytaert, et al (2011) - Schematic of a Thin-Sheet LASER Microscope from top and side view. A LASER of desired wavelength (GL/BL: green light/blue light) forms a beam reflected through a beam-expander (BE), field-stop (FS) and cylindrical lens (CL) to form a LASER sheet. The imaged object (O) is mounted upon a an object transport system (OTS) to allow positioning within the confocal portion of the light sheet. Imaging is performed by a CMOS or CCD camera (CCD) via a microscope objective lens (OL) and colour filter (CF) if required.

What is common to the techniques is the use of a light-source with associated optics to form the light path into a sheet, focussed in the centre of the region of interest. When Siedentopf and Zsigmondy first described the concept in the early 20th century, visible light was collected, collimated and used to illuminate particles in a colloid in a plane orthogonal to the visual axis of their microscope. They referred to the apparatus as an Ultramicroscope (Becker, Jährling, Saghafi, & Dodt, 2013).

The sheet of light allows virtual sectioning of a specimen, which can then be moved along the z-axis within the light path to position the optical section at the desired depth within the specimen (Figure 1-12). Images are acquired in the z-axis, orthogonal to the plane of the light-sheet using a charge-coupled device (CCD) or complementary metal-oxide-semiconductor (CMOS) sensor. This process can be automated by the way of stepper-motors to allow automated acquisition of images through the depth of a specimen for formation of a 3D volume from stacked slices (Buytaert, Johnson, Dierick, Salih, & Santi, 2013; Santi, 2011).

The specimen must be translucent, to minimise the effect of light fall-off in parts of the specimen further from the light source. The light-path is often split and then the specimen illuminated from opposite sides to minimise this effect. LSFM techniques were originally used to image specimens that were already translucent, such as early embryos, but the technique was expanded to tissues that had been made translucent during processing. Specimens are fixed using formaldehyde or glutaraldehyde, decalcified if necessary, then incubated in Spalteholz fluid (Steinke & Wolff, 2001). Spalteholz fluid, consisting of benzyl

benzoate and methyl salicylate, clears tissue pigments and reduces the refractive index of the tissue (Santi et al., 2018).

Many components of fixed-tissue will autofluoresce when excited by a suitable LASER. Additional stains, including immunostains, can also be visualised using LASER excitation during LSFM (Becker et al., 2013; Kopecky, Santi, Johnson, Schmitz, & Fritzsch, 2011).

Recent refinements in the area focus on modification of the light-source to avoid the issues created by a static light source. The ideal illumination for LSFM would be a uniform, collimated sheet of LASER light, but compromises between collimation and intensity mean that the sheet used still narrows to a waist at a given distance, and it is around this point (the confocal parameter, where the width of the beam remains relatively constant (Schröter, Johnson, John, & Santi, 2012)) that the thinnest, most-focussed portion of the optical section occurs. With a static light sheet, then, the z-resolution of the resulting image is limited by the width of the light sheet in the region of interest and image quality reduces towards the peripheries of the optical slice.

Scanning techniques have seen movements of the specimen along the x-axis, with stitching of the focussed segments of the images into a complete slice. A scanning line camera can be used to avoid a full acquisition for each segment of the stitched-slice, but that involves synchronising movement of the specimen with the scanning rate of the line camera (P. Schacht, Johnson, & Santi, 2010). An alternative scanning technique involves scanning a narrow LASER beam using piezo-electrically actuated mirrors to create a sheet, rather than a cylindrical

lens (Mertz & Kim, 2010), thus avoiding the unfavourable optics of a static light-sheet.

Scatter from refractive elements within the specimen increase the effective width of the beam as it transits, as well as illuminating structures at depths outside the desired optical section. Several groups have utilised structured light-sheets of various conformations in order to suppress out-of-focus background elements illuminated by scattered light. This relies on the fact that if the light sheet is structured in the form of a horizontal grid, only elements within the optical slice will be modulated in the pattern of the horizontal grid. This modulated image can be used to reduce out-of-focus elements (Figure 1-13) in an image acquired using a uniform light sheet (Mertz & Kim, 2010).

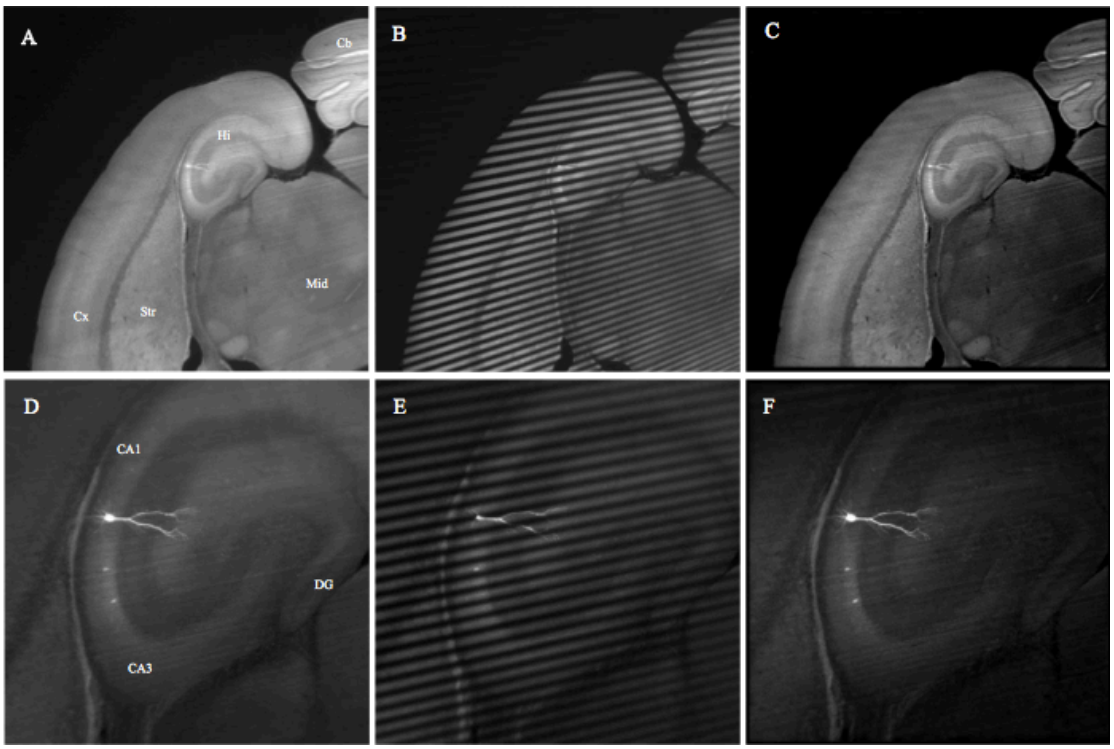

Figure 1-13 - From Mertz, et al (2010) - Illustration of the use of structured illumination to reduce out-of-focus elements during imaging of a whole mouse brain. Mid: midbrain, Hi: hippocampus, Str: striatum, DG: dentate gyrus, Cx: cortex, Cb: cerebellum, CA: cornu ammonis . (a) and (d) - uniform sheet, (b) and (e) - grid modulation, (c) and (f) combined images.

1.3.2.1.1 In Otology

LSFM techniques have only been refined in recent years, but a lot of this refinement has been performed whilst imaging otologic specimens. The technique was applied to the guinea-pig cochlea in 1995 by Voie, et al, with the same group later refining their technique to allow imaging of an intact guinea-pig tympanic bulla in 2001 (Voie, 2001). Santi (Santi et al., 2018) used visualisation of mouse spiral ganglion neurons, hair cells and Reissner's Membrane (Figure 1-14) as a demonstration of the resolving ability of their static sheet system constructed from off-the-shelf components.

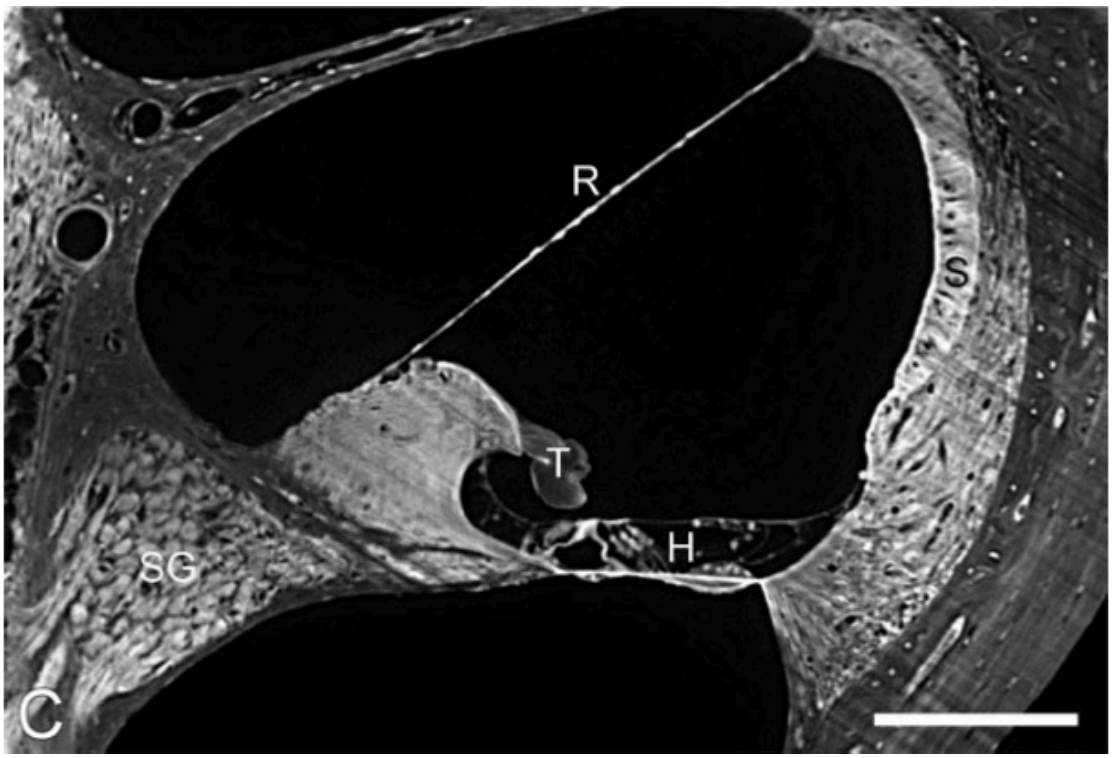

Figure 1-14 - Adapted from Santi, et al (2011) - TSLIM image of the mouse scala media, with Reissner's Membrane (R), Tectorial Membrane (T) and three Outer Hair Cells (H) readily visible. Spiral Ganglion neurons (SG) are at bottom left. Scale bar: 100µm.

Buytaert, et al (2013) made a detailed comparison of the relative merits of their in-house LSFM and micro-CT systems. They concluded that each method has its place, with micro-CT perhaps necessary for calibration of measurements performed using TSLIM. TSLIM specimen preparation involves fixation, decalcification, dehydration and clearing: all steps that introduce shrinkage. Micro-CT specimen preparation involves fixation only, with the shrinkage involved therein limited by the intact bone. They calculated that the extra processing involved saw TSLIM specimens shrunk an extra ~4.2% in each dimension when compared with paraformaldehyde-fixed Micro-CT specimens

(Buytaert et al., 2013). TSLIM's remarkable visualisation of soft-tissues is a distinct advantage if that is required.

1.3.3 Tomographic Techniques

Tomography (derived from Ancient Greek τόμος *tomos*, "slice, section" and γράφω *graphō*, "to write") was initially used with conventional x-ray projections to provide selective focus; a technique developed by Allesandro Vallebona in 1930. An x-ray source and detector/film were rotated around the point of interest during the projection, blurring parts of the image away from the centre of rotation and reducing the effect of superposed objects that would interfere with examination from a single viewpoint.

Tomography today generally refers to computed tomography, where x-ray projection images taken at a variety of angles around an attenuating sample permit reconstruction of cross-sectional images.

Micro-CT relies on the principles of x-ray computed tomography (CT), which has been used for decades in clinical imaging and research. Using a micro-focus x-ray source, x-ray attenuation images are produced on a scintillator and captured by a camera. A number of these projections are acquired, whilst rotating the subject with respect to the x-ray path. The resulting series of projections are reconstructed using tomographic reconstruction algorithms to generate a three-dimensional volume. Where high-resolution clinical CT typically generates volumes with spatial resolution down to 0.25mm, Micro-CT is capable of acquiring datasets with spatial resolution of 1μm and beyond (NanoCT).

As can be expected from first-principles and experience with conventional computed tomography, imaging of the inner ear after cochlear implantation presents additional challenges.

The use of metals such as Platinum (Pt) and Iridium (Ir) in the manufacturing of research and clinical implant electrodes presents a problem when attempting to acquire a high quality, three-dimensional dataset. Reliable identification of scalar positioning of a cochlear implant electrode requires imaging of the cochlear partition to determine the limits of scala tympani. The cochlear partition, even in its bony portion, attenuates few x-ray photons when compared to Pt/Ir wires and electrode contacts. This large difference in attenuation, combined with the relatively poor dynamic range of charge-coupled device (CCD) cameras makes simultaneous imaging of the detail of both an electrode and intracochlear anatomy difficult (Wimmer et al., 2014).

Making measurement of intrascalar positioning of an electrode ever more difficult are the various artefact phenomena associated with imaging of metallic structures and subsequent tomographic reconstruction. Beam-hardening due to differential attenuation of x-ray photons from a polychromatic x-ray source is a particular issue when two or more high-attenuation regions are present in the same scanning plane; as is the case when imaging a cochlear implant in any possible plane. This artefact can be intensified by the filtered back-projection (FBP) techniques commonly used for tomographic reconstruction of 3D datasets. Noise, both Poisson and due to Compton Scattering of photons to starved areas of the detector is also not improved by the use of FBP

Several strategies exist to improve the reliability of electrode-scalar localisation techniques. The simplest is the use of dummy electrodes that do not contain metallic components. Opinion on the place of silastic 'dummy' electrodes in the simulation of the behaviour of clinical electrodes varies, but Roland (Roland, 2005) has demonstrated that a large component of the biomechanical behaviour of the intracochlear portion of an electrode is determined by the silastic carrier, rather than the metallic components of the clinical electrode. This allows us to utilise silastic dummy electrodes for insertional trauma research with more confidence. This strategy falls down in situations where wires and contacts are required, such as long-term stimulation studies, or measurement of intracochlear potentials.

Another strategy is to avoid FBP as a tomographic reconstruction method. Iterative reconstruction (IR) methods were used early in the development of computed tomography, but rapid increases in the volumes of data acquired meant that computational requirements for IR outstripped available hardware. Only recently has IR once again become feasible for clinical imaging (Beister, Kolditz, & Kalender, 2012). IR techniques do not involve the amplification of metal-edge artefact inherent to FBP and integration of metal artefact reduction (MAR) algorithms appears to be more successful with IR than FBP reconstruction (Morsbach, Bickelhaupt, et al., 2013a; Morsbach, Wurnig, et al., 2013b). Iterative reconstruction techniques to facilitate MAR are not infallible (Cheng, Romero, & Duddalwar, 2014), however, and their limitations will only become more apparent as their utilisation becomes more widespread. Of particular relevance to our situation is clearing and blurring of tissues (Boas &

Fleischmann, 2012) immediately surrounding the area of MAR, which may have implications for visualisation of the osseus spiral lamina when electrode hardware is adjacent.

Another methodology that seeks to address both the issues of dynamic range and metal artefact is coregistration. One dataset is acquired with the implant electrode in-situ, utilising high-energy photons to reduce scatter and beam hardening secondary to metallic structures. A second dataset is acquired using lower-energy photons to better delineate soft tissues. This can be performed prior to insertion of the electrode (Postnov et al., 2006), or after the electrode has been removed and this order will depend on the context of imaging.

The use of digital subtraction of Micro-CT images before and after implantation has been demonstrated to allow reduction of electrode-related image degradation, but introduces other potential confounding factors. As demonstrated by Roland (2005), the force of insertion of a cochlear implant electrode generates a 'Resultant Rising' force that directs the electrode array towards the Basilar Membrane. The Resultant Rising force, largest in the ascending limb of the basal turn, is thought to be responsible for the large proportion of electrode-trauma seen in this region of the cochlea. Digital subtraction Micro-CT may not take into account distortion of the soft-tissue architecture of the membranous labyrinth generated by the Resultant Rising force of electrode-insertion, giving a less-reliable assessment of electrode-location.

1.3.4 Interferometric Techniques

Interferometry relies on the principles of interference of waves originating from the same source, which have travelled different paths to a common end-point. Depending on the length of the path or changes in refractive index of materials along the path, waves will arrive in or out of phase. Waves arriving at the end-point in phase will interfere constructively, where waves arriving out of phase will interfere destructively.

The most widespread uses of interferometry in medicine are Optical Coherence Tomography and Phase-Contrast Radiography.

1.3.4.1 Interferometry - Optical Coherence Tomography

Optical Coherence Tomography (OCT) is used commonly in Ophthalmology as a means of real-time, depthwise imaging of the retina.

OCT, first described by Huang (D. Huang et al., 1991), relies on the properties of the Interferometer, the prototype being described by Michelson (Figure 1-15).

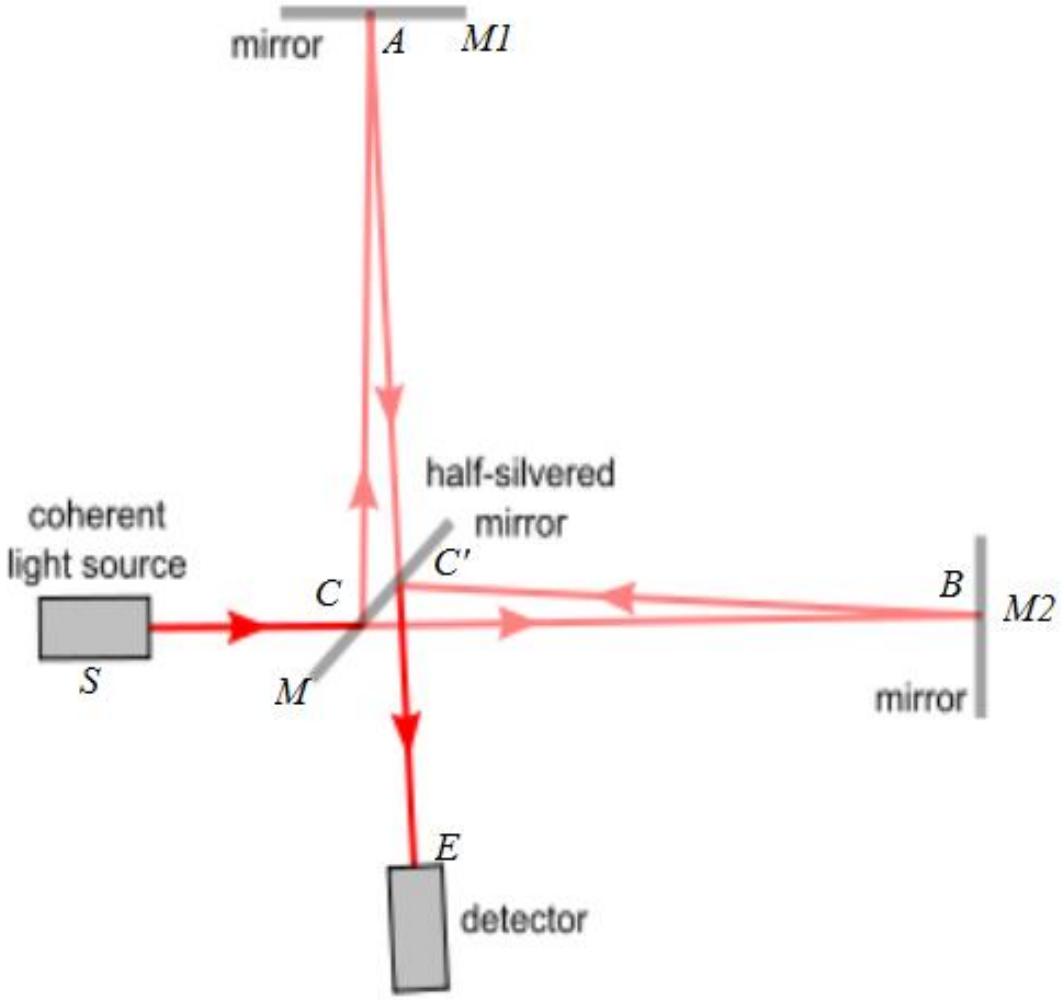

Figure 1-15 - Light path in a Michelson Interferometer. Sourced from WikiCommons - Jbeam.scholar

The half-silvered mirror (*M*) in the interferometer both splits the beam and recombines the beams after the two components have completed their separate paths. Interference patterns produced by in- or out-of-phase waves are detected at (*E*). Replace *M1* with a piece of semi-reflective tissue and interference patterns will be produced when light is reflected back to *M* and thus *E* by structures within the tissue. Constructive interference will occur when light is reflected by a tissue interface at a depth such that the path length is identical to the *M-M2*

path. Larger amounts of constructive interference arise from areas of higher reflectivity.

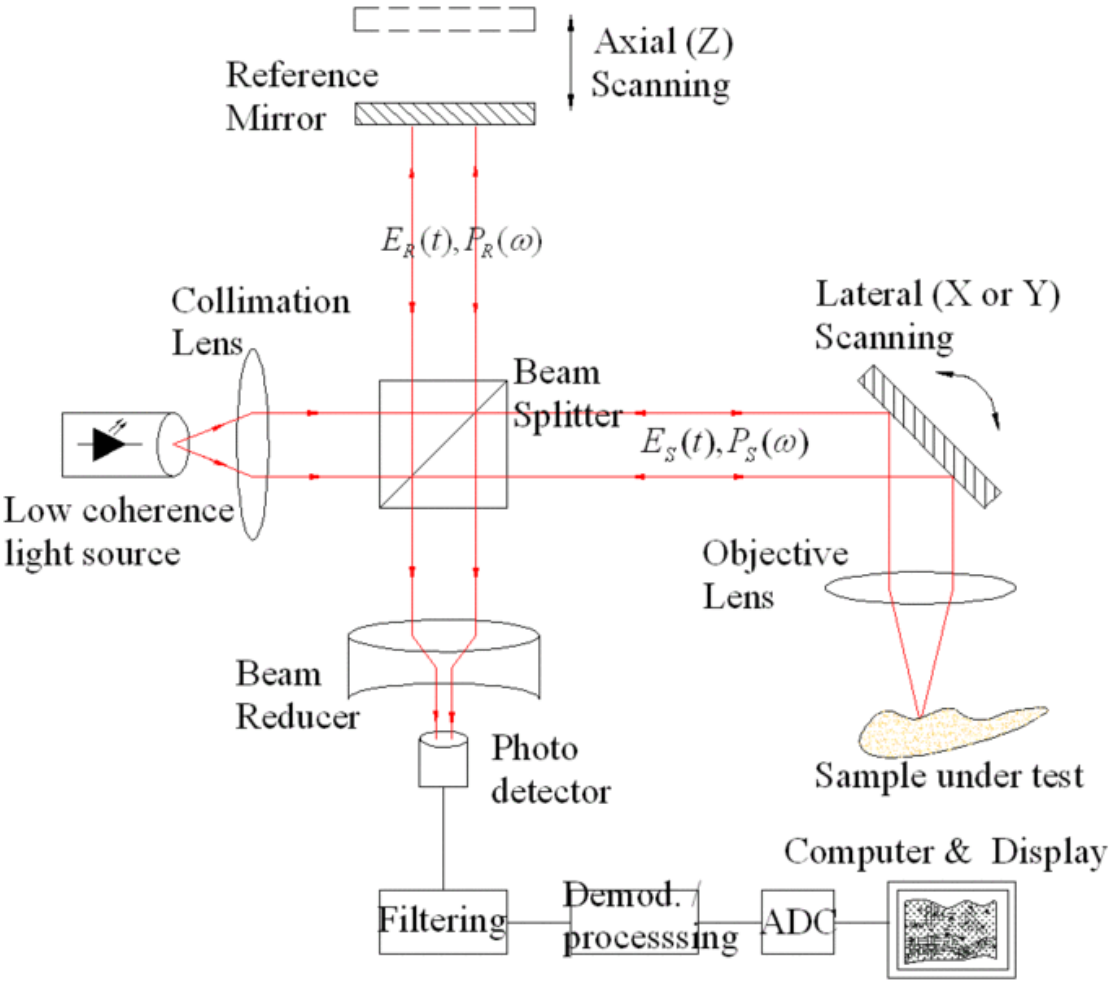

Figure 1-16 - Time-Domain Optical Coherence Tomography. Point detection is combined with Z scanning by altering the position of the reference mirror and XY scanning by changing the direction of the Sample beam towards the sample. Sourced from WikiCommons – pumpkinegan.

Original applications of OCT saw reflectivity measured at a single point, with the position of this point altered in the Z-axis (depth) by altering the distance between the beam splitter and Reference mirror. Movement of the point of

measurement in a second dimension was produced by rotation of a mirror placed in the beam splitter – sample light path (Figure 1-16). This configuration is known as Time-Domain OCT (TD-OCT).

Subsequent modifications aimed to improve both scanning time and spatial resolution.

Spectral-Domain Optical Coherence Tomography (SD-OCT) uses a broadband light source, with the spectral profile of the interference signal then providing depth information via Fourier transformation.

Frequency-Domain OCT (FD-OCT) is one form of SD-OCT. A broadband light source is used and directed into the beam splitter. The polychromatic interference signal produced by the returning sample and reference light paths is dispersed into its constituent wavelengths by a diffraction grating

(

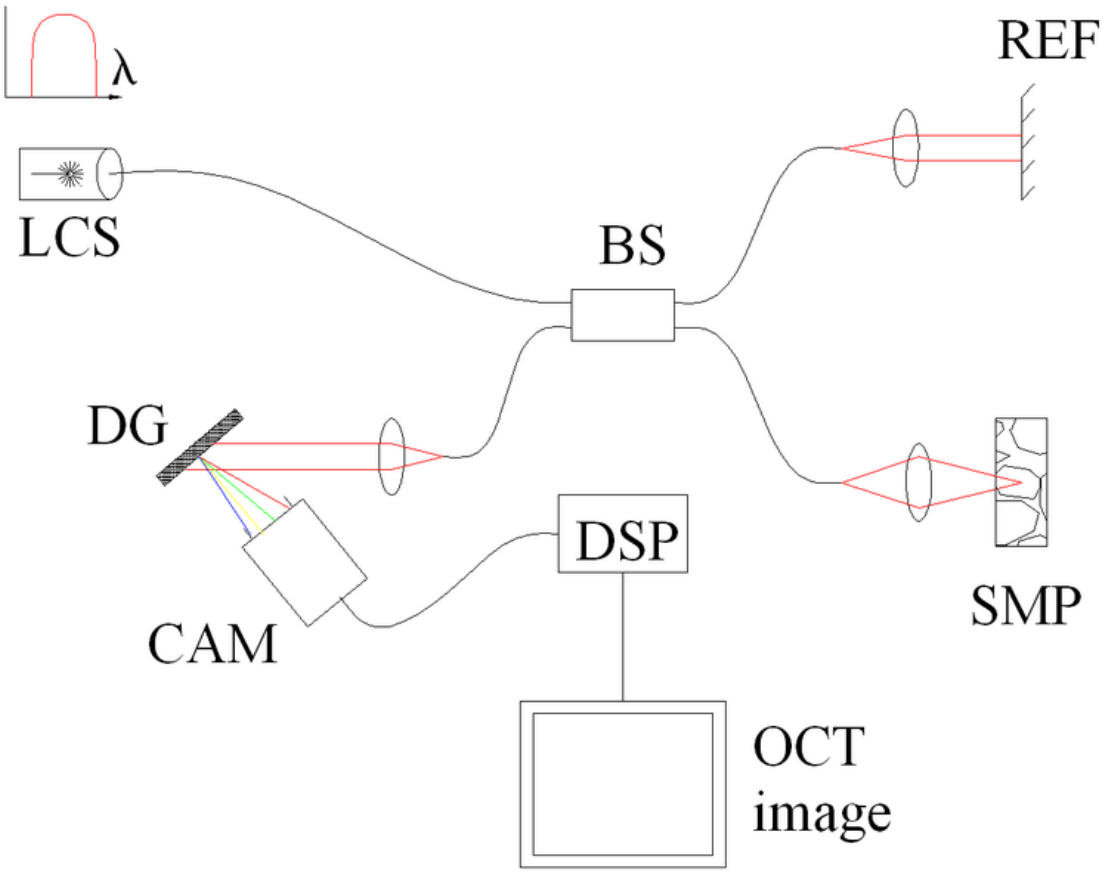

Figure 1-17 -DG) and the separate frequency information measure by an array of detectors. In essence, this allows reflectivity measurements for a range of depths (Z) at a single point in time. The Reference mirror, moved in Time-Domain OCT to provide measurements across a range of depths (Figure 1-16), can thus be fixed.

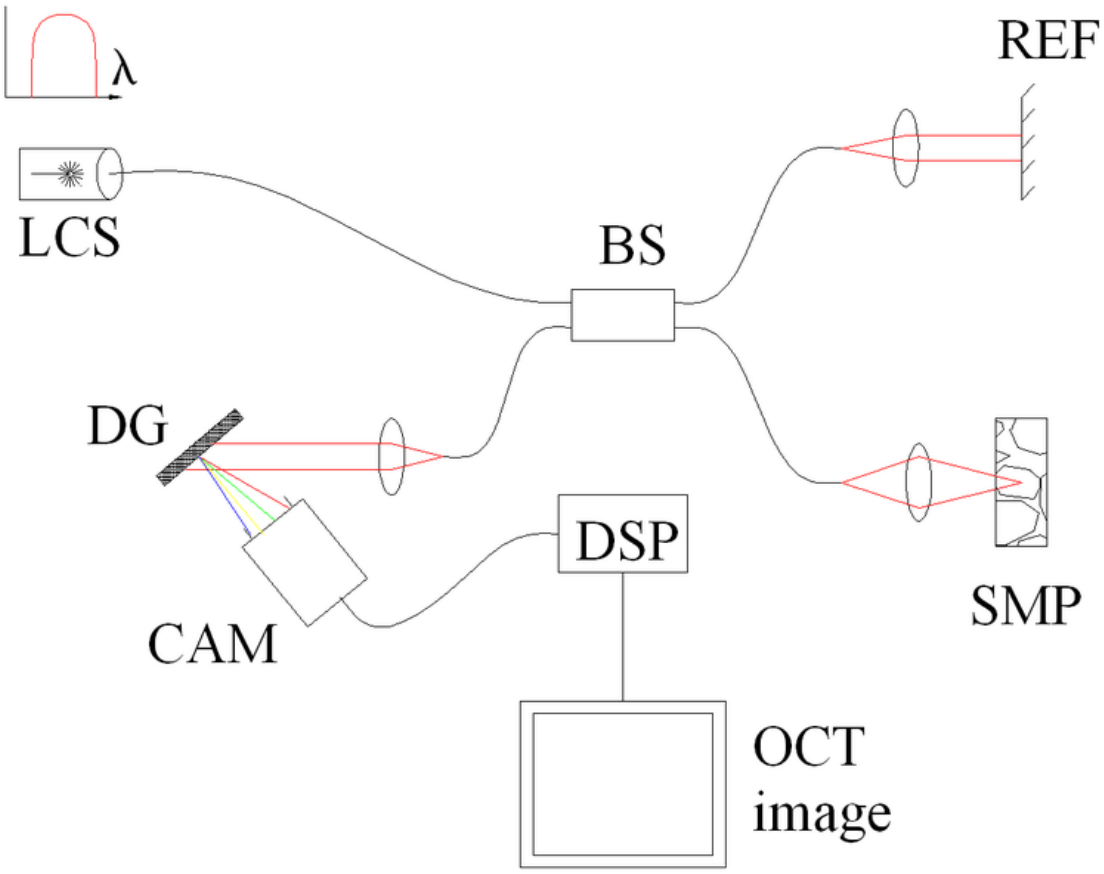

Figure 1-17 - Frequency-Domain OCT illustrating a Broadband light source (LCS), Diffraction Grating (DG), Camera (CAM), Digital Signal Processor (DSP). Sourced from WikiCommons - pumpkinegan

Another approach to SD-OCT removes complexity at the detector by altering the light source. The same spectral information as detected in FD-OCT can be measured by a single, less-expensive photodetector if the source only emits one wavelength of light at any one time, but alters that emitted wavelength across the time domain. This approach is known as swept-source OCT (SS-OCT). When compared to TD-OCT, both approaches have significant scanning speed improvements. They are, however, both affected by a more rapid decrease in signal to noise ratio (SNR) with increased scanning depth.

Clinical applications of OCT generally use one of the Spectral-Domain techniques due to the much shorter acquisition time. Generally, OCT acquisitions will have a

higher spatial resolution in the z-axis (One to five micrometres), while x (and y, if performed) will be limited to 10-20μm. FD-OCT Z-resolution will be largely limited by the number of individual detectors in the detector array, while the introduction of a diffraction grid also reduces the effective SNR at each site. SS-OCT as advantages in terms of SNR, but is much more susceptible to movement artefacts. Scanning depth is limited by the wavelength of light used and the transparency or turbidity of the sample.

1.3.4.1.1 In Otology

OCT for imaging of the cochlea was first described by Wong, et al, in 2000 (B. J. F. Wong, de Boer, Park, Chen, & Nelson, 2000). Wong's group utilised fresh cochleae harvested from rats. The cochleae were not decalcified prior to imaging, but the group were still able to identify internal structures of the rat cochlea including Reissner's and basilar membranes with a spatial resolution of 10-15μm depending on scanning parameters.

The same group improved their scanning depth in 2004 (B. Wong, 2004) by using a higher central wavelength for FD-OCT of 1300nm. This saw depth of scanning increase to up to 2mm, depending on tissue turbidity and was once again performed post-mortem in rats without decalcification. Because of concerns about the feasibility of scanning through thicker bone covering the human cochlea, porcine cochlear OCT was trialled by Sephehr (Sepehr, Djalilian, Chang, Chen, & Wong, 2008), within the same institution. Scanning depth of 2.56mm was achieved, but this was only after extraction of the cochlea and thinning of the bone of the promontory until cochlear endosteum was exposed.

In the areas of thinned bone, all scalae in the adjacent turn, tectorial membranes, Reissner's membranes and basilar membranes were visualised.

In-vivo OCT of the cochlea was first published by Subhash (Subhash et al., 2010), in 2010. In-vivo scanning was performed in an anaesthetised mouse via a ventral bullostomy necessitating removal of the ipsilateral submandibular gland and posterior belly of digastric muscle. A specially constructed FD-OCT scanner was utilised, with a broadband light source with a centre wavelength of 1300nm and a 1024 bin Indium-Gallium-Arsenide (InGaAs) detector. Voxel sizes of ~12x10x10μm were acquired with a 2.45mm scan depth, allowing identification of all scalae, Reissner's and basilar membranes. In-vivo scanning in other species has not been published to this date, though Tona, et al (Tona et al., 2014), have managed to progress the technique such that experimental endolymphatic hydrops can be detected on in-vivo mouse scanning.

Decreasing the turbidity of the tissue will allow for increased scanning depth and less-rapid drop-off in SNR across the depth range. It was through this approach that Kakigi (Kakigi et al., 2013) was able to evaluate both experimentally induced endolymphatic hydrops (through surgical ablation of the endolymphatic sac) and aminoglycoside-related cochlear injury (through either intravenous kanamycin sulfate-ethacrynic acid or perilymphatic infusion of streptomycin) using OCT. After sacrifice, specimens were fixed with 10% neutral buffered formalin over 7 days and decalcified using ethylenediamine tetraacetic acid (EDTA) over a period of 14 days.

FD-OCT was utilised, with a centre wavelength of 1320nm and image depth of 6mm. Z-resolution was 12μm, with X-resolution 17μm. After imaging, samples

were dehydrated in sequential alcohols and embedded in paraffin for histopathological validation of the OCT findings.

Kakigi's group were able to measure the cross-sectional area of scala media in the OCT images from the endolymphatic hydrops group and calculate the percentage area excess when compared to the area of scala media given a straight Reissner's membrane. The same measurement was performed in histological specimens. The group found that there was a statistically significant difference ($p<0.05$) between the area excess measured on OCT and histology for the same animal. Histological examination gave a larger percentage area excess than measurements using OCT. A further difference between OCT and histological examination was seen in animals treated with intravenous kanamycin sulfate - ethacrynic acid (KE), where OCT imaging detected concavity of Reissner's membrane that was not apparent on histopathological examination of the same tissue. Flattening of the organ of Corti was evident using both imaging modalities, but was only measurable on OCT because of slicing artefact present in the paraffin-embedded tissue. In the streptomycin model, designed to produce strial atrophy, both imaging modalities clearly demonstrated strial atrophy and profound collapse of the scala media. Only histopathological examination, however, could identify spiral ganglion neuron (SGN) losses, because of OCTs relatively low spatial resolution.

Another exciting area of progress in OCT's use in Otology is the use of high-frequency dynamic imaging. OCT is capable of scanning at frequencies well in excess of the human range of hearing, unlocking the potential for real-time imaging of cochlear mechanics. This has recently been demonstrated by Alfred

Nuttall's group, in both in-vivo (Ramamoorthy et al., 2013) and ex-vivo (Choudhury et al., 2011) guinea-pig cochleae. Basilar membrane movements of down to 0.001nm were visible on specialised FD-OCT viewing the basilar membrane through the RWM via a bullostomy.

1.4 Conceptual Framework for the work and an outline of the intended methods

The cochlea is a highly complex structure, susceptible to a wide variety of insults. As the number and variety of interventions designed to protect or restore cochlear function have increased, so has the recognition that these processes can themselves be injurious to cochlear function.

Examination of existing imaging techniques and their applicability to the examination of inner ear pathology after therapeutic interventions will allow identification of their respective pitfalls and the formation of a bank of techniques allowing imaging most appropriate to the pathological process being studied.

A guinea-pig model will be used for all experiments because models of the relevant pathological processes are well established and the department has considerable experience in examination of guinea-pig otopathology using conventional histological techniques.

The imaging methods to be utilised in this body of work will include micro-CT, optical coherence tomography and thin-sheet LASER microscopy.

2 General and Expanded Methods

2.1 Animal Procedures

2.1.1 Guinea Pig Anaesthesia

Animals were anaesthetised for all surgical and electrophysiological procedures using a combination of intramuscular injection of ketamine (60 mg/kg, Troy Laboratories Pty Ltd, Sydney, Australia) and xylazine (4 mg/kg, Troy Laboratories Pty Ltd) as per institutional protocol.

2.1.2 ABR Measurements

ABR Measurements were performed with the animal anaesthetised using intramuscular ketamine and xylazine as previously described. The ABR recording system has been described in previous publications (Shepherd, Clark, & Black, 1983). Acoustic stimuli consisted of clicks and tone pips (5ms total duration including 1ms rise/fall), with the tone pips presented at frequencies of 2, 4, 8, 16 and 24kHz. The stimuli were generated using custom software (developed by Rodney Millard) and delivered via a loudspeaker (Richard Allen DT-20, UK) situated 10cm from the external auditory canal, with the contralateral external auditory canal occluded using Otoform moulding compound (Dreve, Germany). Stimuli were repeated 250 times per intensity, at a rate of 30 presentations per second. High stimulus levels were used initially, with the stimulus intensity then reduced by 5dB each run.

Subcutaneous differential recording electrodes were placed at the nape of the neck and the vertex, with a grounding electrode placed on the animal's flank. Responses were pre-amplified by a factor of 1000 (DAM-5A, W-P Instruments Inc, New Haven, USA), and then band-pass filtered between 150 Hz and 3 kHz (Krohn-Hite 3750, Avon, USA). The filtered output was amplified again by a factor of 100 by a custom-made amplifier, then passed to a 16-bit analogue-to-digital converter (Tucker Davis Technologies, USA) and sampled at 20 kHz for 10 ms after stimulus onset. Responses were averaged across the 250 repetitions. The averaged waveforms were analysed using custom routines in Igor Pro 5.0.2 (Wavemetrics Inc.). ABR Threshold was defined as the lowest stimulus intensity that produced a response where the amplitude of wave III was greater than 0.4μV.

2.1.3 Cochlear Implantation

The procedure for cochlear implantation has been described in detail elsewhere (Smeds et al., 2015) (James, Eastwood, Richardson, & O'Leary, 2008) (Connolly et al., 2011). Local anaesthetic, lignocaine (1 mg/mL, Troy Laboratories Pty Ltd) was injected subcutaneously at the surgical site prior to incision. The cochlea was then approached via a post-auricular skin incision, division of the post-auricular muscles and fenestration of the dorsal tympanic bulla to allow a direct microscopic view of the RWM. A cochleostomy was created anteroinferior to the round window using a 0.8 mm diamond bur drill. Soft-surgical principles were employed, including avoidance of suctioning of perilymph or introduction of bone dust . A dummy cochlear implant electrode, made of Silastic® (MDX4-4210; Dow Corning Products, USA), and with a diameter of 0.4 mm, was introduced

~2.5 mm into scala tympani, or until first resistance was met. This electrode was constructed without platinum electrode bands, in order to minimise artefact during micro-CT. The cochleostomy was sealed with fascia and the incision was closed in layers using absorbable suture material (Vicryl; Ethicon, New Brunswick, NJ). The wound was covered with an aerosolised occlusive dressing (OpSite Spray; Smith & Nephew, London, England).

2.1.4 Pump Surgery

A mini-osmotic pump (Model 2004; Alzet, Cupertino, California) was prepared according to manufacturer instructions. This particular model of pump was selected for use because of its delivery duration of 28 days, with a flow-rate of 0.25µL/day. The pump was to be filled using a micro-syringe with either 200µL of artifical perilymph (AP - Table 2-1) solution (Bobbin, Jastreboff, Fallon, & Littman, 1990; Jenison, Bobbin, & Thalmann, 1985; Robertson & Paki, 2002), or artificial perilymph solution containing 12µg of brain-derived neurotrophic factor (BDNF). Artifical perilymph solution was prepared as per Table 2-1 and combined with guinea pig albumin (Sigma-Aldrich, St Louis, USA) to make a 1% solution. The prepared solution was then filtered through a 0.2µm membrane filter (Acrodisc 32mm, 0.2µm; Pall Corporation, Cornwall UK) and transferred to vials in 200µL aliquots using a micro-syringe (SGE Analytical Science Pty Ltd, Ringwood, Victoria). In the case of animals receiving BDNF treatment, 12µg of BDNF (Peprotech, Rocky Hill, NJ, USA) was added to the GPA:AP solution, and the solution mixed in a vortex. All vials were briefly centrifuged to collect the mixed solutions into a single volume and the contents then transferred to the bladder of

the mini-osmotic pump using a clean micro-syringe, taking care to fill the pump bladder from the bottom to ensure no air-bubbles were formed. Once the bladder was seen to be filled, the flow-regulator was attached and the complete pump placed regulator-upwards in a sterile 50ml tube containing 5ml of sterile saline such that the regulator was above the level of the normal saline. The filled pumps were stored at 37°C until implantation surgery was performed the following day.

Table 2-1 - Composition of srtificial perilymph solution utilised, after Jenison GL, et al (1985)(Jenison et al., 1985).

Solute	**Concentration (mM)**
Sodium chloride (NaCl)	137
Potassium chloride (KCl)	5
Calcium chloride ($CaCl_2$)	2
Magnesium chloride ($MgCl_2$)	1
Monosodium phosphate (NaH_2PO_4)	1
Sodium bicarbonate ($NaHCO_3$)	12
Glucose	10

The post-auricular skin was prepared using chlorhexidine (0.5% w/v in alcohol 70% w/v; Avagard, 3M, St Paul, USA) and then infiltrated with 1% lignocaine for local anaesthesia. A post-auricular skin incision was made, followed by division of the post-auricular musculature. Dorsal bullostomy was performed using an

11-blade (Swann-Morton, Sheffield, UK) to avoid acoustic trauma from drilling (Pau, Just, Bornitz, Lasurashvilli, & Zahnert, 2007).

A mini-osmotic pump (Model 2004; Alzet, Cupertino, California) was prepared according to manufacturer instructions. This particular model of pump was selected for use because of its delivery duration of 28 days, with a flow-rate of 0.25 µL/hour. The pump was filled using a micro-syringe with either 200 µL of AP solution (Bobbin et al., 1990; Jenison et al., 1985; Robertson & Paki, 2002; S. Y. Zhang, Robertson, Yates, & Everett, 1999), composed as per Table 2-1 ,or 200 µL BDNF solution containing 12 µg of BDNF (Cat #450-02; Lot #071161J1112 and 061361F0914, Peprotech, Rocky Hill, NJ, USA).

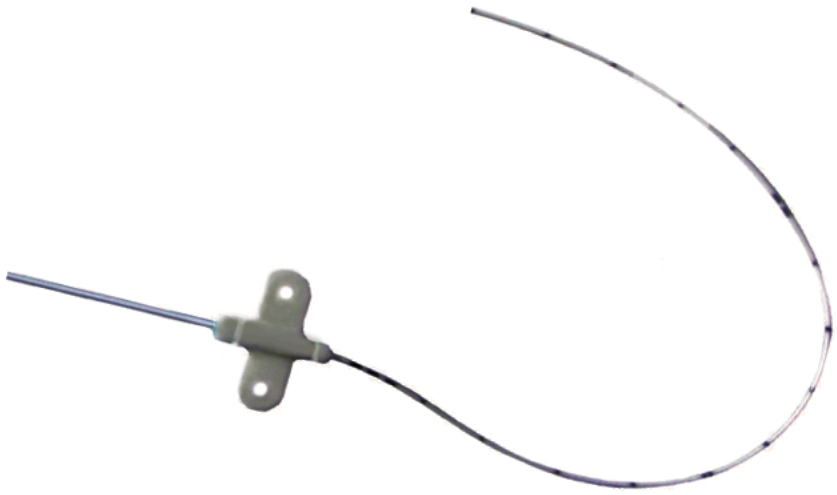

Figure 2-1 - 1Fr Polyurethane neonatal central venous catheter, modified for use as a Round Window Niche Microcatheter in a guinea pig.

A 1Fr neonatal central venous catheter (Premicath 1Fr; Vygon, Ecouen, France) was used as the drug-delivery conduit after some modifications ((Shepherd et al., 1983)). The proximal Luer fitting was removed to allow direct attachment of the mini-osmotic pump (Figure 2-1). The intravascular portion of the device was

shortened to suit the size of the individual animal, allowing for unimpeded neck movements and the formation of a tension-relief loop on the external surface of the dorsal tympanic bulla.

The end of the catheter was placed in the round window niche, without placing pressure on the RWM itself. Once positioned, the catheter was secured to the margin of the bullostomy using a drop of cyanoacrylate cement (3M, St Paul, MN). Once the cyanoacrylate cement had cured, two-part carboxylate dental cement (Durelon; 3M, St Paul, MN) was used to further secure the catheter to the tympanic bulla, as well as to form a tension-relieving loop in the catheter. The catheter was primed with the same solution as loaded in the mini-osmotic pump using a micro-syringe (Microliter 700 Series; Hamilton, Reno, NV), then connected to the mini-osmotic pump. Blunt dissection of a tunnel within the interscapular subcutaneous fat of the guinea pig was performed, then the mini-osmotic pump inserted. The incision was closed in layers using absorbable suture material (Vicryl; Ethicon, New Brunswick, NJ) and the wound covered with an aerosolised occlusive dressing (OpSite Spray; Smith & Nephew, London, England).

2.1.5 Pump Removal

Guinea pigs were anaesthetised as previously described, then euthanased as described in *Specimen Preparation for OCT*. A skin incision was made over the nape of the neck, and blunt dissection performed caudally to identify the mini-osmotic pump. The mini-osmotic pump was examined to ensure that the bladder had emptied and thus its contents delivered. The delivery catheter was then disconnected from the mini-osmotic pump and connected to a micro-syringe containing normal saline. An aural speculum was placed in the external

auditory canal of the guinea pig and the tympanic membrane examined using an operating microscope (Karl Storz, Tuttlingen, Germany). A myringotomy was performed using a 25-gauge hypodermic needle (Precision-Glide 305127; BD, USA), then the catheter slowly flushed with normal saline to confirm that the catheter tip had remained both patent and correctly located in the round window niche.

2.1.6 LPS Administration

Lipopolysaccharides derived from *Escherichia coli* 055:B5 were prepared as a 1mg/ml solution. Intraperitoneal injections were performed under general anaesthesia as previously described. 0.8ml/kg of the 1mg/ml LPS solution was injected intraperitoneally.

Intratympanic injections were performed under general anaesthesia as previously described.

The guinea pig was placed in a lateral position and a paediatric ear speculum was inserted into the external auditory canal to gain a view of the tympanic membrane through an operating microscope. After toileting of cerumen, the anteroinferior portion of the tympanic membrane was incised with a 25-gauge needle (Precision-Glide 305127; BD, USA), and the middle ear space slowly filled with 1mg/ml LPS solution (left ear) or 0.9% Saline solution (right ear) until it spilled from the myringotomy site. After each injection, the animal was left in the lateral position for 5 minutes before being moved.

2.1.7 Evans Blue Dye Administration

4ml/kg of 2% Evans Blue dye in 0.9% saline was prepared in a 3ml Luer-lock syringe. The Evans Blue syringe was connected to a three-way tap along with a a second syringe containing only 0.9% saline.

After initiation of anaesthesia using intramuscular ketamine and xylazine as previously described, the animal was placed in the supine position. Infiltration with 1% Lignocaine was performed on the left side of the neck and a ventral neck incision made. Blunt dissection was performed to expose the internal jugular vein, which was skeletonised along a 5mm length. 2-0 Silk (Ethicon, New Brunswick, NJ) ligatures were placed around the vein cranially and caudally to control the vessel while a venotomy was performed using microsurgical scissors. The cranially positioned ligature was tightened to prevent bleeding while a 1-French-Gauge catheter, attached to the three-way tap, was inserted caudally into the venotomy. Once the catheter position had been confirmed by aspiration of venous blood, the caudal ligature was tightened to help retain the catheter. The Evans Blue dye solution was injected over a 10 second period, followed by 2ml of 0.9% Saline to flush the catheter. Prompt blue discolouration of the animals' peripheries (all four feet, gingiva) without other physiological perturbation was considered evidence of successful Evans Blue infusion.

The catheter was then removed, the ligatures tightened and tied, and the wound closed with cyanoacrylate glue.

2.2 Specimen Preparation Procedures

2.2.1 Specimen Preparation for µCT

After the final electrophysiological recording, animals were euthanised under general anaesthesia as previously described. Pentobarbital (200mg/kg) was administered by intraperitoneal injection, with transcardial perfusion of 0.9% saline followed by 10% neutral buffered formalin after respiratory arrest. Cochleae were harvested and then immersed in 19% neutral buffered formalin for a further 24 hours.

After fixation, a small apical fenestration of the scalae was performed using a 25-gauge needle and bone removed overlying the semicircular canals to facilitate staining. Cochleae were immersed in a solution of 4% Osmium Tetroxide and agitated for 48 hours to increase the radio-opacity of intracochlear soft tissues.

Prior to mounting the specimen on the µCT stage, the specimen was wrapped in paraffin (Parafilm; Bemis Co, USA) to prevent contamination of the apparatus with Osmium salts.

2.2.2 Specimen Preparation for TSLIM

30 minutes after administration of intravascular Evans Blue, animals were euthanised under general anaesthesia as previously described. Pentobarbital (200mg/kg) was administered by intraperitoneal injection, with transcardial perfusion of 0.9% saline followed by 4% paraformaldehyde (Mallinckrodt Baker Inc., Phillipsburg, NJ, USA) after respiratory arrest. Cochleae were harvested and then immersed in 10% neutral buffered formalin for a further 24 hours.

After fixation, cochleae were trimmed and transferred to 10% EDTA in PBS, with 72-hourly changes until decalcification was complete.

The dummy electrodes were carefully removed and then the cochleae were bleached by immersion in 5% Hydrogen Peroxide solution for 24 hours. Following bleaching, the cochleae were dehydrated in sequential alcohols as per Table 2-2 - Sequential Alcohol Dehydration Stages in preparation for TSLIM (Cheol Hee Choi et al., 2012; Jang et al., 2011; Schmutzhard et al., 2012; T. Suzuki et al., 2008).

Table 2-2 - Sequential Alcohol Dehydration Stages in preparation for TSLIM

Stage	Solution	Duration
1	50% Ethanol	30 minutes
2	70% Ethanol	30 minutes
3	90% Ethanol	30 minutes
4	90% Ethanol	30 minutes
5	100% Ethanol	30 minutes
6	100% Ethanol	30 minutes

The dehydrated cochleae were immersed in an organic solvent (n-heptane) for 30 minutes prior to being transferred to Spalteholz fluid; consisting of 5:3 methylsalicylate and benzyl-benzoate (Sigma-Aldrich, St Louis, USA). Cochleae were stored in Spalteholz fluid for at least 24 hours prior to TSLIM imaging. If cochlea were to be stored for a longer period of time, this was done in a light- and air-tight container.

Prior to imaging, cochleae were mounted on a bamboo skewer using a two-component epoxy cement (Araldite; Selleys, Australia) and placed in a vacuum chamber to remove air bubbles.

2.2.3 Specimen Preparation for OCT

After the final ABR recording, animals were euthanised under general anaesthesia as previously described. Pentobarbital (200mg/kg) was administered by intraperitoneal injection, with transcardial perfusion with 0.9% saline followed by 4% paraformaldehyde (Mallinckrodt Baker Inc., Phillipsburg, NJ, USA) after respiratory arrest. Cochleae were harvested and then immersed in 10% neutral buffered formalin for a further 24 hours.

Specimens were then washed in phosphate buffered saline (PBS) prior to being decalcified using a rapid decalcifying solution (RDO; Apex Engineering Products, USA). Specimens were immersed in the decalcifying solution and placed within a vacuum chamber. The vacuum was evacuated and then repressurised for four cycles, after which further trimming was performed. A further two vacuum cycles were then performed. The specimens were removed from the decalcifying solution and then rinsed thoroughly in PBS.

2.2.4 Specimen Preparation for LSCM

The already decalcified tissue was dissected into half-turns. The lateral wall, modiolar remnant and tectorial membrane were excised and then the resulting ~11 pieces photographed on a light microscope.

Using a plug-in (http:// www.masseyeandear.org/research/ent/eaton-peabody/epl-histology-resources/) for ImageJ (NIH, Maryland, USA) developed by Liberman's group at the Massachusetts Eye and Ear Infirmary, distances along the cochlear spiral for each piece of tissue were calculated and a guinea pig specific (Tsuji & Liberman, 1997) frequency-place map generated for the dissected tissue.

The piece of tissue corresponding to the 16kHz region on the frequency-place map was selected for whole-mount confocal microscopy.

Half-turn whole-mounts were washed in 0.01M PBS and then preincubated at room temperature for 1 hour in blocking solution of 4% normal horse serum (Life Technologies, Carlsbad, CA) in 0.01M PBS with 0.1% Triton X-100 (Sigma-Aldrich, St Louis, MO). Specimens were then incubated overnight at 37˚C in a solution of myosin VIIa primary antibody at 1:50 dilution before being washed three times for five minutes in 0.01M PBS. Biotinylated horse anti-rabbit IgG was then added at 1:200 dilution for one hour at room temperature and then the specimen washed again in 0.01M PBS. Alexa Fluor® 568-conjugated streptavidin (Life Technologies, Carlsbad, CA) was used for detection, with the specimen placed in a 1:1000 dilution for one hour at room temperature. After three further washes in 0.01M PBS, DAPI was added at 1:10 dilution for 10 minutes for nuclear detection. Three further washes were performed before the specimens were mounted in glycerol.

2.3 Image Acquisition Procedures

2.3.1 TSLIM Acquisition

Our TSLIM apparatus is demonstrated diagrammatically in Figure 2-2 - Diagrammatic representation of our TSLIM apparatus demonstrating the split beamline for reduced light sheet fall-off

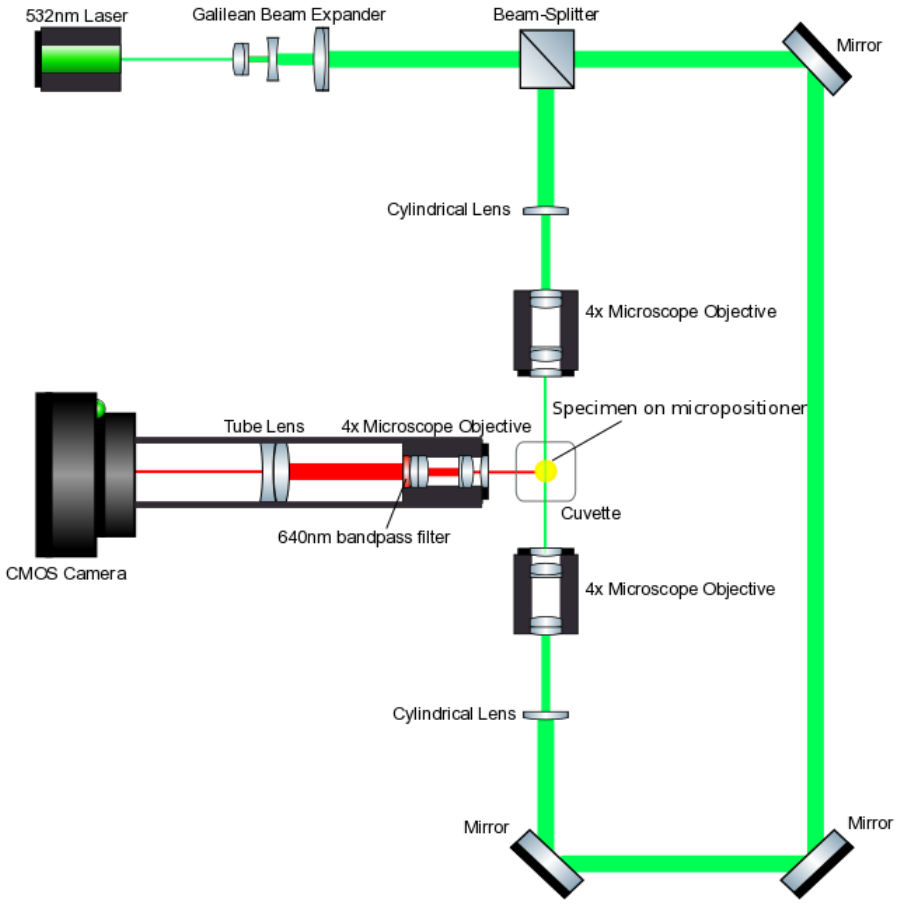

Figure 2-2 - Diagrammatic representation of our TSLIM apparatus demonstrating the split beamline for reduced light sheet fall-off

The apparatus can be thought of as three main components:

1. Specimen preservation and positioning apparatus

a. The specimen is kept immersed in Spalteholz fluid within a custom-manufactured (20mm x 20mm x 20mm) cuvette with quartz-crystal walls of uniform thickness (2mm).
b. The specimen is suspended in the Spalteholz fluid from a bamboo skewer, held by an instrument arm above.
c. The instrument arm is attached to a 3-axis micropositioning system (ThorLabs, Newton, USA), with individual control modules attached to a computer via USB.

2. Light-Sheet generation apparatus
    a. The light sheet begins as a Gaussian beam emitted by a solid-state LASER module (manufacturer, Luke).
    b. The diameter of the Gaussian beam is expanded by a 10x Galilean beam expander (BE10M-A; Thorlabs, USA)
    c. The expanded beam is focused in one dimension by a cylindrical lens (LJ1821L2-A; Thorlabs, USA).
    d. The sheet of LASER light is then further focused by a microscope objective (M-PLAN; Olympus, Japan).
    e. The specimen, within the Spalteholz-fluid-filled cuvette, is placed within the confocal region of the focused light sheet.
3. Image acquisition apparatus
    a. The emission image is magnified by an infinity-corrected microscope objective (M-PLAN; Olympus, Japan).
    b. A bandpass filter with centre-wavelength 640nm filters the image to exclude tissue autofluorescence.

c. A 200mm tube lens refocusses the infinity-corrected input onto the imaging plane.
d. The resulting image is captured by a 20.2 megapixel CMOS sensor (EOS 70D; Canon, Japan).

The specimens were mounted and the X, Y, Z ranges required to image the cochlea identified utilising custom software to control the micro-positioning stepper motors whilst viewing an unfiltered acquisition via Live View. A 4x M-Plan Objective was utilised on the acquisition apparatus as a compromise between desired spatial resolution and acquisition time. 10x M-Plan Objectives were used in the light-sheet generation apparatus.

Because only a portion of the x dimension of the acquired image was within the confocal range of the 10x light sheet, multiple, overlapping exposures were performed in the x dimension (x-step of 1mm) to allow later selection and stitching of the acceptably sharp portion of the images into a composite. Similarly, multiple images were acquired in the y dimension (y-step of 2mm) because the acquired image included the edges of the converging light-sheet when a 4x acquisition objective was used. The evenly illuminated, central portions (y dimension) of the frames could then be selected for stitching of a composite image. z-distance between slices was set at 10μm. A 640nm bandpass emission filter (FB640-10; ThorLabs, USA) was then inserted into the acquisition apparatus prior to commencing the automated scan protocol.

2.3.2 µCT Acquisition

The specimens were imaged using an XRadia MicroXCT-200 scanner (XRadia, Concord, CA). Nine second exposures, with source parameters of 60kV and 10W were performed. 361 projections were performed, with the cochlea rotated by 0.5 degrees between exposures. Detector binning reduced the detector resolution to 1024x1024 pixels. Proprietary tomographic reconstruction software (XReconstructor - XRadia, Concord, CA) was utilised to form a three-dimensional volume from the projections, with correction for drift of the subject, beam-hardening and ring-artefact. This generated a volume of 1024x1024x1024 isotropic voxels, each with a sidelength of 5.2µm given a 4x magnification objective, 100mm source-sample distance and 22mm sample-detector distance. The volume was sliced, and exported for visualisation in other software packages.

2.3.3 OCT Acquisition

OCT Acquisitions were performed using a Spectral-Domain OCT (Spectralis OCT; Heidelberg Engineering, Germany) retinal imager adapted for cochlear imaging using an additional 78-diopter double-aspheric lens.

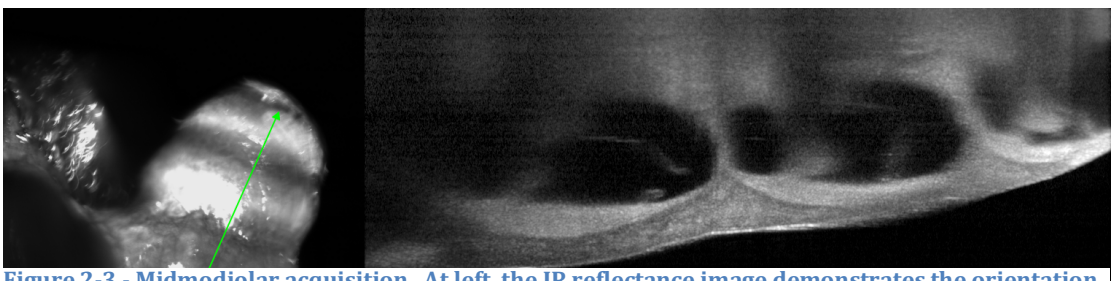

Figure 2-3 - Midmodiolar acquisition. At left, the IR reflectance image demonstrates the orientation of the OCT acquisition, with the arrowhead indicating the right end of the OCT image

The cochleae were mounted in front of the 78-diopter double-aspheric lens with the modiolus oriented vertically. One acquisition was performed in a mid-modiolar plane adjacent the promontory (Figure 2-3), then the specimen was rotated such that the imaging plane bisected the round window membrane (Figure 2-4).

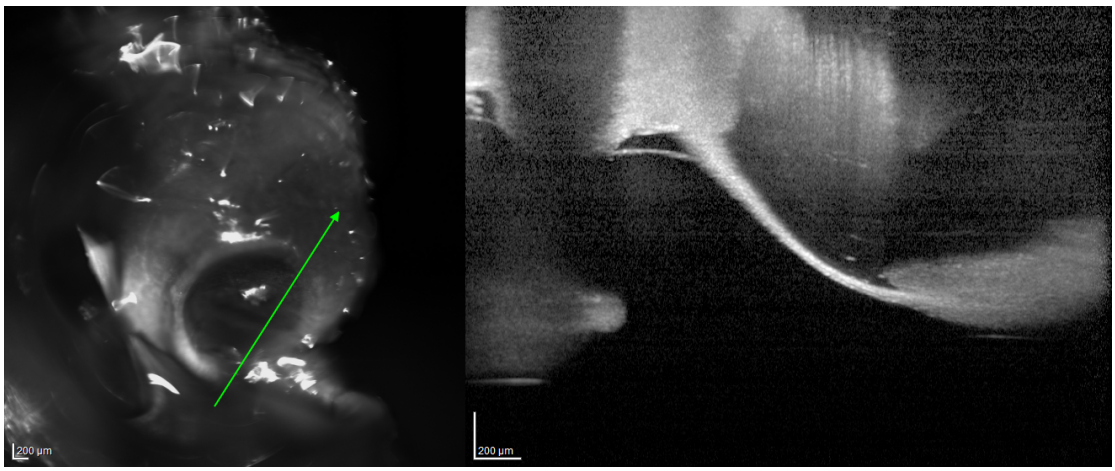

Figure 2-4 - Round Window Membrane acquisition. The IR reflectance image at left demonstrates the straight-on view of the RWM with correct specimen positioning to facilitate accurate measurements of RWM thickness.

2.3.4 LSCM Acquisition

LSCM Acquisitions were performed on a Nikon A1R confocal microscope, using the DAPI, TRITC and AF568 LASER lines. A Nikon CFI Plan Apochromatic 20x objective was utilised, with no digital zoom. Z-stacks were acquired to ensure imaging of the full depth of the Organ of Corti.

2.4 Analytical Procedures

2.4.1 LSCM

2.4.1.1 Hair Cell Counts

LSCM acquisitions were imported into NIS Elements Viewer (Nikon, Tokyo, Japan). A region of interest of 30 rows of hair cells was considered. This region of interest was randomly determined to begin at the left or right border of the LSCM stack, unless a contiguous sample could not be made at one border because of the presence of processing artefacts.

Inner hair cells locations were examined for DAPI and/or MyosinVIIa fluorescence, and their status recorded as present or absent.

2.4.2 OCT

2.4.2.1 Round Window Membrane Thickness

Measurements of the thickness of the round window membrane were performed using the two-dimensional distance measuring tool within Heidelberg Eye Explorer (HEYEX – Heidelberg Engineering, Heidelberg, Germany). Measurements were performed through the centre of the round window membrane as identified on the Spectralis OCT's infrared reflectance image. Measurements were performed at five points around the centre of the membrane and a mean thickness determined for each specimen.

2.4.2.2 Reissner's Membrane Position

Determination of the position of Reissner's membrane was performed on a transmodiolar section through the promontory, as identified on the Spectralis OCT's infrared reflectance image.

2.4.3 µCT

Analysis of µCT data was performed primarily in Amira (versions 5 through 5.6; Visualization Sciences Group, Bordeaux, France) on an Apple Mac Pro (Apple Computer, Cupertino, CA) desktop computer running Mac OS X 10.8.4. Simpler computational tasks were often delegated to a Dell Precision T3600 (Dell, Round Rock, TX) desktop computer running Windows 7 (Microsoft, Redmond, WA).

Luminosity data was imported from the stack of slices generated by XReconstructor, with the dimensions of the voxels to be imported into Amira provided by the metadata inspector.

Micro-CT voxels are usually isotropic, and in our case each side measured 5.2µm as previously described (see 2.3.2 - µCT Acquisition).

Non Local Means (NLM) Noise-Reduction (see also Appendix 7.1 – *Non Local Means Filtering*) was performed upon all imported µCT datasets. Two-dimensional NLM filtering was performed, with a search window of 30 voxels, a local neighbourhood of 6 voxels and a similarity value of 0.5. Amira was allowed to calculate the block size appropriate to the CUDA (Nvidia, Santa Clara, CA) GPGPU device allocated to the task.

Discussion of analysis performed is continued in *Experiment 2 – Evaluating Endolymphatic Hydrops and Tissue-Response after Cochlear Implantation using μCT.*

2.4.4 TSLIM

2.4.4.1 Quantification of Evans Blue Extravasation

Evans Blue extravasation was quantified by measuring its fluorescence on TSLIM.

TSLIM acquisitions were performed with a 640nm (+/- 2nm) bandpass filter (FB640-10 – ThorLabs, Newton, MA) to quantify Evans Blue using its primary emission peak when stimulated by a 532nm diode LASER. Camera sensitivity was set at ISO 1600, with a 2 second exposure. XYZ stitching of multiple acquisitions for each slice was performed to allow imaging of the entire cross-section of the cochlea using the confocal region of the LASER sheet. A second set of acquisitions was performed without an emission filter to allow imaging of anatomical details through tissue autofluorescence. XYZ stitching was again performed, with the same volume imaged to allow for easy co-registration of datasets in Amira.

The datasets were imported into Amira in two different ways. Only the Luminance data was imported from the emission-filtered dataset, whilst the unfiltered acquisition was imported in its entirety as an RGBA (Red-Green-Blue-Alpha) data object. Voxel dimensions were the same for both datasets because of the identical stitching and slicing parameters.

Using the superior anatomical detail available in the RGBA dataset, a BSpline was generated to trace the organ of Corti, in a method identical to that described previously for µCT (*µCT - Tonotopic Mapping*). Further BSplines were generated marking the positions of the following structures along the length of the cochlear duct:

1. Spiral limbus
2. Type II fibrocyte region of lateral wall
3. Type IV fibrocyte region of lateral wall

The defined BSplines were connected to LineSetProbe modules to determine the luminance value for the emission-filtered dataset centered on the BSpline and at any distance along the BSpline.

Further detail of data preparation and analysis is included in *Experiment 3 – Changes in Cochlear Vascular Permeability after Cochlear Implantation visualised using TSLIM*

3 Experiment 1 – Cannula-based drug delivery to the guinea pig round window causes a lasting hearing loss that may be temporarily mitigated by BDNF

3.1 Introduction

Guinea pigs will be implanted with flexible round window niche (RWN) cannulas that will deliver either artificial perilymph (AP) or brain-derived neurotrophic factor (BDNF) in an artificial perilymph carrier. Control animals will be implanted with an RWN cannula that will not deliver any fluid.

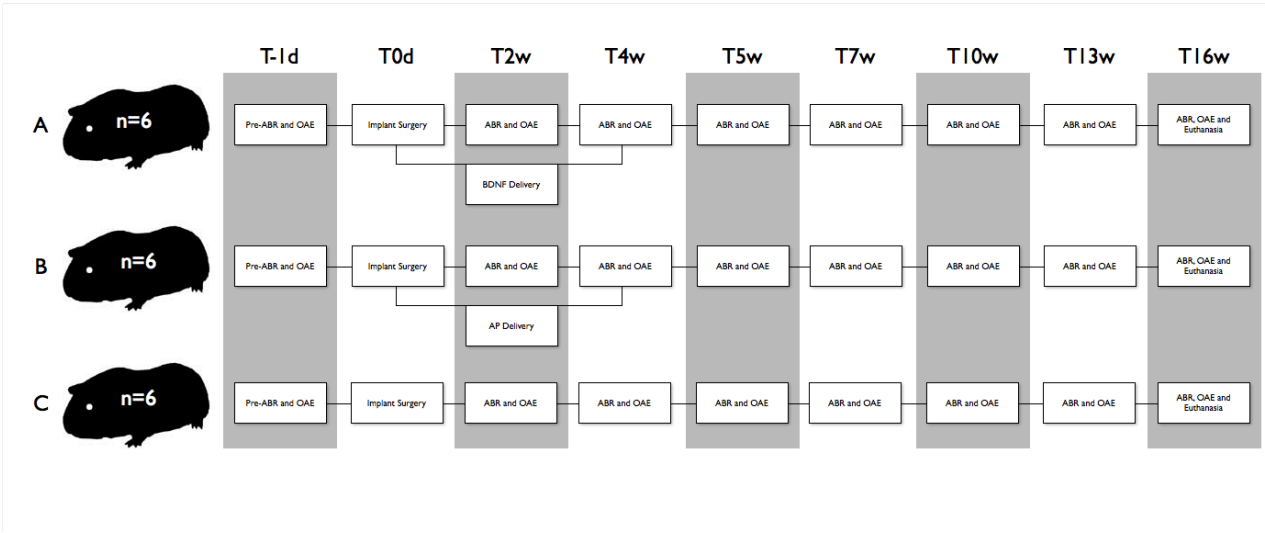

Figure 3-1 - Timeline and grouping for Experiment 1

Hearing measures will be performed at multiple time points and the animals sacrificed at 16 weeks post-op. Optical Coherence Tomography will be utilised for non-destructive, qualitative measurement of the position of Reissner's membrane along with measurement of the thickness of the round window membrane.

3.2 Abstract

Sustained local delivery of drugs to the inner ear may be required for future regenerative and protective strategies. The round window is surgically accessible and a promising delivery route. To be viable, a delivery system should not cause hearing loss. This study determined the effect on hearing of placing a drug-delivery microcatheter on to the round window, and delivering either artificial perilymph (AP) or brain-derived neurotrophic factor (BDNF) via this catheter with a mini-osmotic pump. Auditory brainstem responses (ABRs) were monitored for 4 months after surgery, while the AP or BDNF was administered for the first month. The presence of the microcatheter – whether dry or when delivering AP or BDNF for 4 weeks– was associated with an increase in ABR thresholds of up to 15 dB, 16 weeks after implantation. This threshold shift was, in part, delayed by the delivery of BDNF. We conclude that the chronic presence of a microcatheter in the round window niche causes hearing loss, and that this is exacerbated by delivery of AP, and ameliorated temporarily by delivery of BDNF.

3.3 Introduction

The optimal method for local drug administration to the inner ear has not yet been established. Sustained drug delivery via the semi permeable round window membrane (RWM) (Goycoolea & Lundman, 1997) is a promising approach, but not without its challenges. Persistence of the drug to be delivered at the middle ear surface of the RWM

is required for sustained delivery (Salt, Hartsock, Plontke, LeBel, & Piu, 2011). Varied attempts have been made at increasing this persistence through the use of sustained release biodegradable-solid (Plontke, Glien, Rahne, Mäder, & Salt, 2014; Silverstein, Arruda, Rosenberg, Deems, & Hester, 1999) or viscous carriers (Endo et al., 2005; Salt et al., 2011), such as hydrogels (Piu et al., 2011). Other methods have involved repeated or continuous administration of liquid compounds (Cayé Thomasen et al., 2009; Wagner, Cayé Thomasen, Laurell, Bagger-Sjöbäck, & Thomsen, 2005). One method of achieving continuous administration over a prolonged time course involves the use of a microcatheter placed adjacent to the RWM in its bony niche, connected to a drug delivery pump. This method has seen success in the delivery of glucocorticoids (Lefebvre & Staecker, 2002), aminoglycosides (DeCicco et al., 1998) and neurotrophins (Goycoolea & Lundman, 1997; Sly et al., 2012). This method offers the advantage of a predictable duration of delivery, with a consistent concentration of drug present at the delivery site during that time.

There is a paucity of literature regarding potential adverse local effects of continuous or repeated drug administration to the round window niche. Middle ear granulations have been noted after microcatheter delivery of concentrated glucocorticoids in humans (Plontke, Zimmermann, Zenner, & Löwenheim, 2006; Salt et al., 2011), though the authors suggested that mobility of the catheter due to inadequate fixation was the likely stimulus. Thickening and inflammation of the RWM was noted after repeated intratympanic instillation of hydrocortisone solution (Nordang, Linder, & Anniko, 2003; Plontke et al., 2014; Silverstein et al., 1999) in rats, though this effect was thought to be due to the specific compound, as instillation of dexamethasone in the same manner

resulted in no such changes. Thickening of the RWM has also been seen in response to application of polymyxin E, as well as combination medications (Cortisporin; Monarch Pharmaceuticals, Bristol, USA) containing bacitracin, neomycin, polymyxin B and hydrocortisone, with no thickening in response to triamcinolone or cefmenoxime (Endo et al., 2005; Ikeda, Morizono, & Takasaka, 1991; Salt et al., 2011). Experimental stiffening or obliteration of the round window may cause a cochlear conductive hearing loss in guinea pigs (Nageris et al., 2012; Piu et al., 2011), with similar losses seen in human patients with congenital or acquired immobility or obliteration of the RWM (Cayé Thomasen et al., 2009; T. E. Linder et al., 2003; Wagner et al., 2005). The primary aim of this paper is to determine whether chronic drug delivery via a microcatheter approach can be performed without risk to hearing. This is important in order to ascertain whether drugs can be applied long-term to the RWM, in order to prevent or treat hearing loss.

One class of proteins with therapeutic potential are the neurotrophins (Cunningham & Tucci, 2015; Lefebvre & Staecker, 2002; Sly et al., 2012; Wan, Gómez-Casati, Gigliello, Liberman, & Corfas, 2014). Brain-derived neurotrophic factor (BDNF) and neurotrophin-3 (NT-3) are of particular interest in inner ear therapeutics, as they have been demonstrated to be critical to the development and neuronal organisation of the cochlea (DeCicco et al., 1998; Staecker, Galinovic-Schwartz, et al., 1996a; Staecker, Van De Water, et al., 1996c). Both have been shown to aid survival of spiral ganglion neurons in experimental deafness models (Endo et al., 2005; Gillespie, Clark, Bartlett, & Marzella, 2003; Miller et al., n.d.; Noushi, Richardson, Hardman, Clark, & O'Leary, 2005; Staecker, Kopke, Malgrange, Lefebvre, & Van De Water, 1996b), with BDNF also having been shown to improve ABR thresholds beyond baseline at high frequencies in normal-

hearing guinea pigs (Sly et al., 2012). More recently there have been suggestions that neurotrophins may have a therapeutic role in the treatment of hidden hearing loss (Cunningham & Tucci, 2015; Sly et al., 2016). For these reasons, BDNF was the active drug delivered via the RWM microcatheter in these experiments. Here we examined whether the better-than-normal hearing elicited by neurotrophins (Sly et al., 2012) persisted after cessation of the treatment. This is of interest because although neurotrophins reduce *electrically* evoked ABR thresholds for the duration of drug delivery some studies have shown that its effect is transient, lasting only as long as the drug is administered (Gillespie et al., 2003; Landry, Wise, Fallon, & Shepherd, 2011; Shepherd, Coco, Epp, & Crook, 2005), while others have shown persistent effects long after the neurotrophins delivery has ceased (Ramekers, Versnel, Strahl, Klis, & Grolman, 2015). The reason(s) for these disparate study outcomes are not known, and may be informed by knowing the persistence of neurotrophins' effects on the hearing cochlea.

3.4 Materials and methods

Ethics approval for the described experiment was obtained from the Animal Research Ethics Committee of the Royal Victorian Eye and Ear Hospital (project 12/240AR).

3.4.1 Experimental design and timeline

The primary aim of these experiments was to examine the safety of prolonged RWM drug-delivery techniques using a combination of electophysiological measures, non-destructive imaging and more established imaging techniques. To test this, normal-hearing adult guinea pigs were implanted with a RWM catheter that delivered artificial perilymph (AP) for 1 month. Hearing was assessed by recording auditory brainstem response (ABR) thresholds and distortion product otoacoustic emissions (DPOAEs) over a four month period (the day prior to implantation surgery, then at 2, 4, 5, 7, 10, 13 and 16 weeks after surgery). To control for the physical presence of the RWM catheter, in one of the experimental groups the microcatheter (cannula) was placed but no fluid was delivered – this was termed the "dry" cannula.

After the completion of the last physiological experiment the animals were euthanised with an overdose of pentobarbitone, and the cochleae were harvested. LASER scanning confocal microscopy was used to assess the organ of Corti, and optical coherence tomography to examine the RWM and Reissner's membrane.

This experimental setting also provided the opportunity to conduct new studies on the effects of neurotrophins on hearing when delivered to the round window. We included one experimental group where BDNF was applied to the RWM via the cannula for 1 month. We predicted that ABR thresholds would be better (lower) after neurotrophin treatment compared with AP treatment, as we had observed previously in Sly, et al (2012) (Sly et al., 2012). The question of interest in this arm of the study was the persistence of any hearing improvement (which was tracked for another 3 months after the completion of drug delivery), as this had not been studied previously in the hearing animal.

3.4.2 Mini-osmotic pump surgery

Guinea pigs were anaesthetised as previously described in *Guinea Pig Anaesthesia* 2.1.1. Mini-osmotic pumps and catheters were prepared as described in *Pump Surgery* 2.1.4 above.

3.4.3 Mini-osmotic pump removal

Guinea pigs were anaesthetised as described above. The delivery pump and catheter were inspected and then removed as discussed in *Pump Removal* 2.1.5 above.

3.4.4 ABR Measurements

The equipment and general methods utilised are described in *ABR Measurements* 2.1.2.

Acoustic stimuli consisted of clicks (rarefaction, 100μs width) and tone pips (5 ms total duration including 3 ms plateau plus rise/fall times of 1 ms), with the tone pips presented at frequencies of 2, 4, 8, 16, 24 and 32kHz in the left ear, but only 8, 16 and 24kHz in the right, non-operative ear to reduce the duration of testing and thus, anaesthesia. ABR threshold was defined as the lowest stimulus intensity that produced a response where the amplitude of wave III was greater than 0.4 μV (Figure 3-2).

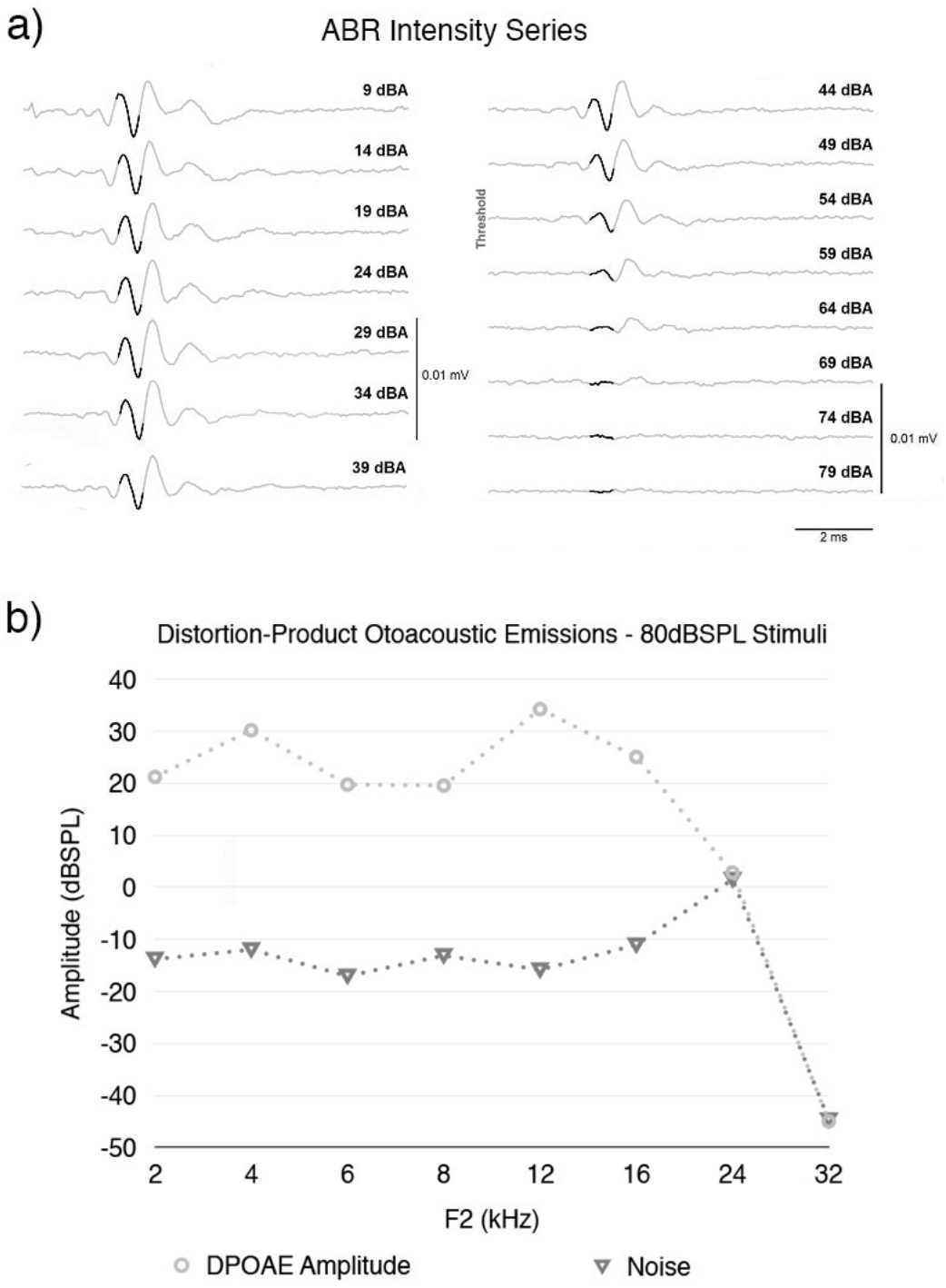

Figure 3-2 - a) Preoperative ABR for one animal, with ABR stimulus intensity measured in dBA from a system maximum of 99 dB SPL and threshold selected by Wave 3 amplitude of 0.4µV. b) Example of DPOAE amplitude and noise floor with F2 intensity of 80 dB SPL in an example animal

3.4.5 Distortion product otoacoustic emissions

DPOAEs were recorded immediately after the ABRs under the same anaesthetic. Stimuli were generated by Intelligent Hearing Systems OAE Suite (IHS, Miami, USA) and delivered by high frequency transducers (IHS, Miami, USA) via an Etymotic 10B+ probe (Etymotic Research, Elk Grove Village, USA) to the left and right ears in turn. A silicon probe tip (IHS, Miami, USA) was fitted to the probe to form a closed field system when properly inserted into the guinea pigs' external auditory meatus. The system was calibrated for the external auditory canal of the guinea pig using a custom made 50 µL cavity.

Two pure tones were presented to generate a distortion product. The F2/F1 ratio was 1.3. The intensity of the delivered pure tones was equal in each run. F2 stimuli were delivered at 2, 4, 6, 8, 12, 16, 24 and 32 kHz (Figure 3-2). Intensities utilised were 50, 60, 70 and 80 dB SPL. Multiple recordings were averaged to reduce the noise floor, with the averaged response intensity and noise floor recorded for each run (Figure 3-2).

3.4.6 Tissue processing

After the final ABR recording, animals were euthanised under general anaesthesia and specimens prepared as described in *Specimen Preparation for OCT* 2.2.3.

3.4.7 Optical coherence tomography

Optical coherence tomography (OCT) was performed to allow measurement of RWM thickness, as well as facilitate non-destructive identification of endolymphatic hydrops. OCT for cross-sectional (X-Z Axes) imaging of biological specimens was developed by Huang et al., (1991) and is now commonplace, particularly in imaging of the eye. Refinements such as frequency-domain techniques have allowed considerable increase in scanning speed as well as the possibility of volumetric acquisitions.

OCT acquisitions were performed using a Spectral-Domain OCT (Spectralis OCT; Heidelberg Engineering, Germany) retinal imager adapted for cochlear imaging using an additional +78-diopter (D) double-aspheric lens.

The decalcified cochleae were mounted in front of the +78D double-aspheric lens with the modiolus oriented vertically. One acquisition was performed in a mid-modiolar plane adjacent to the promontory (Figure 3-3 a), and then the specimen was rotated such that the imaging plane bisected the RWM (Figure 3-3 b). Localisation and orientation of the OCT imaging plane is facilitated by capture of an infrared reflectance image (Figure 3-3 a and c) with the planned OCT acquisition location, orientation and field-of-view indicated by a green arrow.

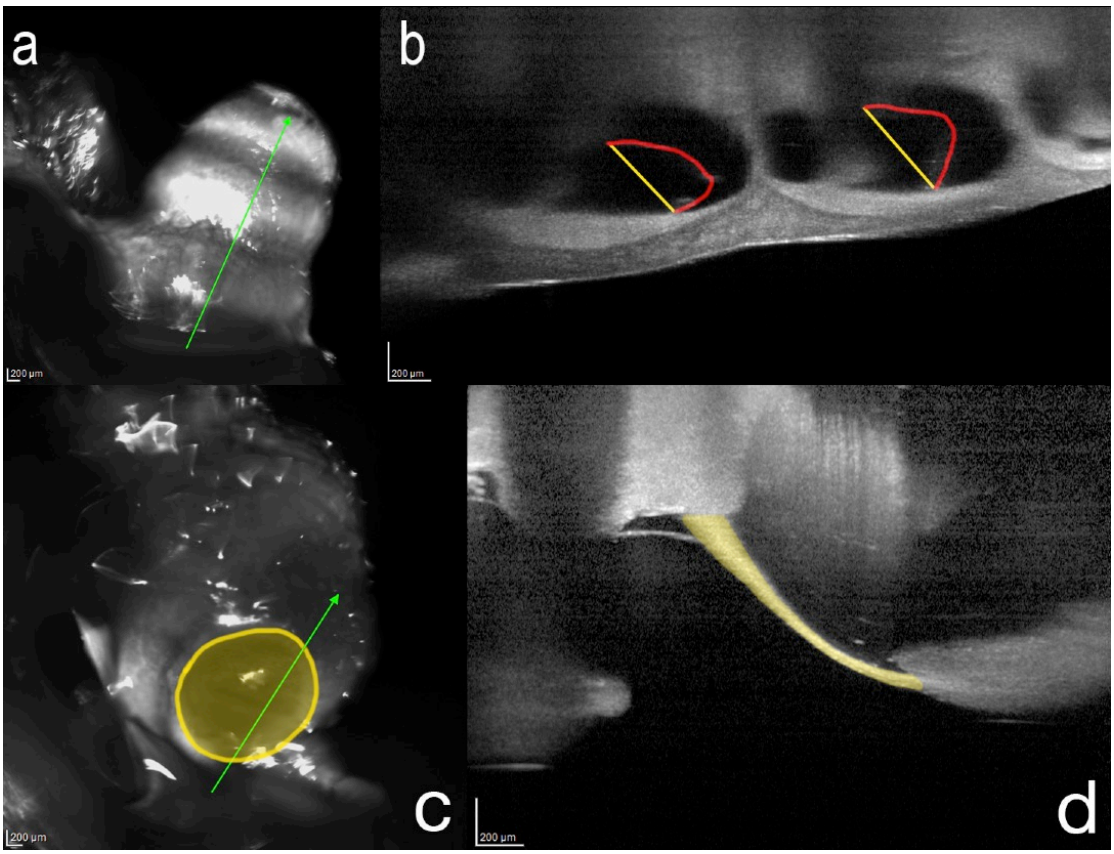

Figure 3-3 - Mid-modiolar OCT acquisition demonstrating the expected (yellow) and actual (red) position of Reissner's membrane (b) in a case of cochlear hydrops. OCT acquisition across the round window membrane highlighted in yellow on IR reflectance (c) and OCT(d)

Measurements of the thickness of the RWM were performed using the two-dimensional distance-measuring tool within Heidelberg Eye Explorer (HEYEX – Heidelberg Engineering, Heidelberg, Germany). Measurements were performed through the centre of the RWM as identified on the Spectralis OCT's infrared reflectance image. Measurements were performed at five points around the centre of the membrane and a mean thickness determined for each specimen. Attempts were made to cut and mount the specimens identically with respect to the Spectralis-OCT in order to ensure that the RWM was positioned identically with regards to the imaging plane. Ideal positioning for measurements of thickness of the RWM would see the specimen mounted with the long axis of the

RWM mounted perpendicular to the beamline, so that measurements of thickness would be performed in the vertical meridian accuracy is maximised. Anatomical constraints meant that an oblique, but consistent position had to be accepted, which would allow between-animal comparisons of RWM thickness. Determination of the position of Reissner's membrane was performed on a transmodiolar section through the promontory, as identified on the Spectralis OCT's infrared reflectance image.

3.4.8 Hair cell counts

The already decalcified tissue was dissected into half-turns. The lateral wall, modiolar remnant and tectorial membrane were excised and then the resulting ~11 pieces photographed on a light microscope.

Using a plug-in (http:// www.masseyeandear.org/research/ent/eaton-peabody/epl-histology-resources/) for ImageJ (NIH, Maryland, USA) developed by Charles Liberman's group at the Massachusetts Eye and Ear Infirmary, distances along the cochlear spiral for each piece of tissue were calculated and a guinea pig specific (Tsuji & Liberman, 1997) frequency-place map generated for the dissected tissue.

The organ of Corti corresponding to the 16 kHz region of the frequency-place map was isolated and stained to demonstrate the presence of inner hair cells using DAPI as a nuclear marker and myosin VIIa as a marker of the presence of sterocilia (Figure 3-4), for all groups except the Dry Cannula.

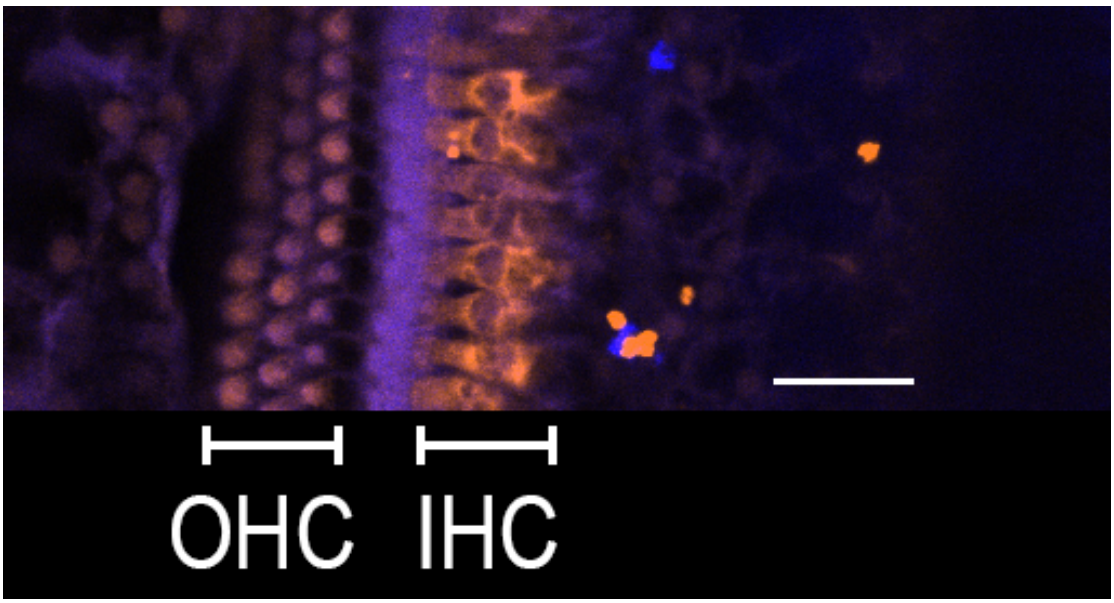

Figure 3-4 - LASER Scanning Confocal Microscopy image of the organ of Corti, demonstrating DAPI (violet) and Myosin VIIa (orange) immunofluorescence of inner and outer hair cells. Scale bar 25µm.

Half-turn whole-mounts were washed in 0.01 M PBS and then preincubated at room temperature for 1 hour in blocking solution of 4% normal horse Serum (Life Technologies, Carlsbad, CA) in 0.01 M PBS with 0.1% Triton X-100 (Sigma-Aldrich, St Louis, MO). Specimens were then incubated overnight at 37 ˚C in a solution of Rabbit anti-Myosin VIIa (Proteus #25-6790) primary antibody at 1:50 dilution before being washed three times for five minutes in 0.01 M PBS. Biotinylated Horse Anti-Rabbit IgG (Vector #6101) was added at 1:200 dilution for one hour at room temperature and then the specimen was washed again in 0.01 M PBS. Alexa Fluor® 568-conjugated streptavidin (Life Technologies, Carlsbad, CA) was used for detection, with the specimen placed in a 1:1000 dilution for one hour at room temperature. After three further washes in 0.01 M PBS, 4',6-diamidino-2-phenylindole (DAPI) was added at 1:10 dilution for 10 minutes for nuclear detection. Three further washes were performed before the specimens were mounted in glycerol.

LASER-Scanning Confocal Microscopy (LSCM) acquisitions were performed on a Nikon A1R confocal microscope, using the DAPI, tetramethylrhodamine isothiocyanate (TRITC) and AF568 LASER lines. A Nikon CFI Plan Apochromatic 20x objective was utilised, with no digital zoom. Z-stacks were acquired to ensure imaging of the full depth of the organ of Corti.

LSCM acquisitions were imported into NIS Elements Viewer (Nikon, Tokyo, Japan). A region of interest of 30 rows of hair cells in each piece of cochlear tissue was used for the counts. This region of interest was randomly determined to begin at the left or right border of the LSCM stack, unless a contiguous sample could not be made at one border due to the presence of processing artefacts, where counting defaulted to the intact side. Inner and outer hair cells locations were examined for DAPI and/or MyosinVIIa fluorescence, and their status recorded as present or absent for each marker.

3.4.9 Statistics

Statistical analyses were performed using XLSTAT (Addinsoft, France), with Mixed-Models ANOVA utilised to examine the homogeneity of data across multiple domains at single time points and Repeated-Measures ANOVA utilised to detect treatment effects across multiple time points. Once identified, differences were further examined using Student's t-tests for paired or unpaired data as appropriate.

3.5 Results

Twenty Dunkin Hartley tri-coloured guinea pigs (11 females and 9 males, ranging from 429-1037 g) were allocated to AP (n = 6), BDNF (n = 9) or 'Dry Cannula' (n = 5) groups.

3.5.1 Electrophysiology

Preoperative ABR thresholds were similar across all groups (AP, Dry cannula and BDNF), which means that the pre-investigational hearing status of the groups did not differ between the experimental conditions ($F_{2,151}$) = 0.711, p = 0.493; Figure 3-5). ABR thresholds were monitored for 16 weeks after surgery (Figure 6). Postoperative time had a significant effect on these ABR thresholds (F = 18.694, p <0.001) and there was a significant interaction between time and group (F = 5.314, p <0.001). This meant that the way in which hearing changed over time differed between the experimental groups, as will now be described. Animals in the Dry Cannula group maintained their ABR thresholds over the first month after surgery, as did animals that had received BDNF over this period (mean difference between AP and BDNF = 6.20 dB, *p (t-test, unpaired)* = 0.068). Over the first month thresholds in the AP group dropped an average of 18.1 dB across all frequencies, which was significantly greater than the shift seen in the BDNF (6.2dB shift, mean difference between AP and BDNF = 11.9 dB, *p (t-test, unpaired)* < 0.001) and Dry Cannula (0dB shift, mean difference between AP and Dry Cannula = 18.1 dB, *p (t-test, unpaired)* < 0.001) groups over the same time period.

BDNF treated animals had a further statistically significant deterioration in their ABR thresholds between the cessation of drug-delivery and 16 weeks (mean difference = 5.3 dB, $p = 0.006$), while during the same period, the AP animals had no further deterioration of their thresholds (mean difference = 3.4 dB, $p = 0.4$). The BDNF group's thresholds deteriorated largely after the 7 week time point (mean difference 6.5 dB, $p < 0.001$). The Dry Cannula group also had a statistically significant deterioration in ABR thresholds between 4 and 16 weeks (mean difference = 15.7 dB, $p < 0.001$), though most change occurred after the 7 week time point.

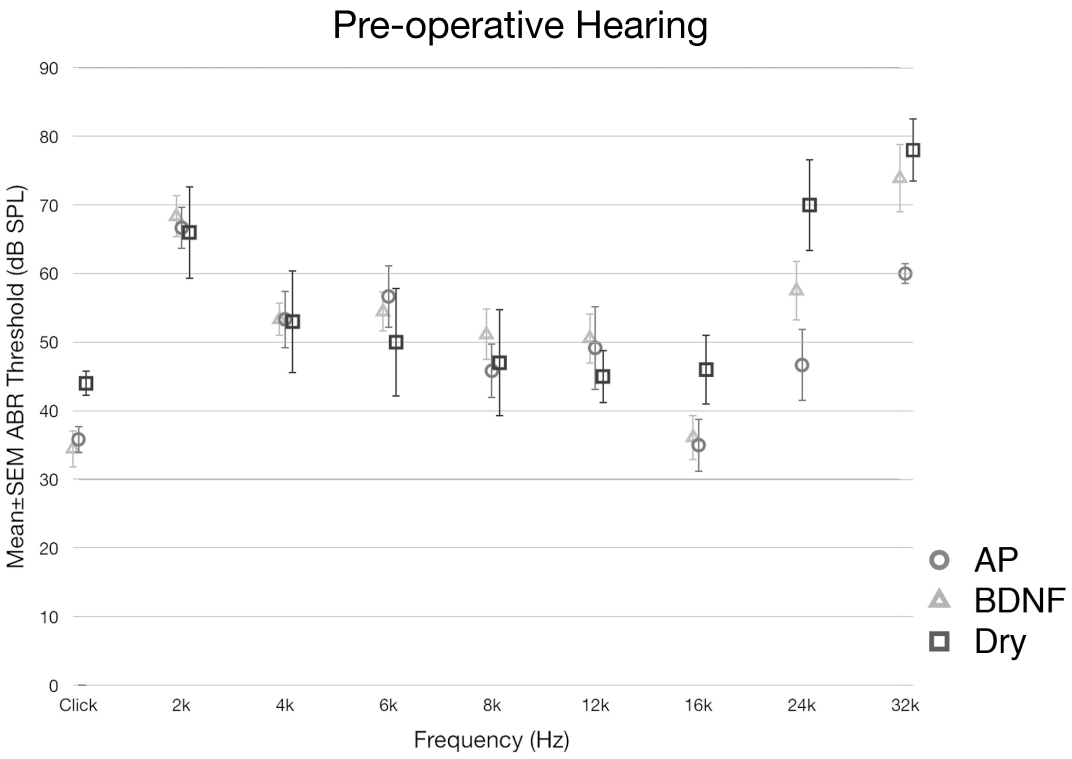

Figure 3-5 - Preoperative ABR thresholds for all animals, represented by the mean and standard error of the mean (SEM) for each experimental group. There was no significant variance by group.

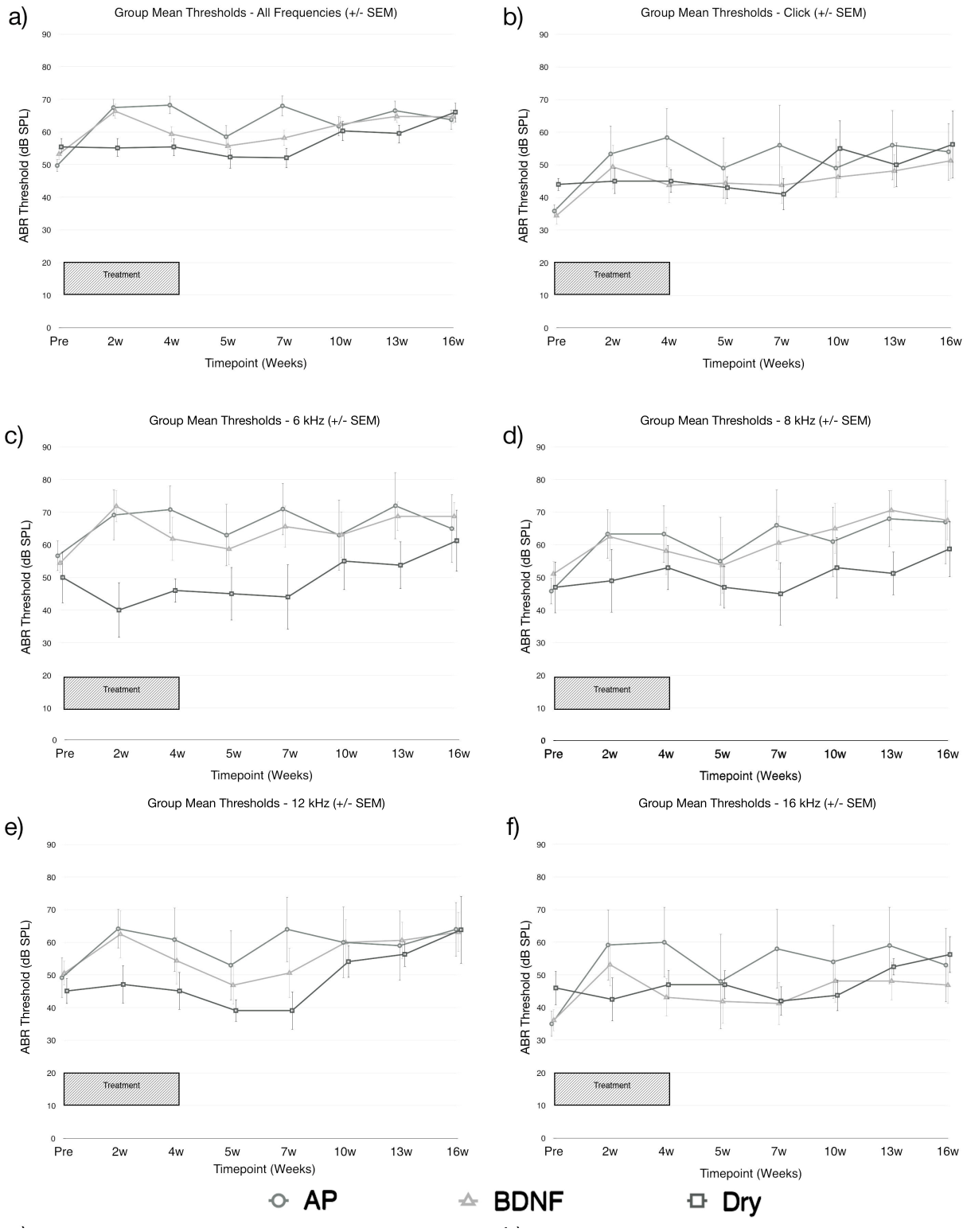

Figure 3-6 - ABR thresholds over time, group means, for a) pooled stimuli, b) clicks, c) 6 kHz and d) 16 kHz tones. Error bars represent standard error of the mean; grey shading indicates the treatment period (weeks 1 to 4). Demonstrates the timeline of deterioration of ABR thresholds. Different time courses become evident in theses plots, but the eventual results are the same

Final hearing results at 16 weeks were statistically homogenous (one way

ANOVA; F = 2.87, p = 0.06), with no significant differences between groups. Specifically, there was statistically significant deterioration in ABR threshold across all frequencies in the BDNF (mean difference = 11.6 dB, p < 0.001), AP (mean difference = 14.7 dB, p < 0.001) and Dry Cannula (mean difference = 15 dB, p < 0.001) groups over the 16 weeks of the experiment (Figure 3-6).

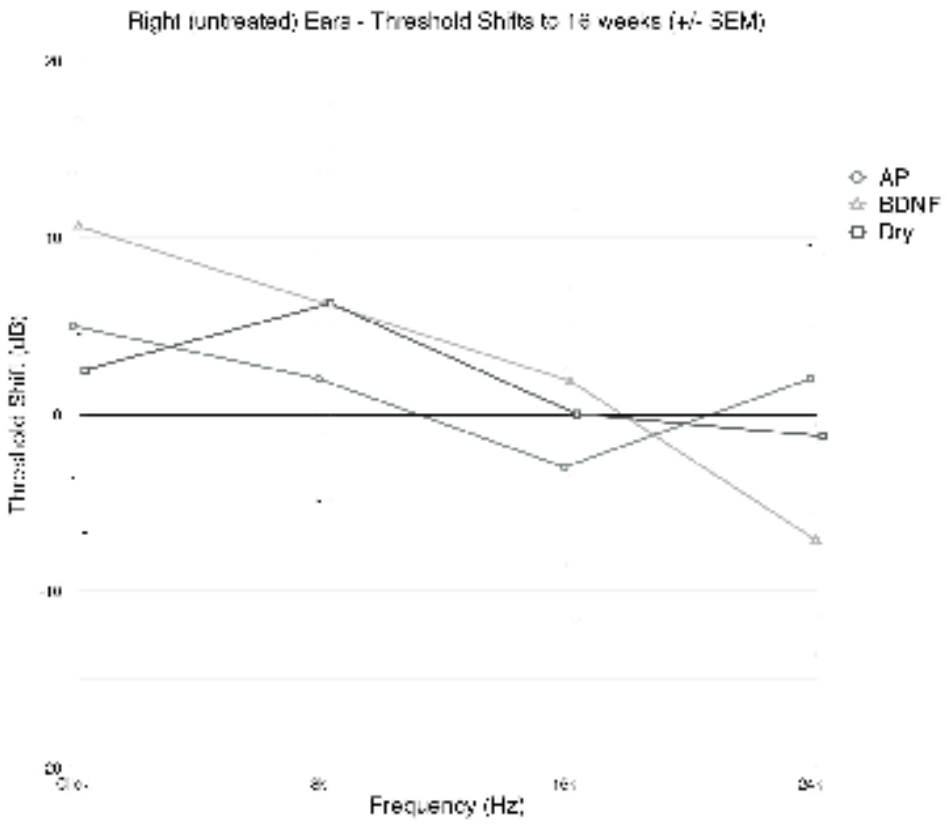

Figure 3-7 - ABR threshold shifts (dB) between preoperative and 16 week measures, from the untreated (right) ear, presented by group. The mean and standard error of the mean are plotted against the stimulus frequency.

Contralateral ABR thresholds were not significantly affected in the Dry Cannula (paired samples t-test, mean difference = -1.9 dB, p = 0.703), BDNF (paired samples t-test, mean difference = -3.2 dB, p = 0.362) and AP (mean difference = -1.5 dB, *p (t-test, paired)* = 0.705) groups (Figure 3-7).

These results demonstrate that the presence of dry cannula had little effect on hearing for the first 7 weeks after surgery, but thereafter there was a deterioration in hearing. Delivery of AP from the cannula lead to a significant reduction in hearing over the month of drug delivery, that persisted over the 16 weeks of the experiment. BDNF delivery via the cannula was associated with a preservation of hearing for 7 weeks after surgery, with a subsequent deterioration in hearing. Hearing was preserved in the contralateral ears of all experimental groups.

3.5.2 Distortion product otoacoustic emissions

DPOAE amplitudes were examined for the two groups where a test solution was delivered (AP and BDNF), in order to assess the effect of the experimental interventions upon outer hair cell function. To ensure that the DPOAE signals exceeded the noise floor, responses to an 80 dB SPL stimulus were analysed at day 0 and weeks 2, 4 and 16 after surgery. These data were analysed by repeated-measures ANOVA with nested effects. The DPOAE amplitudes did not differ between the groups prior to experimentation ($F = 0.120$, $p = 0.730$). After surgery, significant difference between groups were observed across frequency ($F = 59.303$, $p < 0.001$) and within groups ($F = 7.566$, $p < 0.001$). Specifically, an effect of treatment group on amplitude shift was apparent only at week two ($F = 4.368$, $p = 0.039$), where AP animals had already experienced a reduction of amplitude of 7.4 dB ($p = 0.001$), whilst in BDNF animals the DPOAE amplitudes were unchanged from preoperative levels (mean difference = 1.532, $p = 0.350$),

there was, however, no significant difference in mean amplitude (all tested frequencies) between groups at this (p = 0.281), nor any other stage (Figure 3-8).

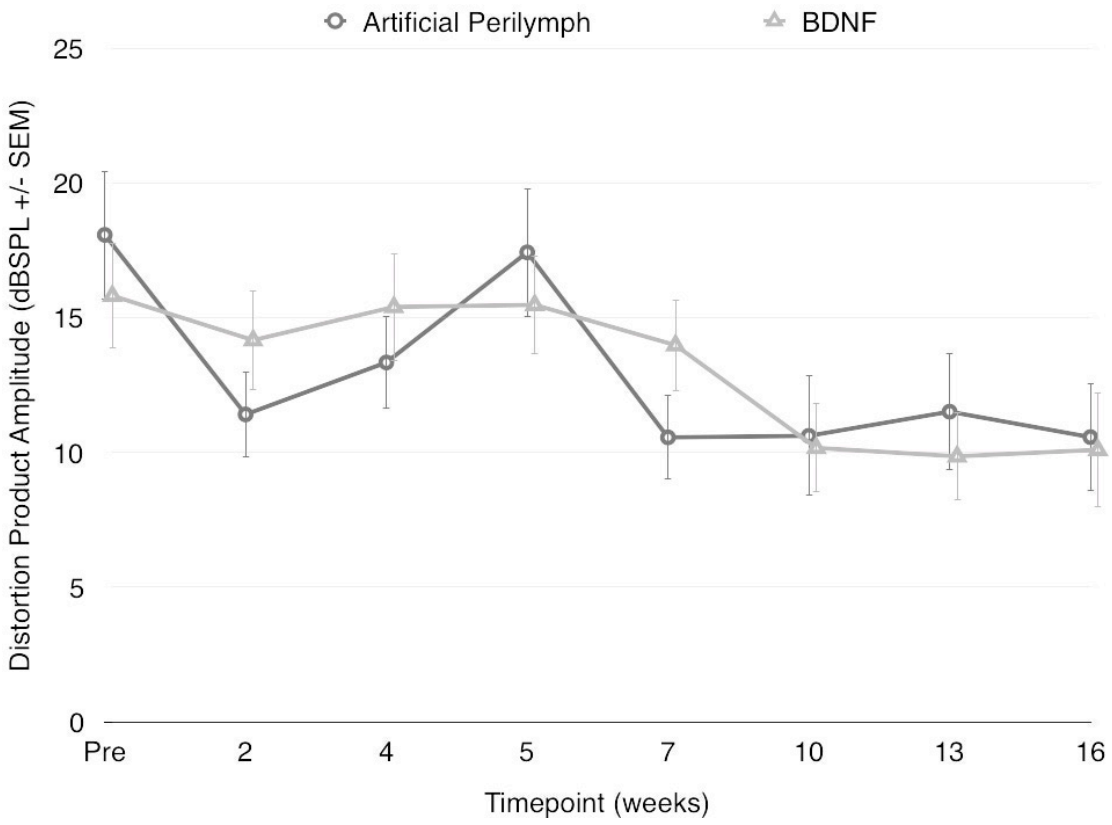

Figure 3-8 - Across-frequencies DPOAE amplitude (mean +/- standard error of the mean dB SPL) plotted by group at all time points. There were no significant differences in mean DPOAE amplitude between groups at any time point. Both groups demonstrated significant degradation of DPAOE amplitudes over the course of the experiment, but the time course of this deterioration differed

DPOAE amplitudes did not differ between groups at four weeks (F = 0.749, p = 0.389). By 16 weeks, both groups had statistically significant reduction in mean DPOAE amplitude across all frequencies (AP mean difference = 4.3, p = 0.040 and BDNF mean difference = 5.6, p = 0.002) when compared to preoperative measures (Figure 3-9).

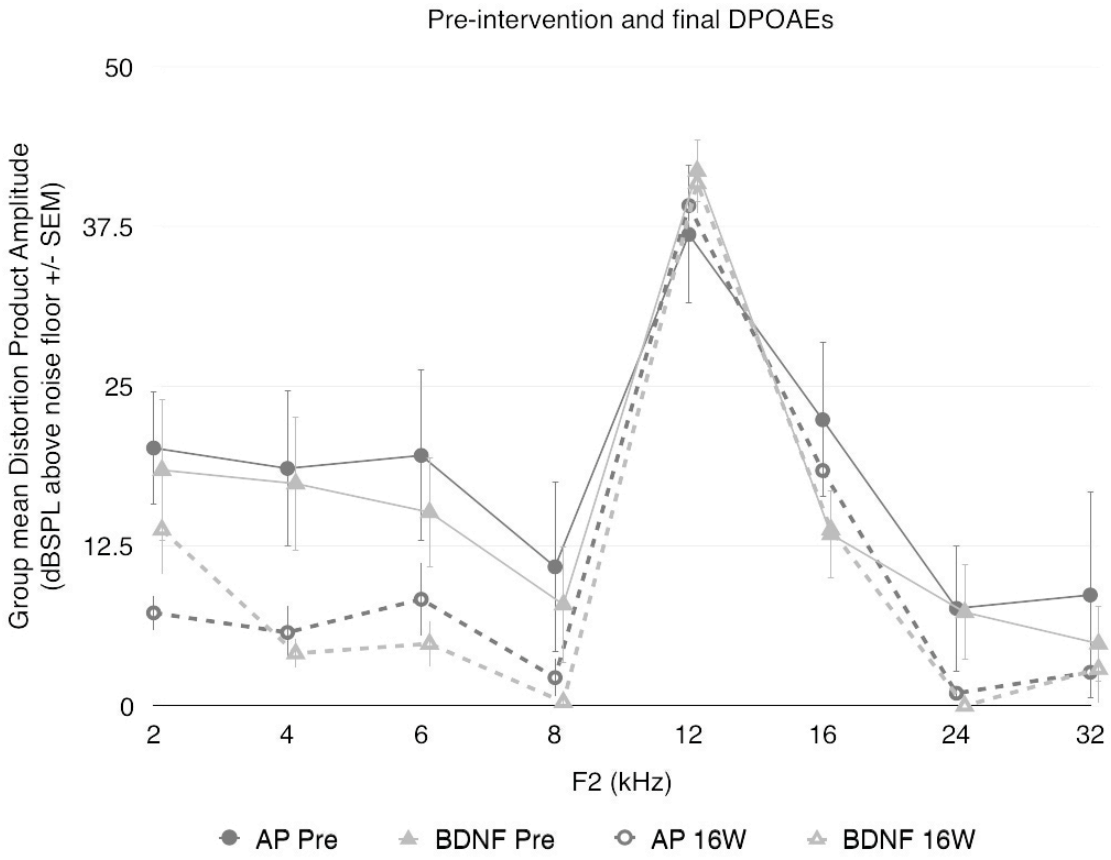

Figure 3-9 - Group mean (+/- standard error of the mean) DPOAE amplitudes by frequency prior to surgery and at 16 weeks, demonstrating the overall deterioration in DPOAEs over the length of the experiment in both the AP and BDNF groups.

3.5.3 Round window membrane

Twenty-four RWMs were intact after tissue processing, compared to 34 at the time of patency testing. The thickness of the central portion of the RWM was measured on OCT acquisitions, with the mean thickness determined from three separate measurements on each sample (Table 3-1). Specimens in which the RWM was not oriented correctly were excluded from analysis of RWM thickness because of concerns about the accuracy of measurements not performed in the vertical meridian.

Table 3-1 - Mean round window membrane thickness (μm) as measured using optical coherence tomography. SD = standard deviation.

Group	Left – treated (μm)	Right – untreated (μm)
Artificial Perilymph	27.8 (n=2, SD 11.55)	60.5 (n=3, SD 33.59)
BDNF	36.0 (n=1, SD N/A)	39.9 (n=4, SD 12.02)
Dry Cannula	43.8 (n=3, SD 7.94)	47.8 (n=3, SD 6.15)

There were no statistically significant differences in mean RWM thickness between groups or sides on unpaired *t*-tests. When comparing the presence or absence of a round window niche cannula (left-treated versus right-untreated), unpaired comparison of all data demonstrated no statistically significant difference ($p = 0.147$). Wetting of the RWM showed a trend toward reduced RWM thickness (mean thickness 30.5 μm for wet RWMs and 47.4 μm for dry or untreated ears), but this did not reach statistical significance ($p = 0.065$).

We found that both the presence of the delivery cannula on the RWM (9 of 17 left-treated RWMs destroyed, versus 1 of 17 right-untreated RWMs, Risk Ratio[2] = 9, 95% Confidence Interval of 5.66 – 14.31) and the delivery of fluid to it (8 of 13 wet RWMs destroyed, versus 2 of 21 dry RWMs, Risk Ratio = 6.46; 95% C.I. 1.61 – 25.85) influenced the likelihood that this structure would withstand tissue-processing. This suggested that the fragility of the RWM has been increased by

[2]Risk Ratio = Probability of event when exposed / Probability of event when not-exposed.

these factors, even if the thinning of the membrane was not found to be statistically significant in those that survived the processing.

3.5.4 Endolymphatic hydrops

The position of Reissner's membrane was determined categorically using OCT, in order to assess its displacement. The authors have previously demonstrated that empirical categorisation of Reissner's membrane on other cross-sectional imaging techniques correlates significantly with cross-sectional area changes in the scala media (Smeds et al., 2015). Reissner's membrane was examined in the second turn of the cochlea on the transmodiolar acquisition and categorised as convex (hydropic), straight (normal), concave ("enhydropic"), or flaccid, where Reissner's membrane was longer than in the normal state, but had mixed curvature.

There was no difference in the likelihood of an abnormal position of Reissner's membrane between ears that had been delivered fluid, and those that had not (unpaired samples t-test, $p = 1.0$). Similarly, there was no statistically significant difference between sides or between the AP treated ears and BDNF treated ears. The frequency of a hydropic Reissner's membrane was not altered by the presence (2 of 17 ears) or absence (3 of 17 ears) of a cannula, fluid delivery overall (0 of 13 ears), or delivery of BDNF (0 of 8 ears) or AP (0 of 5 ears) individually.

3.5.5 Hair cell counts

Administration of BDNF or AP was not associated with a statistically significant reduction in inner hair cells ($DAPI^+$) in either ear (Table 3-2).

. There was no significant reduction in outer hair cell counts in either group or side. The proportion of inner hair cells remaining in each animal was determined and the

mean was calculated for BDNF and AP groups.

Group	**Proportion of Hair Cells Remaining (0-1)**			
	Inner Hair Cells		**Outer Hair Cells**	
	Left	**Right**	**Left**	**Right**
Artificial Perilymph	0.9933	1	0.9888	0.9944
BDNF	0.9904	0.9944	0.9944	0.9955
Dry Cannula	*N/A*	*N/A*	*N/A*	*N/A*

Table 3-2 - Proportion of hair cells remaining (DAPI+) in a 30-row counting window.

3.6 Discussion

3.6.1 All drug-delivery manipulations to the round window caused some hearing loss

The presence of the AP had a detrimental effect upon hearing in its own right, being associated with poorer ABR thresholds whilst it was being delivered than afterwards. Whatever the cause for the hearing loss, its transient nature implies a temporary cochlear change. At least two possibilities for this could be considered. The first is that the constant wetting of the RWM changed its physical and mechanical properties. The second is that the ionic content of the AP had a detrimental effect upon either the round window or the inner ear. Others have reported degradation in hearing from RWM delivery of control solutions (Piu et al., 2011) in the guinea pig, but have not resolved why the hearing loss occurred. In contrast, in a very similar experiment we have reported no hearing loss from RWM delivery of normal saline via a rigid (polyimide) catheter in the guinea pig (Sly et al., 2012). The catheter used in the current study should have been no more traumatic than that used in Sly et al (2012), but the current delivery vehicle was different, being AP rather than normal saline. The simplest explanation for the difference in these experiments is that AP caused the hearing loss and is best avoided for chronic RWM delivery. An alternative explanation could be that the more rigid polyimide tubing used in earlier experiments was less prone to movement within the round window niche.

The presence of a round window niche catheter, even when not delivering liquid, was also seen to be associated with eventual increase in ABR thresholds. The

deterioration seen in these animals, however, was seen later in the experimental timeline, with threshold shift increasing after the 7 week measures. Contralateral ABR thresholds were unaffected in all groups. There is some evidence that the presence of the cannula had a direct physical effect upon the RWM, given that round windows of treated ears were less robust during tissue processing. Whether this altered the function of the RWM or not cannot be gleaned from these data, but if so this could potentially explain all of the observations presented here. For example, if the RWM stiffness were to increase, then this would have a direct effect upon cochlear mechanics, causing degradation of both ABR thresholds and the DPOAE, whilst preserving the hair cells.

It is necessary to consider causes other than an alteration to the round window membrane, for the reduction in auditory function in all groups over the 16 weeks. The degradation in DPOAE thresholds suggests an effect on the organ of Corti or the middle ear, as argued above. The preservation of inner and outer hair cells suggests that if the effect is on the organ of Corti, then the hearing loss results from a loss of function, rather than a reduction in the number of outer hair cells. Examples of such pathology include damage to tip links and stereocilia seen in aminoglycoside ototoxicity (Lenoir & Puel, 1987), noise exposure (H. Wang, Yin, Yu, Huang, & Wang, 2011) and endolymphatic hydrops (Albers, De Groot, Veldman, & Huizing, 1988; Dunnebier et al., 1997; Horner, Guilhaume, & Cazals, 1988; Jia et al., 2012). Endolymphatic hydrops did not feature prominently in these data, as evidenced by the low incidence in all groups on OCT imaging.

Our findings suggest that caution must be exercised when considering the round window as a site for chronic delivery of drugs to the inner ear. The presence of the cannula in itself caused hearing loss, and the presence of AP exacerbated this. Whether similar issues would arise with a hydrogel delivery system is very difficult to ascertain because these systems necessarily cause a conductive hearing loss when present.

3.6.2 BDNF delivery temporarily mitigated hearing loss from round window delivery

As discussed above, there was deterioration in ABR thresholds in treated ears from all groups across the 16 week timeline. As noted in Sly et al (2012) (Sly et al., 2012), BDNF delivery reduced the hearing loss associated with the application of perilymph to the round window niche, but only temporarily. The cause for this was thought to be neural, but whether the effect was mediated by a change in single-fibre threshold, or improved synchrony (Davis, 2016) causing a greater amplitude of the ABR response, is not yet understood. Unlike the results of that study ABR thresholds were not improved beyond baseline during BDNF treatment. The difference between this study and our previous work (Sly et al., 2012) is likely due to the increased hearing loss caused by the particular method of drug delivery in this paper. It is apparent that the major portion of the deterioration in hearing thresholds in the BDNF group did not occur until after the end of BDNF delivery by the mini-osmotic pump, whilst thresholds in the AP group deteriorated at an earlier time point. This suggests that delivery of BDNF protected against the functional deficit associated with chronic AP delivery to

the RWM, but that this protective effect did not persist. ABR thresholds were similar to animals in the AP group by the week 10 measures. The time course of the non-sustained protective effect observed here was similar to that seen by Gillespie and colleagues(Gillespie et al., 2003), where BDNF treatment after deafening initially preserved spiral ganglion neurons, but spiral ganglion neuron density dropped precipitously after cessation of BDNF delivery to levels similar to untreated (deafened) animals. However, this study was in contrast with the later findings of Ramekers and colleagues (Ramekers et al., 2015) , where beneficial effects of BDNF treatment were seen to persist for at least 8 weeks after treatment cessation.

Most of the previous literature concerning the effects of BDNF within the cochlea has been on deafened cochleae. Within this literature there is an unresolved discrepancy surrounding the duration of effect of exogenously applied BDNF. Some studies (Gillespie et al., 2003) show a transient preservation of spiral ganglion cell neurons and electrically evoked neural function that persists for just a few weeks after BDNF treatment. Other studies (Agterberg, Versnel, van Dijk, de Groot, & Klis, 2009; Ramekers et al., 2015) have demonstrated persistence of spiral ganglion cell survival and functional benefit that persists after cessation of BDNF treatment. The reason(s) for this discrepancy are not yet resolved. While it has been suggested that the electrical stimulation used to measure electrically evoked ABRs may have been sufficient to provide prolonged trophic support in most of these studies, this explanation cannot account for Rameker's results where it was suggested that exogenous BDNF may induce an autocrine neurotrophic loop that sustained the spiral ganglion cells after BDNF

treatment had stopped (Ramekers et al., 2015). It is important to note that in all of these studies, there was significant loss of hair cells and secondary degeneration of the spiral ganglion induced by ototoxicity, and that BDNF's effects could be attributed to improved neural survival (and therefore function). The present study differs considerably from the previous literature in that there was significant residual hearing at the end of the experiment, meaning that the organ of Corti was largely intact, and considerably less damaged than in the ototoxically deafened cochlea. Therefore, any effect of BDNF on neural function would have been primarily upon the function of auditory neurons, rather than their survival, and we propose that this may explain why we saw a transient effect of BDNF in the present study.

The results presented here suggest that although the presence of the cannula, and in particular the application of AP to the round window was detrimental to hearing, the functional deficit could be temporarily allayed with BDNF by a direct neurotrophic effect upon the auditory nerve. A neural site of action is consistent with most of our results, and in particular that at the end of the observation period (well after withdrawal of the neurotrophins) the DPOAE thresholds and hair cell counts did not differ between the groups, suggesting that the extent of the cochlear pathology from the presence of the cannula and the delivery of test solutions did not differ.

3.7 Conclusions

The presence of a microcatheter adjacent to the RWM was detrimental to hearing, particularly when delivering AP. In this respect, the current paper did not replicate the findings of Sly and colleagues (Sly et al., 2012), where normal saline applied to the round window caused minimal hearing loss. A combination of imaging techniques was utilised to attempt to identify the site and mechanism of the resulting loss. Secondary cochlear endolymphatic hydrops was able to be excluded through the use of a novel non-destructive imaging technique: Optical Coherence Tomography (OCT). Furthermore, the application of LASER-scanning confocal microscopy to the organ of Corti allowed us to determine that the population of nucleated hair cells did not change. The most likely explanation for the degradation in hearing was either a change in the mechanical properties of the round window, or alternatively a reduction in function of the hair cells. The transient effect on hearing of the AP favours an effect on the round window. We suggest that further evaluation of the local effects on RWM structure and function of round window niche microcatheters and treatments involving continuous 'wetting' of the RWM is required before these techniques can be safely applied, particularly in populations with normal or near normal pre-treatment hearing. Our treated ears demonstrated a trend toward thinning of the RWM on OCT, but these results were hampered by the failure of treated membranes to withstand the chosen decalcification process.

We learn from this study that the benefit to acoustic hearing from the application of BDNF to the round window is temporary, lasting for a matter of weeks after cessation of neurotrophin treatment.

3.8 Acknowledgements

The authors would like to thank Michelle Stirling (animal husbandry), Scott Chambers and Leon Winata (technical assistance), Prue Nielsen (histological processing) and James Fallon (Igor software routine development) for their assistance. This work was funded by the Garnett Passe and Rodney Williams Memorial Foundation, Melbourne, Australia.

4 Experiment 2 – Evaluating Endolymphatic Hydrops and Tissue-Response after Cochlear Implantation using µCT

4.1 Experimental Overview and Timeline

Endolymphatic hydrops is a proposed mechanism of deterioration of residual hearing after cochlear implantation. Guinea pigs will undergo unilateral cochlear implantation with a silastic dummy electrode. Animals will be sacrificed and perfused at time points of one day, one week, one month and three months after implantation and undergo imaging using Micro-CT. Measures of Reissner's membrane position, electrode position, inflammatory response will be performed along the length of the organ of corti and correlation with hearing measures determined.

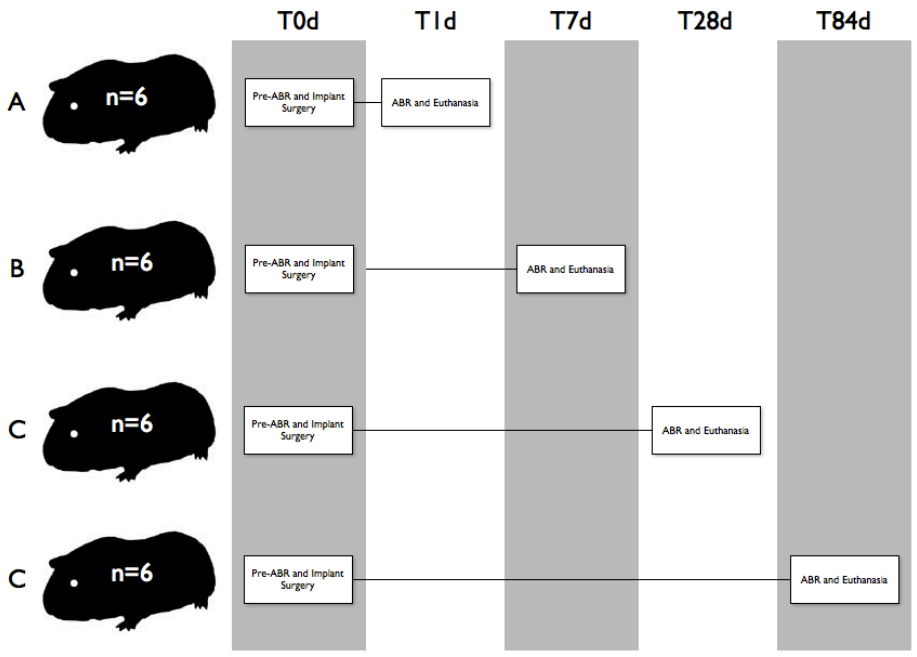

Figure 4-1 - Timeline and grouping for Experiment 2

4.2 Methods

4.2.1 Surgical Procedures

The animals were prepared and surgery performed as described in 2.1.3 *Cochlear Implantation*.

4.2.2 Specimen Preparation for µCT

After the final electrophysiological recording, animals were euthanased under general anaesthesia as previously described. Specimens were then harvested as described in 2.2.1 *Specimen Preparation for µCT*

4.2.3 µCT Acquisition

The specimens were imaged using an XRadia MicroXCT-200 scanner (XRadia, Concord, CA) as further described in 2.3.2 *µCT Acquisition*.

4.2.4 µCT Analysis Procedures

Analysis of µCT data was performed primarily in Amira (versions 5 through 5.6; Visualization Sciences Group, Bordeaux, France) on an Apple Mac Pro (Apple Computer, Cupertino, USA) desktop computer with the Mac OS X 10.8.4 Operating System. Simpler computational tasks were often delegated to a Dell Precision T3600 (Dell, Round Rock, TX) desktop computer running the Windows 7 SP1 Operating System(Microsoft, Redmond, USA).

8-bit grey-value data was imported from the stack of slices generated by XReconstructor, with the dimensions of the voxels to be imported into Amira provided by the metadata inspector within XReconstructor.

Micro-CT voxels are usually isotropic, and in our case each side measured 5.2µm as previously described (see µCT Acquisition).

Non Local Means (NLM) Noise-Reduction (see also (James et al., 2008)) was performed upon all imported µCT datasets. Two-dimensional NLM filtering was performed, with a search window of 30 voxels, a local neighbourhood of 6 voxels and a similarity value of 0.5. Amira was allowed to calculate the block size appropriate to the amount of Video Random Access Memory (VRAM) on-board the CUDA (Nvidia, Santa Clara, CA) General-Purpose Graphics Processing Unit (GPGPU) device allocated to the task.

4.2.4.1 Tonotopic Mapping

Tonotopic mapping relies on accurate measurement of the length of the organ of corti for each individual animal. A Bezier spline was constructed from points placed approximating the cuticular plate of the inner hair cells along the length of the Organ of Corti from the hook region to the helicotrema. 99 points were generally used to define this spline, with the interval between points tailored to the changing radius of curvature along the length of the cochlear spiral. A shorter interval between points was used apically because of the shorter radius of curvature. Once this spline had been defined, it was converted to a lineset defined by 300 equally spaced points. Frequency-place maps of the mammalian

cochlea according to Greenwood (Greenwood, 1990) and Wada (Wada, Sugawara, Kobayashi, Hozawa, & Takasaka, 1998) see characteristic frequencies mapped to locations at proportions of the total length of the organ of corti, so division of the organ of corti spline into equally spaced points means that a given point along the organ of corti spline will represent a particular frequency despite variation in total length of the Organ of Corti between animals.

For a 300-point lineset along the Organ of Corti, the commonly tested frequencies will be located at approximately the points listed below.

Table 4-1 - Characteristic Frequency locations along a 300-point Organ of Corti lineset.

Frequency (Hz)	**PointID**
32000	19
24000	36
16000	59
8000	99
4000	139
2000	179
1000	219

4.2.4.2 Evaluation of Cochlear Hydrops

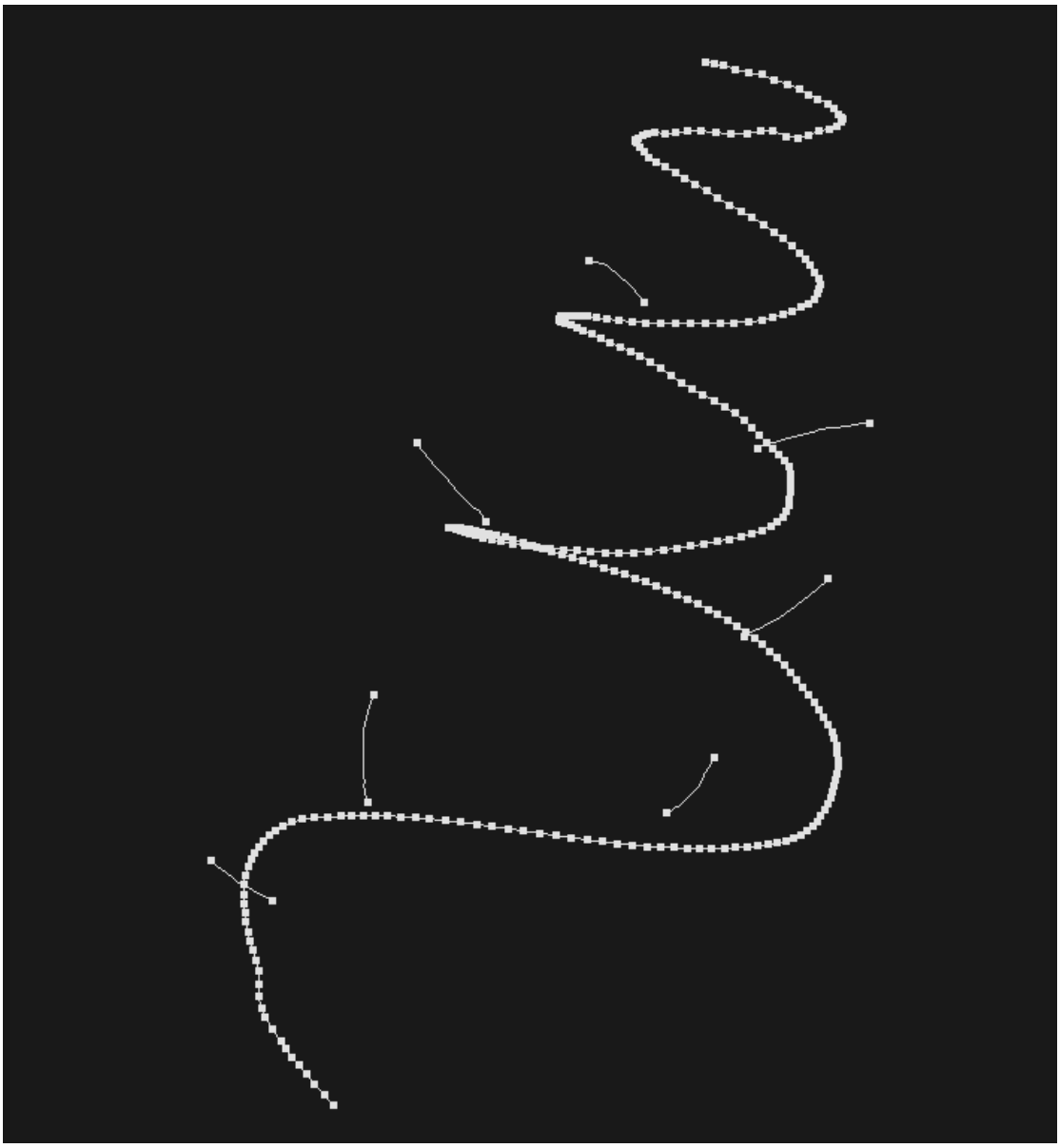

Figure 4-2 – An Organ of Corti linset, displaying 300 constituent points. Reissner's Membrane splines for 1 through 32k are also drawn.

A LineProbe was defined along the modiolar axis of the cochlea, with its origin in the basal plane of the cochlea and its endpoint at the apex of the cochlea. This LineProbe serves as the axis of rotation around which frequency specific transmodiolar slices are generated. Once the organ of Corti spline has been converted to a lineset, the individual points along the lineset are selectable and

can be highlighted, to allow placement of a transmodiolar slice intersecting the highlighted point.

Once this slice has been placed, evaluation of the position of Reissner's membrane in that slice can be performed.

A notable exception is evaluation of Reissner's Membrane at the location of 32kHz hearing in the guinea pig. At this point, the organ of Corti is oriented essentially parallel to the Modiolar Axis. For this location, then, the evaluation of Reissner's Membrane is performed in a plane parallel to the basal plane of the cochlea (Verbist et al., 2010).

For the slice, and thus characteristic frequency in question a new Bezier spline is defined along the contour of Reissner's membrane, beginning at the spiral limbus and ending at the lateral wall of the cochlea.

Qualitative assessment of the shape of Reissner's membrane can be made in the Amira viewer at the time that splines are produced for Reissner's membrane. Quantitative assessment is automated through the use of software developed by Dr Luke Campbell in a Matlab (MathWorks, Natick, MA) environment. Difficulty arises when reducing the often complex shape of Reissner's membrane to a numerical figure useful in statistical comparisons. Several measurements were trialled and abandoned before the final process was developed.

4.2.4.2.1 Length Excess

Length Excess involves tracing the position of Reissner's membrane in the plane of interest (line A~B in Figure 4-3), with Amira returning the length of the created spline in µm. Through a Matlab interface module within Amira, Matlab is then able to calculate the length of the straight line between the start and end points of that spline (line AB in Figure 4-3). A length excess (LE) of Reissner's membrane can then be defined as the difference between these two lengths. This figure was then converted to a proportional LE in terms of the length of AB, to control for variation in Reissner's membrane along the length of the scala media and between animals.

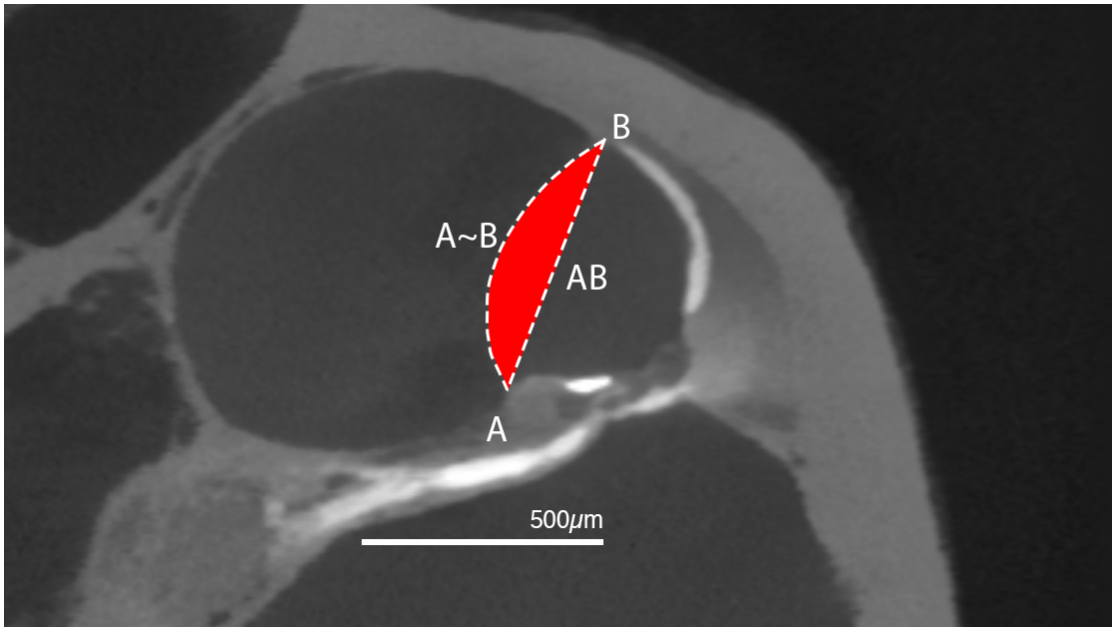

Figure 4-3 - Evaluation of Hydrops. Line AB is assumed to be the ideal position of Reissner's Membrane. Length of A~B is measured, with Length Excess(µm) = A~B – AB.

LE as an indicator of cochlear hydrops falls down when the shape of the hydropic Reissner's membrane is not a simple arc. A flaccid Reissner's membrane with numerous deviations from the ideal may have a significant LE while having no effect on the cross-sectional area of scala media, such as in Figure 4-5 – C.

4.2.4.2.2 Maximal Displacement

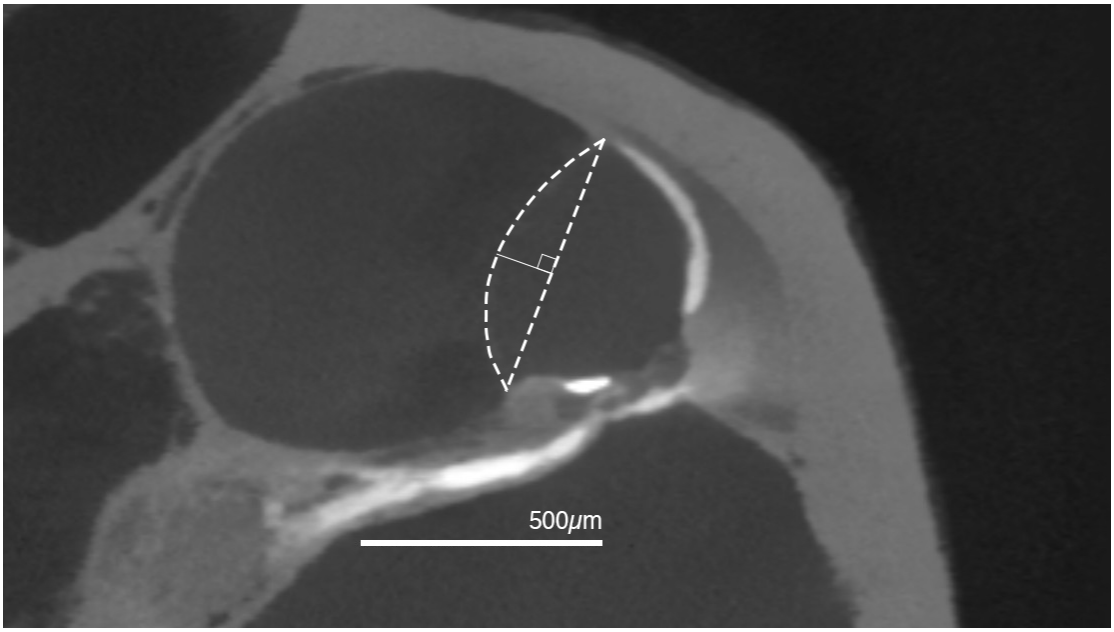

Figure 4-4 - Measuring the maximal displacement of the hydropic Reissner's membrane from the ideal position

When endolymphatic hydrops is present and Reissner's membrane is bowed simply and convex, the maximal displacement of Reissner's membrane from its ideal position can be measured (Figure 4-4) in voxels and then converted to a μm measure. This measure is also applicable in cases where Reissner's membrane is simple in shape, but collapsed, such as in Figure 4-5 – A. This value is signed negatively to indicate the reduction in scala media area at that point.

This measure falls down in instances where Reissner's membrane is not simple in shape, such as example Figure 4-5 where positions B and C may have almost identical maximal displacement of Reissner's membrane despite the former being obviously hydropic and the latter having a scala media cross-sectional area that is similar to what it would be with Reissner's membrane in the anatomical position.

4.2.4.2.3 Summed Displacement

In instances where the contour of Reissner's membrane is more complex, areas above and below the ideal position of Reissner's membrane are signed according to the direction of displacement and then summed. This better describes cases such as Figure 4-5 – C in terms of the sigmoid Reissner's membrane's effect on the cross-sectional area of scala media. The positive and negative displacements of Reissner's membrane give a summed displacement of zero, which parallels the change in the cross-sectional area.

This measure falls down when the shape of Reissner's membrane is such that deflections may be similar in displacement, but different in area.

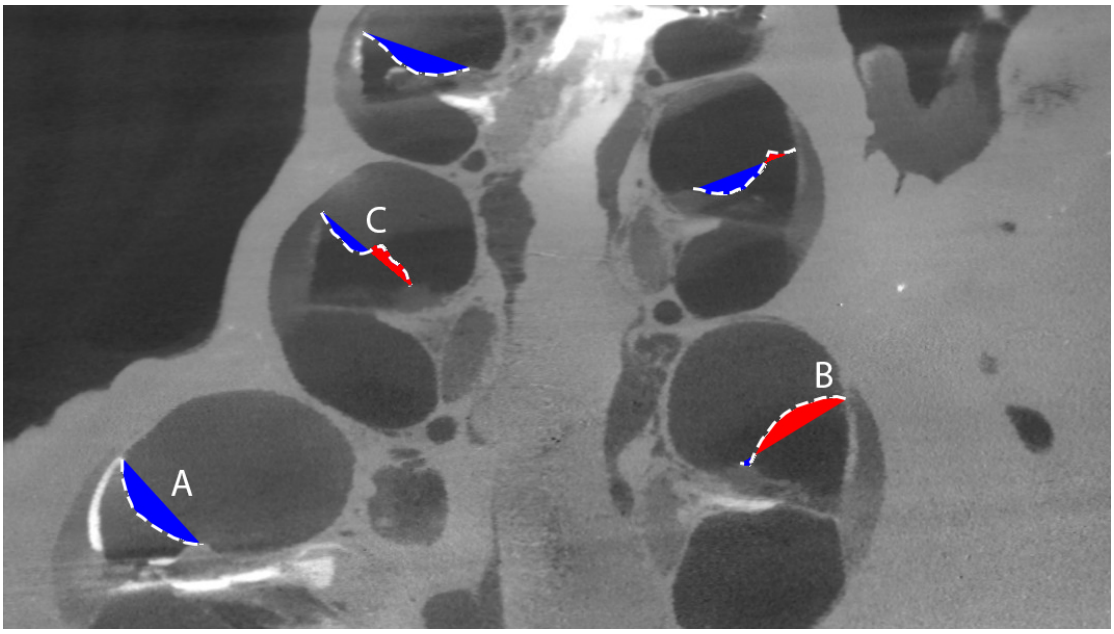

Figure 4-5 - Evaluation of Hydrops when Reissner's membrane has a complex contour. Negative areas are coloured blue, positive areas are coloured red.

4.2.4.2.4 Scala Media Area Difference (SMAD)

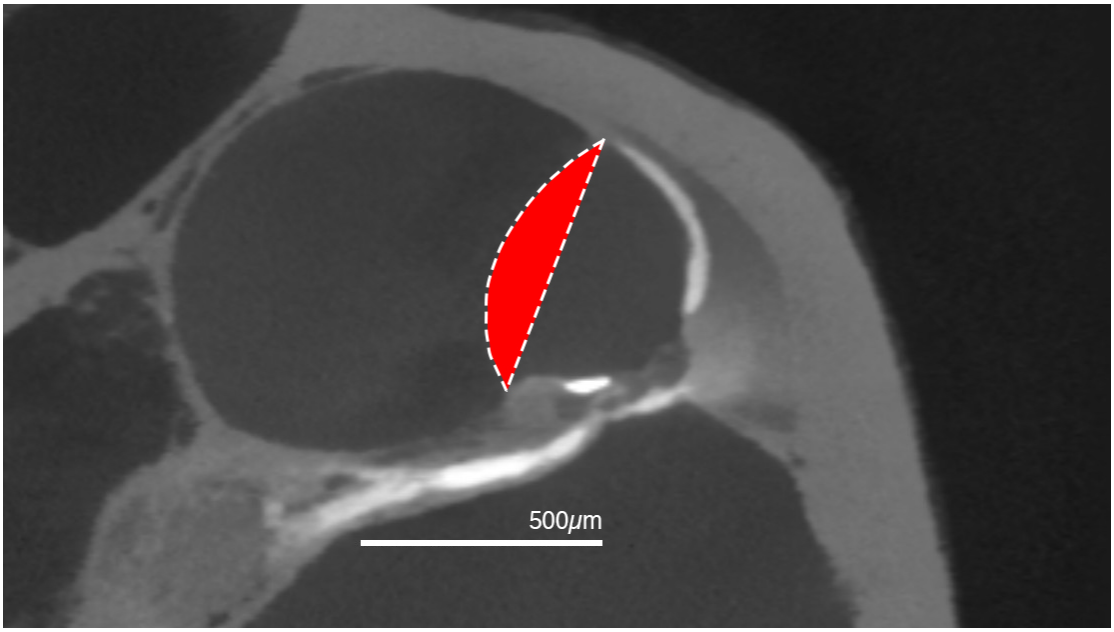

Figure 4-6 - Scala Media Area Difference. The area under the spline traced along Reissner's Membrane is the cross-sectional area increase of Scala Media in this plane

The final measure utilised involved tracing Reissner's membrane in planes of interest using a Bezier Spline (Figure 4-3 – line A~B). The area of the shape resulting when the spline ends were connected by a straight line (Figure 4-3 – line AB) was able to be measured by custom code in Matlab via a Matlab interface module within the Amira environment. This area represents the change in cross-sectional area of scala media in that defined plane. Furthermore, the resulting areas were signed according to their displacement toward or away from a known line (the modiolar axis, defined using a LineProbe) and summed. This approach accounts for sigmoid, or even more complex shapes of Reissner's membrane and their effects on scala media cross-sectional area.

The main deficiency in this technique is that it ignores the huge length excess seen in a complex, flaccid Reissner's membrane. If one can assume that an elongated Reissner's membrane is an indicator of past cross-sectional area

change, then a summed SMAD may be ignoring significant data. Consideration was made of calculating the area under an arc, the length of the flaccid Reissner's Membrane to generate a SMAD that may have been present in the recent past. This, however, ignores the possibility that elongation may have been secondary to a contraction in scala media cross-sectional area, rather than solely due to hydrops. Further future work on the natural history of changes in Reissner's membrane in hydrops may demonstrate that the length excess is of significance.

Calculation of SMAD using this technique was validated with the assistance of Dr Henrik Smeds with respect to qualitative assessment of the position of Reissner's membrane (Smeds et al., 2015). Strong correlation was demonstrated between these qualitative and quantitative methods of evaluation ($r = 0.878$, $p < 0.0005$) of Reissner's membrane displacement.

4.2.4.3 Tissue Response Segmentation

Quantification of tissue response to cochlear implantation and measurement of organ volume relies on the process of 'Segmentation'. Segmentation in this context means the labelling of voxels within a three-dimensional dataset to indicate that they belong to particular material or structure. Once segmentation of relevant materials and structures has been performed, further analysis of these materials can be performed in terms of their radiodensity, volumes, spatial relationships, etc.

Once data had been imported into Amira, segmentation was performed in Amira's Segmentation Editor.

A LabelField was created, which is a three-dimensional matrix with the same dimensions as the original dataset. Each location in this new matrix contains an indicator as to which material this voxel belongs, rather than the grey-value of the voxel as in the original dataset. The materials and structures to be segmented for the evaluation of tissue response and saccular hydrops were the Scala Tympani, Electrode Dummy, Tissue Response, Saccule and Ductus Reuniens.

The plane in which the cross-section of the electrode dummy is most circular was chosen for segmentation of the contents of the basal turn of the cochlea. The outline of the scala tympani was traced using the Lasso tool (settings as per Fig. 20).

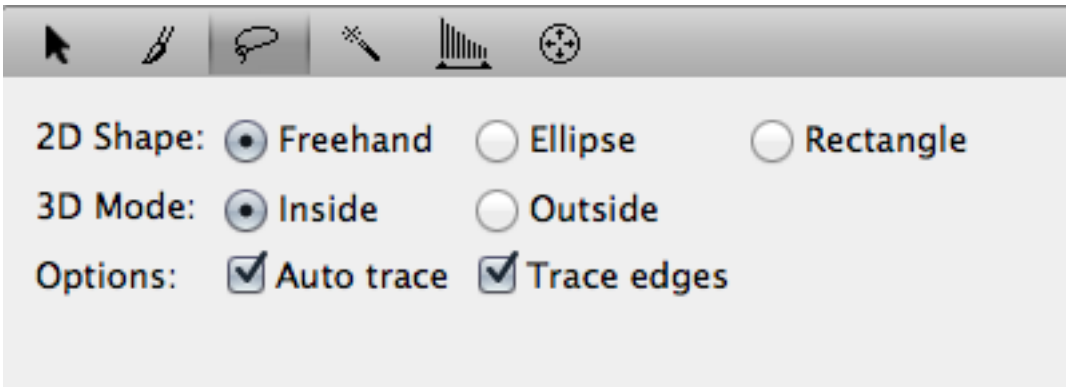

Figure 4-7 - Lasso settings for selecting the scala tympani contour during segmentation

Utilising these settings sees the Lasso tool follow edges of high contrast between manually-placed control points. Larger numbers of control points were required to be placed in areas where edge contrast is low, such as where dense tissue-response abuts otic capsule bone. Because of the large number of image slices that were to be considered to fully segment a structure such as the scala tympani

in the basal turn; interpolation was used to shorten the process. Furthermore, the very gradual change in contour of the scala tympani across slices makes Amira's interpolation process viable for accurate segmentation of the Scala. Generally, every tenth slice would be drawn for interpolation of the contour of scala tympani. Smaller intervals between drawn slices were required when the shape of the scala changes rapidly between slices, such as at the hook region or where turns are seen to unite on the chosen view.

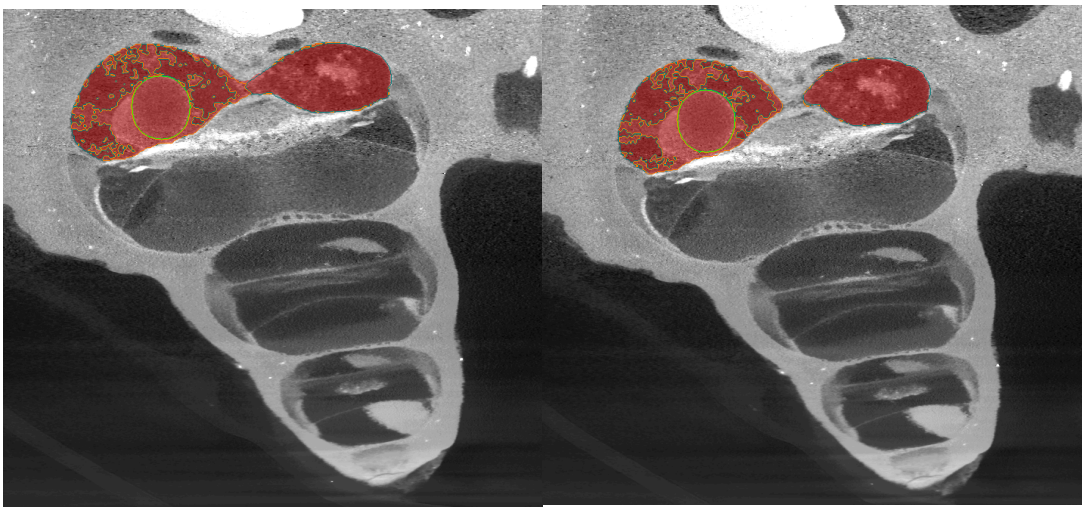

Figure 4-8 – Smaller intervals are used between manually selections in areas where the contour of the Scala changes rapidly across slices, such as the example above where the limbs of the scala are seen to unite.

Once interpolation has been performed between the manual-selections, the selected voxels were added to a material that will be renamed 'Scala Tympani'. Currently this material will not only include the scalar perilymph, but also areas of tissue response and the intrascalar course of the electrode dummy. The next step was to move voxels representing the electrode from the scala tympani material to their own material. A new material was created and renamed 'Electrode', then the shape of the intrascalar portion of the electrode defined

using the circular paintbrush. Again, because the electrode is consistent in its shape along most of its length, interpolation could be utilised to shorten the process of segmentation. Interpolation was generally performed between a manually defined selection every tenth slice, but the interval was necessarily decreased where the electrode changes shape at its tip. Once this selection was interpolated and complete, the voxels were moved from the Scala Tympani material to the Electrode material.

The next step was segmentation of tissue response within the scala. After the electrode voxels have been moved to their own material, the voxels remaining in the Scala Tympani material will consist of:

1. Perilymph
2. Tissue Response, including neoosteogenesis
3. Precipitated Osmium

Selection of tissue response was performed using the Magic Wand tool in Amira. The Magic Wand is based on a combination of voxel thresholding and propagation. A start point was defined in the image, and the 'in' and 'out' values for thresholding defined on the datasets histogram as seen in Figure 4-9. The 'in' value was adjusted to achieve selection of the tissue response without also selecting perilymph. The 'out' values were adjusted to exclude any Osmium

precipitates.

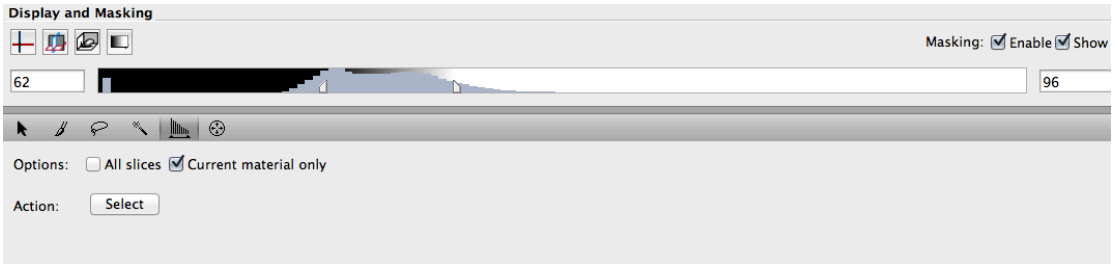

Figure 4-9 - Grey marker tabs on the histogram demonstrate the highest and lowest grey values allowed in the thesholding operation. This same technique is used when a propagating/threshholding technique is used.

By selecting the Scala Tympani material in the Materials List and selecting the 'Current material only' option, the selection made by the Magic Wand tool is limited to the bounds of the Scala Tympani material.

Once all identifiable tissue response has been selected, the selected voxels were added to a new material which is renamed 'Tissue Response'.

A MaterialStatistics module was attached to the LabelField to derive basic information about the materials, such as volume in number of voxels and thus volume in μm^3.

4.2.4.3.1 Tissue Response Rendering Technique

Figure 4-10 demonstrates the results of the rendering technique used to observe the volume, density and location of tissue response after cochlear implantation. The electrode's external surface has been rendered as an opaque surface through the following steps:

1. A SurfaceGen module is connected to the LabelField created by the segmentation process.

2. ‘Electrode’ is selected from the materials list and the surface generated.
3. A SurfaceView module is attached the resulting surface data
4. ‘Selection mode’ is changed to ‘Material’
5. In ‘Materials’, ‘Electrode’ is selected from the first dropdown and ‘All’ selected from the second, telling Amira that a surface is to be generated where the electrode meets any other materials, ie. The electrode’s external surface.
6. A shaded style is selected from ‘Draw style’

Tissue Response has been volume rendered in order to demonstrate the variable radiodensity of the contents of that material.

1. A Volren module was created and connected to both the original dataset (for radiodensity information) and the segmented LabelField (for material allocations).
2. The ‘Tissue Response’ material is selected from the Label dropdown so that only voxels allocated to that material will be rendered.
3. The Standard ‘volrenRed.col’ colourmap was utilised, which is a red-yellow-white colourmap, with a simultaneous reducing transparency gradient.

The points of contact between tissue response and the basilar membrane were visualised as a surface at their intersection.

1. A SurfaceGen module is connected to the LabelField created by the segmentation process.

2. ‘BasilarMembrane’ is selected from the materials list and the surface generated.
3. A SurfaceView module is attached the resulting surface data
4. ‘Selection mode’ is changed to ‘Material’
5. In ‘Materials’, ‘TissueResponse’ is selected from the first dropdown and ‘BasilarMembrane’ selected from the second, telling Amira that a surface is to be generated wherever the Basilar Membrane contacts voxels allocated to the tissue response.å
6. A shaded style is selected from ‘Draw style’

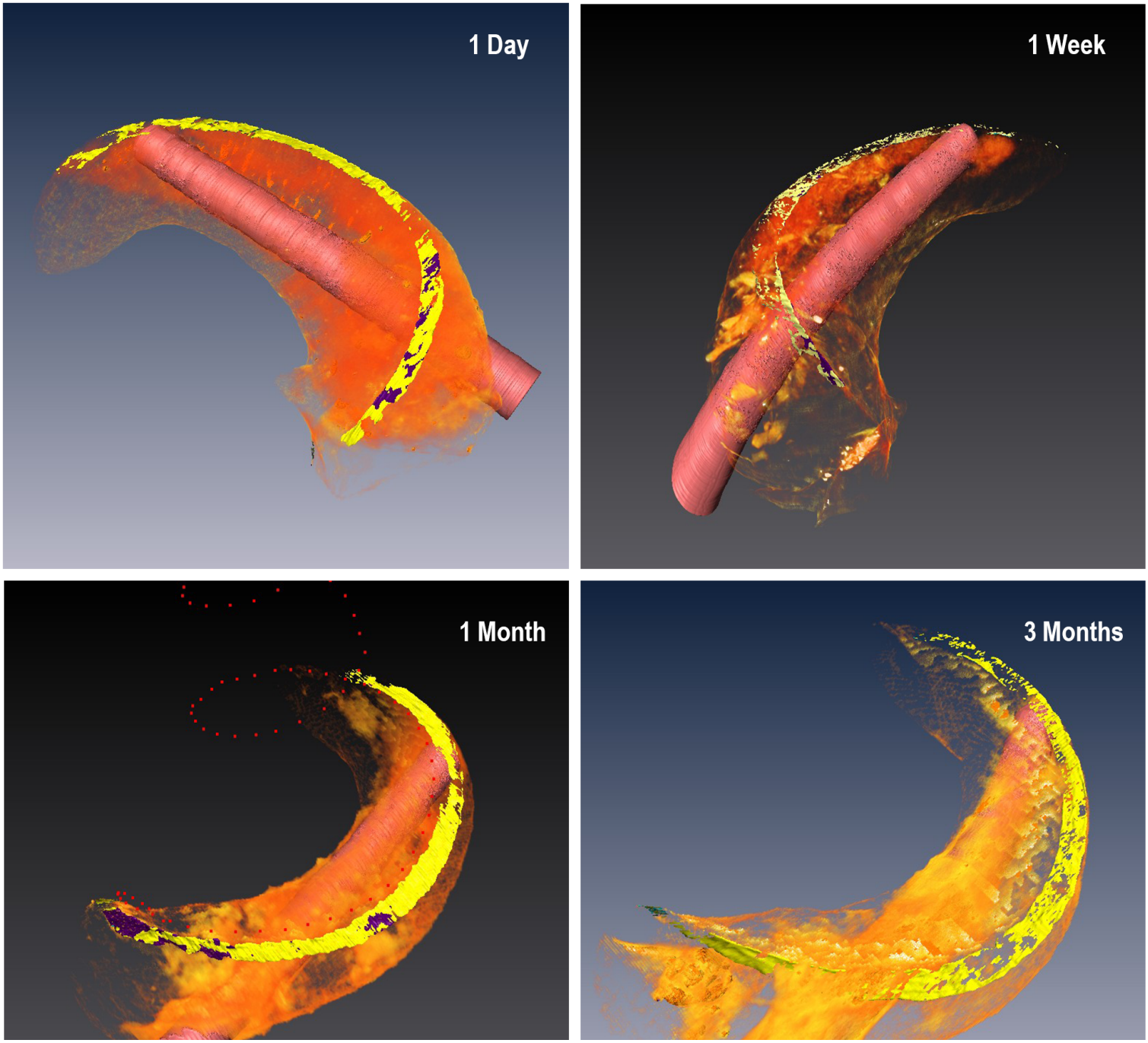

Figure 4-10 - Tissue response after cochlear implantation. All four images from different timepoints are rendered using a similar process, described in Tissue Response Rendering Technique. The electrode is rendered as an opaque pink solid, while the tissue response is volume rendered to demonstrate radiodensity through the colour-map. Contact between the basilar membrane and tissue response is rendered in yellow. Scale bars are not included because these are three dimensional representations, but scale can be gleaned by the 400µm diameter of the electrode. The dotted red line in the '1 month' image is the Organ of Corti lineset.

4.2.4.3.2 Tissue Response Quantitative Analysis

To facilitate further quantitative analysis of the 'Tissue Response' material, some anatomical markers were defined. A LineProbe was used to mark the modiolar axis of the cochlea, as previously described in *Evaluation of Cochlear Hydrops*. Furthermore, a BSpline along the length of the of the Organ of Corti was defined by placing points at the location of the cuticular plate of the inner hair cell. This BSpline was converted to a LineSet, with the resultant data being utilised to create the tonotopic map of the individual cochlea, as well as a marker for measurement of proximity of tissue response to the Organ of Corti.

Once materials, modiolar axis marker and Organ of Corti LineSet had been defined, the data was passed via a Matlab connection module to custom code created by Dr Luke Campbell. Dr Campbell's code performed measures in virtual transmodiolar sections of the cochlea at 500Hz intervals along the cochlear tonotopic map. In each virtual section, Matlab would measure the total cross-

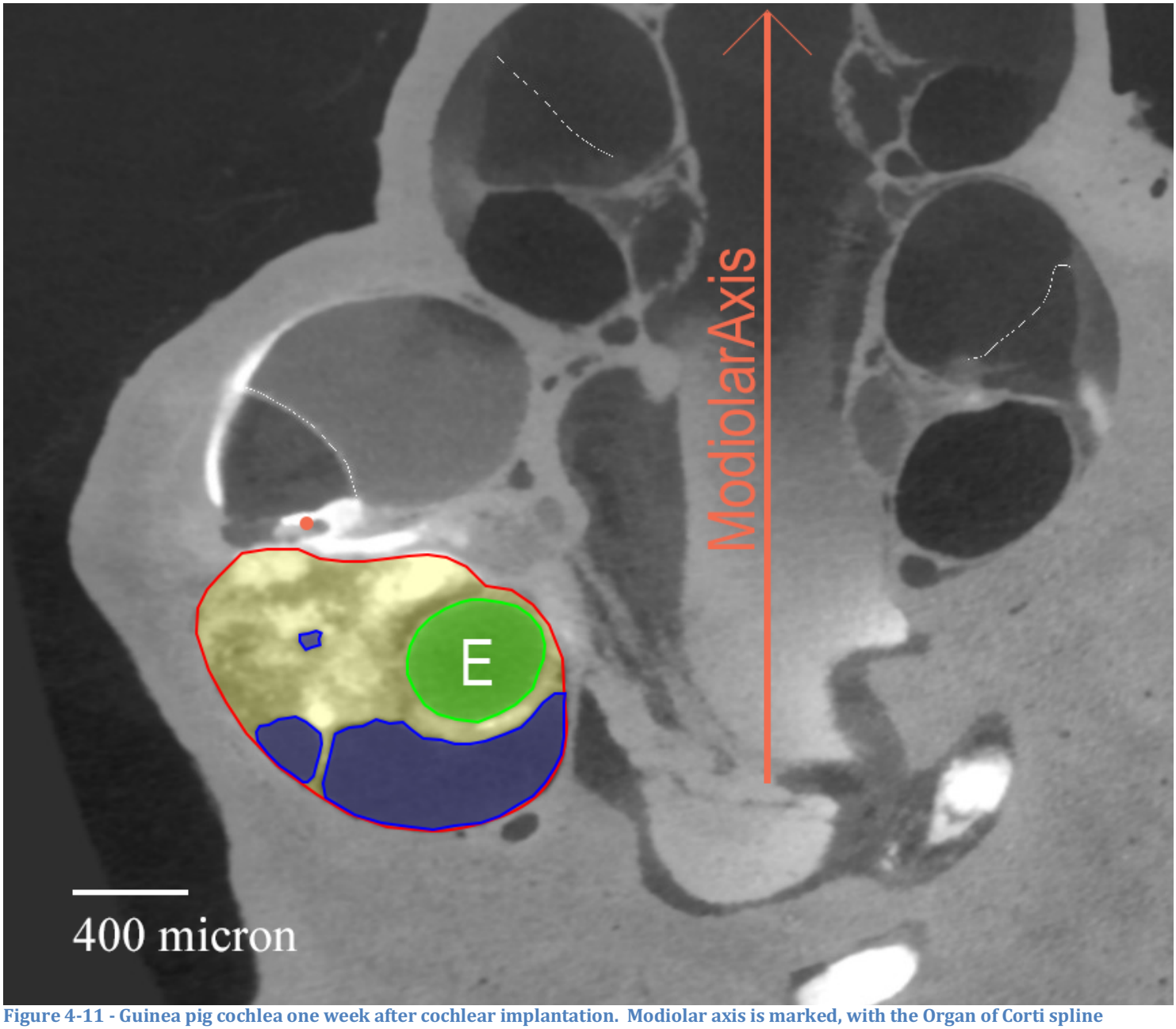

Figure 4-11 - Guinea pig cochlea one week after cochlear implantation. Modiolar axis is marked, with the Organ of Corti spline defined by a point (orange) placed approximating the cuticular plate of the IHC. The cross sectional area of the scala media in the basal turn is outlined in red, with areas of perilymph highlighted in blue and tissue response in yellow. The electrode (E) is highlighted in green. Endolymphatic hydrops is present adjacent in the marked section of the basal turn.

sectional area of the scala tympani as well as the proportion of that cross-section filled with low radiodensity material, ie. perilymph (Figure 4-11). A circle of 200μm radius would also be created around the Organ of Corti line, with the area of that circle occupied by the 'Tissue Response' material measured. A centroid was also calculated for each virtual slice through the scala tympani, with this point and the orientation of the modiolar axis LineProbe used to define the area of the scala tympani into quadrants. This division was utilised by Dr Henrik Smeds (Smeds et al., 2015) to quantitatively describe the position of the tissue response to cochlear implantation.

4.2.4.4 Evaluation of Saccular Volume

The location and conformation of the saccule of the guinea pig (Curthoys, Uzun-Coruhlu, Wong, Jones, & Bradshaw, 2009), mouse (Honda et al., 2015) and human (Mukherjee et al., 2011) have previously been described using μCT, but changes in saccule volumes in disease states have not been evaluated using the same technique. Evaluation of saccular volume was also performed using segmentation. Because of the variability of osmium staining of the membranous labyrinth and the beam-hardening effect of the nearby cochlear nerve, manual selection of the saccule was performed on every fifth slice through the central portion of the saccule, with interpolation of the intervening slices. The extremities of the saccule, particularly at the junction of the ductus reuniens, required manual segmentation of each slice. Once segmentation had been performed, a MaterialStatistics module was connected to the Labelfield to derive

the volume of the organ in voxels. Known voxel dimensions allowed conversion of the resulting volumes into μm^3.

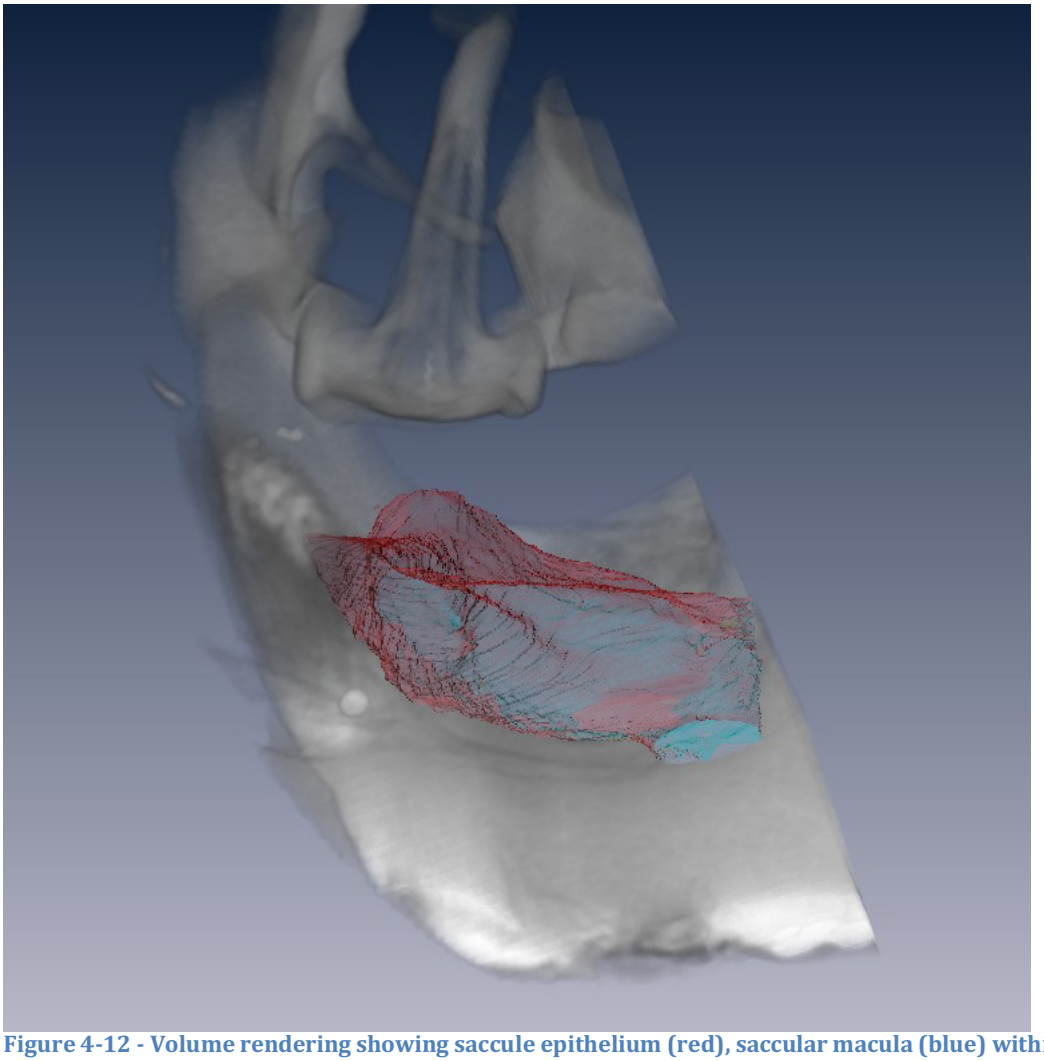

Figure 4-12 - Volume rendering showing saccule epithelium (red), saccular macula (blue) within the left vestibule. Stapes in cross-section superiorly.

4.2.4.5 Determination of Electrode Path

Electrode path was determined using a BSpline defined by points placed at the centre of the cross-section of the electrode along its path. BSplines were also created to represent the positions of the osseus spiral lamina, medial wall of scala tympani and lateral wall of scala tympani. Once these splines were created, they were converted to LineSets and exported to MatLab. Custom routines in MatLab (developed by Dr Luke Campbell) allowed the distances between the

centre of the electrode and the walls of the scala tympani, osseous spiral lamina, basilar membrane to be determined along the intracochlear path of the electrode. This techniques has since also been applied by our group to data acquired using our TSLIM apparatus (Lo, Sale, et al., 2017b), or conventional histopathology(Rowe et al., 2016).

4.2.4.6 Imaging of Ductus reuniens

Ductus reuniens was able to be identified connecting the most extreme basal end of the cochlear duct to the saccule in the anterior portion of the vestibule.

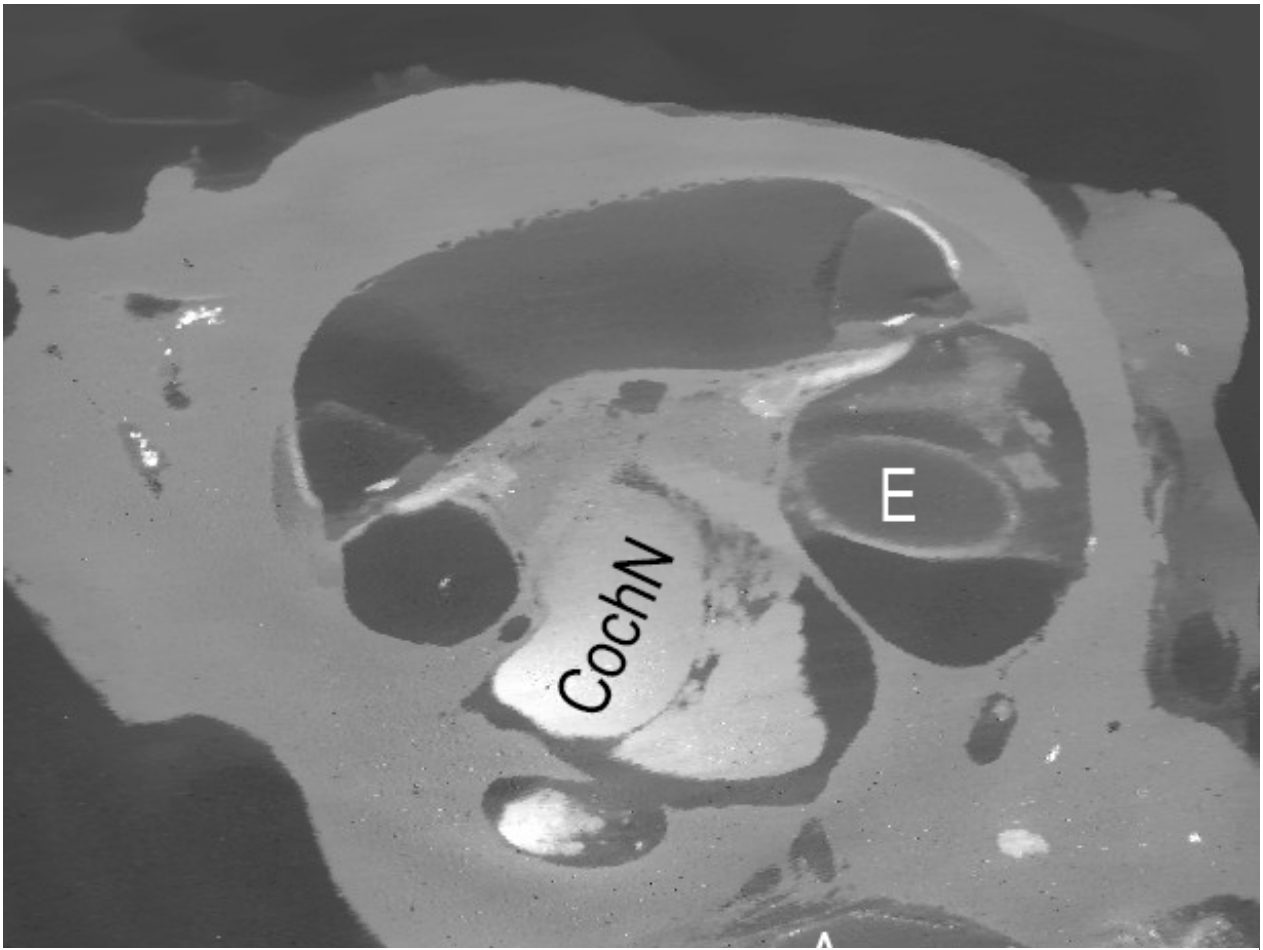

Figure 4-13 - Planar view through the vestibule and basal turn of the cochlea, with a dummy electrode (E) in situ. The Cochlear nerve (CochN) stains intensely with osmium tetroxide.

A BSpline was generated, using orthogonal OrthoSlice modules and tailored ObliqueSlice modules to aid placement of points along the centre of the ductus reuniens from saccule through to cochlear duct. A CurvedSlice module was connected to the Ductus BSpline, generating a longitudinal planar image along the length of the defined BSpline and thus along the length of the Ductus reuniens (Figure 4-14).

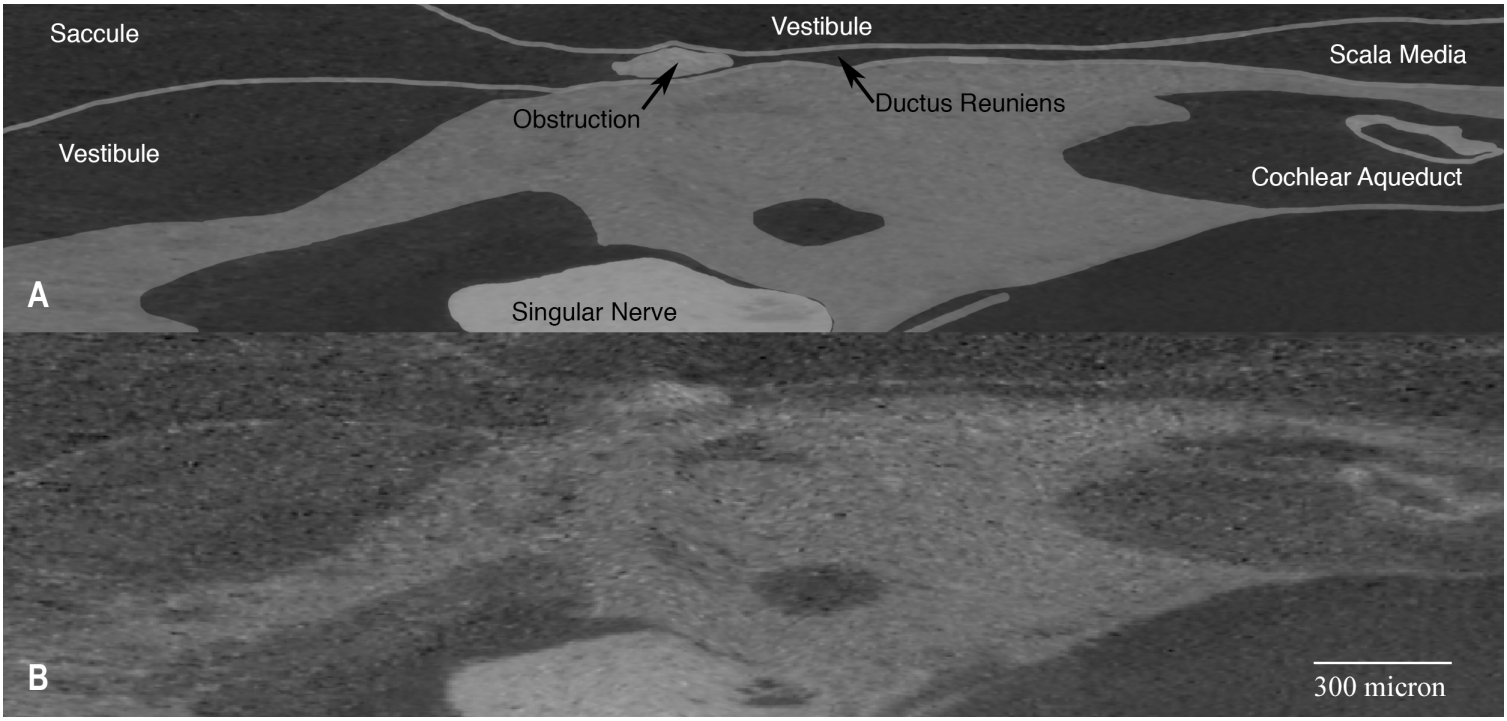

Figure 4-14 - A Curved Slice generated along the axis of the Ductus reuniens, in raw form (B) and schematic form (A). High density material is present near the saccular orifice of the Ductus ('Obstruction').

At the scanning resolution utilised for hydrops evaluation, the ductus reuniens is, on average, approximately 5-6 voxels in diameter. This figure is consistent with the measurements of the guinea-pig ductus published by Konishi (Konishi, 1977), who found the ductus to be 30μm in diameter at its narrowest point. These small voxel dimensions, combined with image noise and the thin membrane of the ductus make utilisation of automated propagation techniques

to determine the patency of the ductus impossible. Noise reduction via Non-Local Means (Appendix - Non Local Means Filtering) was generally not sufficient to remedy this, but made qualitative evaluation of the ductus status more practicable.

4.3 Results

4.3.1.1 Endolymphatic Hydrops

The techniques developed were first utilised for the quantitative evaluation of cochlear endolymphatic hydrops in Dr Henrik Smeds' work, 'Endolymphatic hydrops is prevalent in the first weeks following cochlear implantation'(Smeds et al., 2015). Using my frequency-specific mapping of Reissner's membrane morphology, Smeds' paper demonstrated a strong correlation between subjective morphological classification of the position of Reissner's Membrane (concave, neutral or convex) with the Scala Media Area Difference (SMAD) returned by the technique ($r = 0.878$, $p < 0.0005$). Smeds' paper also demonstrated significantly higher SMAD at Days 1, 7 and 28 after implantation when compared to day 84. SMAD peaked in the Day 7 measures. Correlation was also demonstrated between SMAD and whole-cochlea averaged SP/AP ratio change ($r_s = 0.770$, $p < 0.0005$).

4.3.1.2 Tissue Response

Evaluation of quantity and location of tissue response to cochlear implantation using the described segmentation technique was first published in work performed in conjunction with Dr Henrik Smeds (Smeds et al., 2015).

The segmentation and analysis technique described above and formulated by the author was able to be applied to animals operated upon by Dr Smeds,

demonstrating that the tissue response was stable across the four measured timepoints (1 day, 7 days, 28 days and 84 days) in terms of overall volume (0.93mm^2 mean) and occupied proportion of cross-sectional area of scala tympani (median 0.59) (Smeds et al., 2015).

What isn't demonstrated through measurements of volume and cross-sectional area is the makeup of the tissue response at different points in time after cochlear implantation. Organisation and homogenisation of the tissue response is apparent on Micro-CT as survival after cochlear implantation increases. These changes have been demonstrated on histological examination by our group (Kel, Tan, Eastwood, Wongprasartsuk, & O'Leary, 2013), with the tissue response at 7 days (Micro-CT at same timepoint in (Smeds et al., 2015)) consisting of a resolving red blood cell and fibrin clot being infiltrated with an acute inflammatory infiltrate along with some fibroblasts. 4-weeks after implantation, histopathological examination of the tissue response to cochlear implantation by our group (S. J. O'Leary, Monksfield, Kel, Connolly, Souter, Chang, Marovic, O'Leary, Richardson, & Eastwood, 2013b) demonstrated a dominant population of fibrocytes, with a mixed fibrous and giant cell sheath surrounding the electrode. This sheath was tethered to the scala tympani endosteum by evolving areolar fibrous tissue. The Micro-CT equivalent of this timepoint is seen in an example in Figure 4-15.

Moving forward to the 12-week timepoint, Micro-CT demonstrates (in Figure 4-16) a dense sheath surround the circumference of the electrode (E), with organised lower density material tethering this sheath to the modiolus, osseus

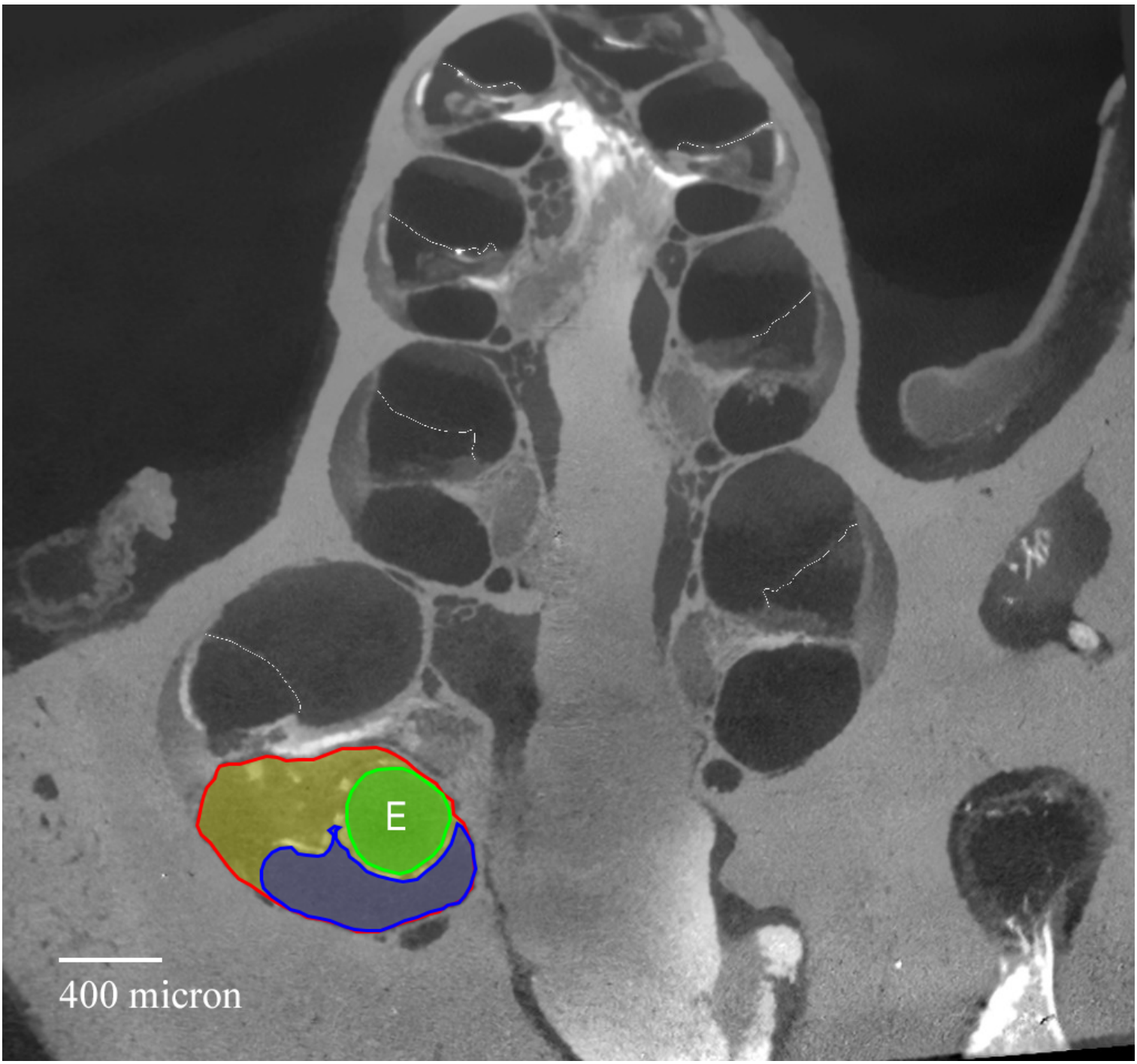

Figure 4-15 - Tissue response example, 1 month after cochlear implantation. Electrode is highlighted in green and marked (E). Scala tympani perilymph is highlighted in blue, with the margins of scala tympani marked in red and tissue response in yellow.

spiral lamina and lateral scalar wall. This ensheathing of the electrode is also demonstrated in Figure 4-17 viewed from within the hook region of the cochlea.

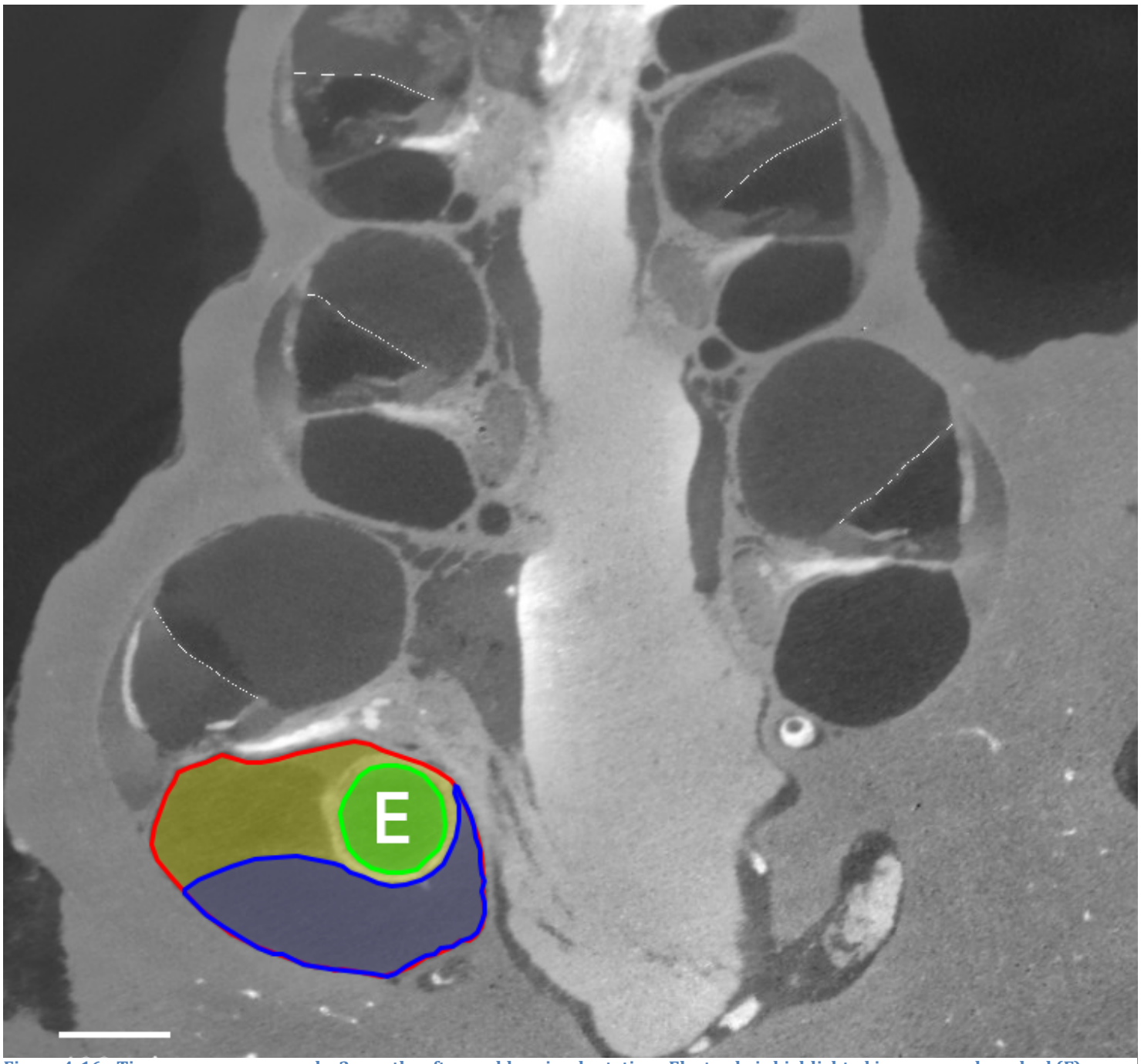

Figure 4-16 - Tissue response example, 3 months after cochlear implantation. Electrode is highlighted in green and marked (E). Scala tympani perilymph is highlighted in blue, with the margins of scala tympani marked in red and tissue response in yellow.

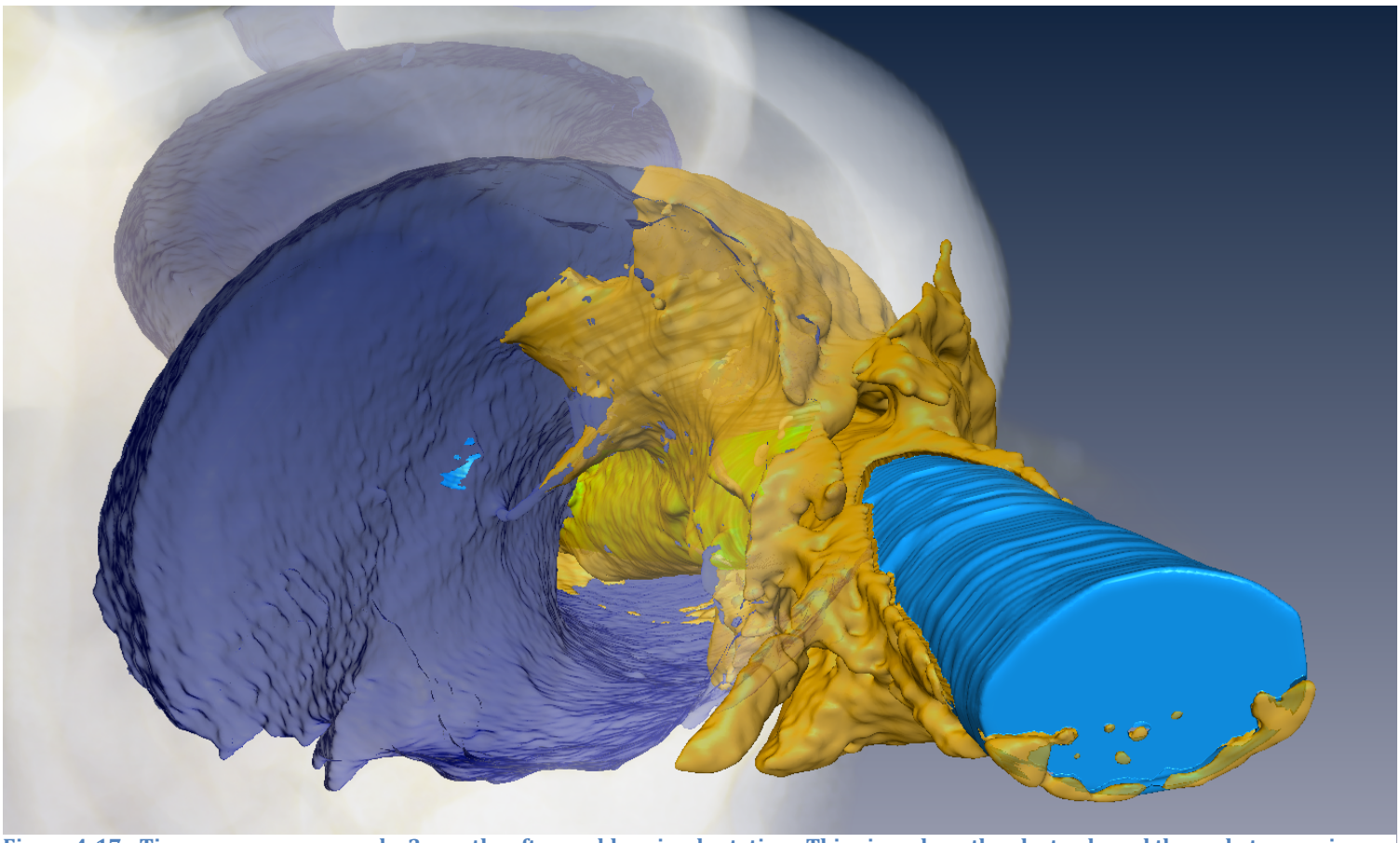

Figure 4-17 - Tissue response example, 3 months after cochlear implantation. This view along the electrode and the scala tympani (endosteum rendered in dark blue) of the basal turn demonstrates the evolving tissue-response sheath (yellow surface) around the electrode (light blue).

This segmentation-based technique has been shown to be effective in other volumetric datasets such as those acquired on our TSLIM apparatus (Lo, Campbell, et al., 2017a).

4.3.1.3 Saccular Volumes

Staining of the specimen with osmium tetroxide allowed for visualisation of the thin saccular epithelium adjacent to dense otic capsule bone. The staining of saccules in our specimen was, within the acquired data sets, as reliable as that of the soft tissues of the cochlea. 33 of 52 specimens had at least 'moderate' staining of all turns of the cochlea, allowing reliable evaluation of RM position along the full length of the scala media as seen in Smeds, et al. (Smeds et al.,

2015), while 38 of 52 saccules were at least moderately stained through their visualised portion. Unfortunately, the field of view at this degree of magnification is small, with the reconstructed volume being a cylinder approximately 5.3mm in height and diameter. This meant that attempts at simultaneous imaging of saccule and cochlea resulted in an incompletely imaged saccule, with only 15 saccules being completely included in that volume. Eight saccules fulfilled both criteria for volumetric measurement and are thus included in **Error! Reference source not found.**.

Table 4-2 - Characteristics of specimens included in analysis of saccular volume

Animal number	Side	Timepoint (days)	Cochlear Hydrops	Saccule Volume (μm^3)	
29	Control	1	None	537921984	
2	Implant	7	All turns	474023936	
3	Implant	7	Basal turn	405114688	
5	Implant	7	Basal turn	347106848	
4	Implant	7	Basal turn	291455616	
5	Control	7	None	475087136	$p = 0.02$*
4	Control	7	None	412214592	
8	Control	84	None	472792736	

Re-imaging of specimens at a later date to gain volumetric data was hampered by formation of osmium salt precipitates within the membranous labyrinth and was thus abandoned.

The mean volume of the measured saccules was 426964692µm^3, or 0.43 (+/- 0.08) mm^3. All of the included implanted specimens had displayed cochlear hydrops involving at least the basal turn of the cochlea. Overall, there was no significant difference in saccular volumes when comparing all animals displaying cochlear hydrops with those having a normally positioned RM (p = 0.09), but there was a trend toward reduced saccule volumes in animals with an implant/hydrops (mean volume 0.38 mm^3 vs 0.47mm^3). There were two animals included (highlighted in Table 4-2) where pairwise comparison could be made. Both animals were imaged at one week after surgery and displayed cochlear hydrops in their basal turn. The implanted sides with cochlear hydrops demonstrated significant reduction (p = 0.02) in their saccular volumes compared to the unoperated controls (mean volume 0.32mm^3 vs 0.44mm^3).

4.3.1.4 Ductus Reuniens Patency

As described earlier, the primary objective of the µCT was evaluation of endolymphatic hydrops and tissue response after cochlear implantation, which meant that imaging of the ductus reuniens was suboptimal. Apparent higher levels of noise within the peripheries of the imaged volume and the small dimensions of the ductus meant that automated methods of determining patency of the system were impossible in most cases. Partial volume averaging of the thin membrane of the ductus saw it appear to be discontinuous in some parts, while its radiodensity was often similar to the apparent radiodensity of adjacent

noise (Figure 4-14). Propagation and thresholding techniques of automated segmentation were planned as objective determinants of patency, but rely on the patent system having contiguous voxels of fluid radiodensity along the whole length of the ductus. More aggressive noise reduction could improve the chances of successful propagation, but risked unintended smoothing of radiodense debris within the lumen or further membrane discontinuity.

Table 4-3 Observed ductus reuniens status. A ductus was determined to be patent when a radiolucent fluid density was continuous along the length of the ductus. A collapsed ductus saw the walls of the ductus in apposition at some point, with resulting discontinuity of the fluid density. An obstructed ductus was identified where radiodense material filled the entire cross-section of the ductus lumen at some point along its length. Not all specimens were assessable due to incomplete staining ('NA').

Side	Timepoint (days)	Patent	Obstructed	Collapsed	NA
Left	**1**	1	1	0	3
	7	2	2	1	1
	28	1	2	0	3
	84	1	4	2	3
Right	**1**	4	1	0	1
	7	1	1	2	0
	28	0	4	1	1
	84	2	4	2	1

Qualitative assessment of the ductus reuniens saw it categorised as patent, obstructed, collapsed or not assessible (NA)(Table 4-3). An 'obstructed' ductus assessment was made where a fluid signal was apparent along the length of the ductus apart from a focal and total intraluminal obstruction, such as that seen in Figure 4-14 or Figure 4-18. A 'collapsed' ductus assessment was made when there was no focal intraluminal obstruction, but a fluid signal could not be followed from scala media to saccule despite adequately stained ductus epithelium. Ductus patency was not assessible where staining was inadequate or excessive noise prevented localisation of the epithelium.

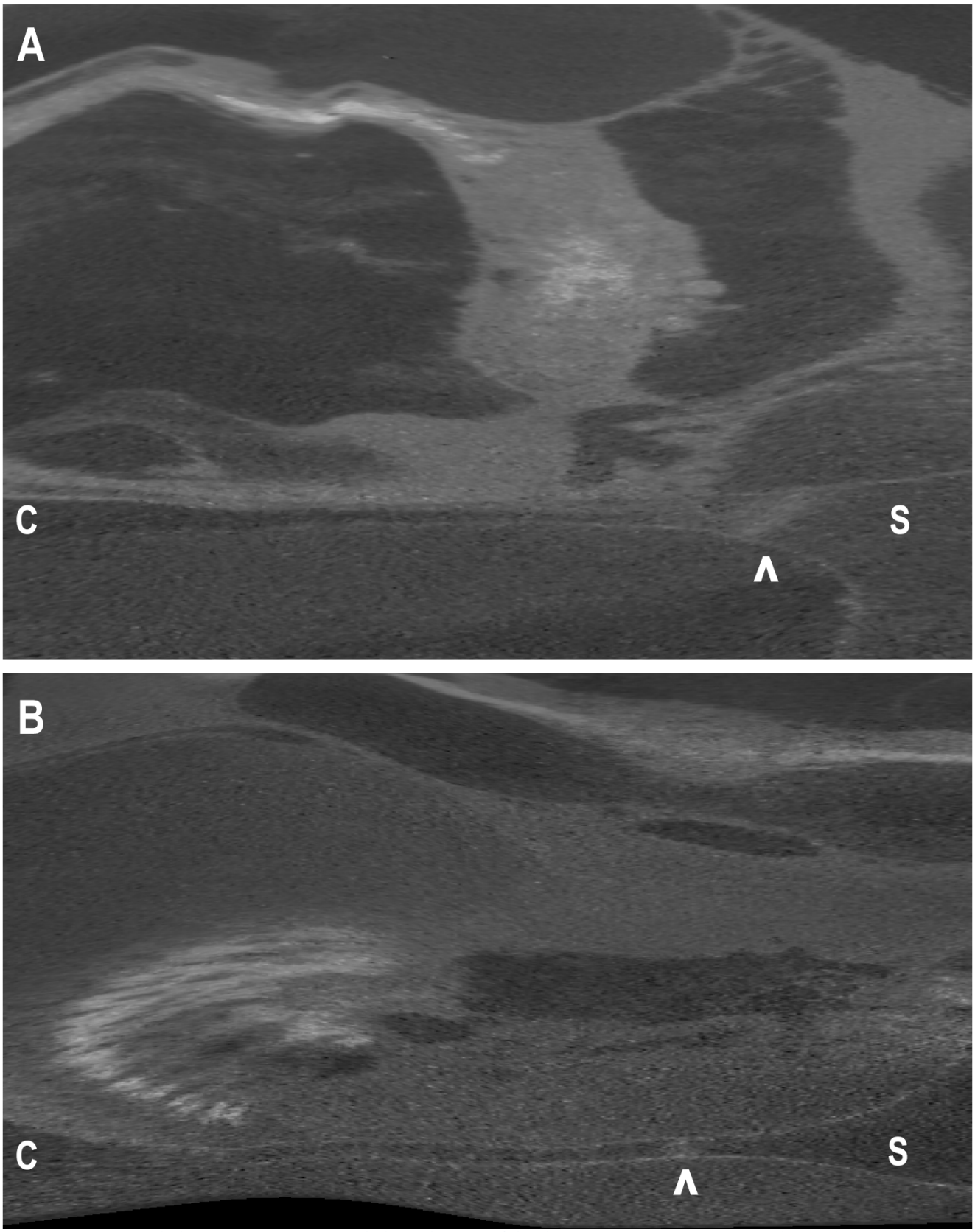

Figure 4-18 - Curved planar images generated along the axis of the ductus reuniens in two animals. Both images demonstrate relatively radiodense material (^) filling the ductus lumen just beyond the saccular orifice (S), while the cochlear end of the ductus appears patent (C)

There was no association between side (implanted vs control) and ductus patency (patent ductus vs [obstructed + collapsed]) on Fisher's Exact test (p = 1.00), nor between side and the presence or absence of an intraluminal obstruction (p = 0.7512).

Attempts were made at re-imaging of ductus reuniens and the adjacent saccule after the conclusion of the original experiment, but it became evident that longer term storage of osmium stained specimens generally resulted in the formation of radio-dense osmium salt precipitates within the labyrinth which limited their utility.

4.4 Discussion

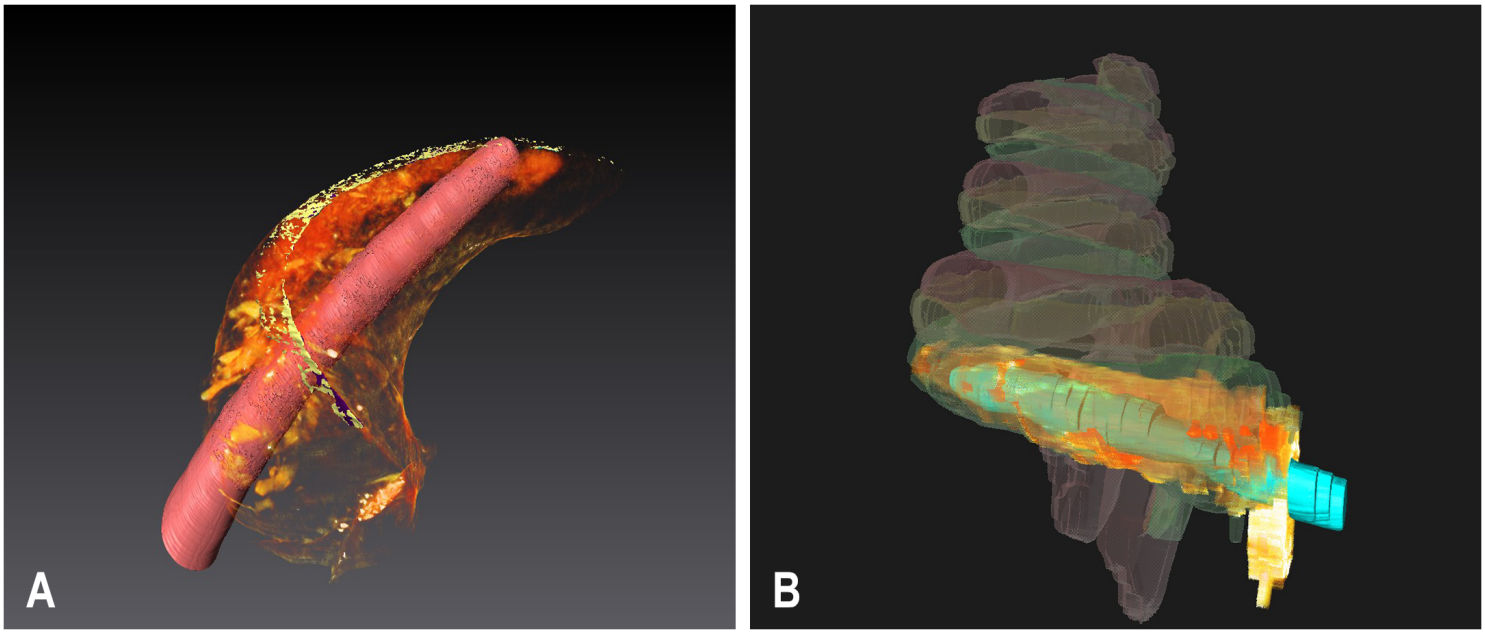

Figure 4-19 - Segmented three dimensional visualisation of cochlear implant electrode tissue response, using µCT (A) and large numbers of serial histological sections (B) demonstrating the difference in z-axis resolution. The reconstructed light microscopy specimen involved greater than 30 slices per cochlea to obtain this spatial information.

μCT has been established in the literature base as an important tool in evaluation of the vestibulocochlear apparatus of animals through its non-destructive process, improved z-axis information and relative labour-sparing nature. The techniques described above add physiological information to the predominantly anatomical mode in which μCT has been utilised over the past 15 years.

4.4.1 Osmium Tetroxide staining

Heavy metal-staining of cochlear soft tissues helps overcome the difficulty inherent in simultaneous imaging of radio-dense otic capsule bone and the relatively radiolucent and delicate soft tissues of the cochlear scalae and membranous labyrinth. However, heavy metal-staining introduces some new difficulties in specimen handling. Dehydrated osmium salts are very hazardous substances, with the handling of aquaeous solutions being simpler. The aqueous solutions stain skin, containers, and the specimen itself a dense, coal-like black. This black staining makes it difficult to achieve precise specimen positioning within the μCT apparatus as anatomical landmarks are obscured. Also apparent was the existence of an optimum time-period after specimen staining during which it should be scanned – this appears to be approximately two weeks. After this time, osmium begins to precipitate in the fluid-filled spaces of the vestibule and cochlear scalae. These radio-dense accumulations can distort fine membranous structures and introduce surrounding beam-hardening artefact, obscuring delicate soft tissues. These issues mean that the 'non-destructive' nature of μCT comes with some caveats. It is non-destructive in the sense that anatomical relations are preserved and the specimen imaged largely in the condition that it existed at the termination of the experiment: this is particularly important when it comes to results being defined by small changes in position

and length of fine structures such as Reissner's Membrane in endolymphatic hydrops. The non-destructive nature does not extend to specimens being available to be utilised and re-imaged in perpetuity, nor are they likely to be useful for reimaging or examination using other modalities such as light microscopy. It is thus recommended that careful consideration is made as to the adequacy of μCT to evaluate all desired aspects of a specimen before commencing osmium-staining. It is also recommended that all foreseeable imaging procedures be performed on a specimen in the time period shortly after staining has finished to avoid later disappointment when further information is sought.

4.4.2 Z-Axis Resolution

Z-axis resolution, or the distance between slices of a volume when considering the conventional histopathological process, tends to be limited by the time and financial costs. Z-axis resolution in μCT can be limited by these some constraints, but to a lesser extent. Once the desired number of x-ray projections are reconstructed into a cylindrical volume, the contained voxels are isotropic. The size of these voxels will be defined by:

1. Relative position of the x-ray source, the specimen and the detector.
2. Power of the intervening microscope objective
3. Dimensions (sensor pitch) and number of pixels on the detector
4. Pixel-binning, if employed

The specified voxel dimensions will also have implications for the field of view (FOV): in this case the dimensions of the cylindrical volume obtained after tomographic reconstruction.

Consideration also needs to be made of the voxel level grey resolution and the voxel dimensions of the end data set and the resulting requirements in terms of data storage and computational power. Our group made some compromises in μCT parameters to facilitate faster scanning, reconstruction and image-processing times with a result that we obtained an approximately 5.3mm tall cylindrical dataset with isotropic voxels of 5.2μm sidelength. These parameters were more than adequate for evaluation of the position of Reissner's Membrane and implant-related tissue response, but were inadequate for detailed or automated examination of ductus reuniens. Similarly, the small field of view meant that simultaneous imaging of the complete saccule was unsuccessful in the majority of cases.

4.4.3 Saccular volume changes

When considering the small number of adequate specimens, we demonstrated reduction of saccular volumes in animals with post-implantation hydrops at day 7 after implantation. There was a non-significant trend toward a reduction in saccule volumes in animals with post-implantation hydrops at all measured timepoints. These findings echo those of Handzel (Handzel et al., 2006), where post-implantation cochlear hydrops was seen to be associated with saccular collapse. The use of Micro-CT adds weight to these findings by imaging the saccule non-destructively and avoiding distortion of the thin membranous labyrinth through tissue slicing.

Handzel, et al (Handzel et al., 2006) and Ishiyama, et al (Ishiyama et al., 2016), propose that interruption of endolymph flow may be responsible for the development of cochlear hydrops after cochlear implantation. They examined the ductus reuniens in their cases of post-implantation cochlear hydrops but did

not find an association between hydrops and obstruction of the ductus. Whilst we have been able to demonstrate ductus obstruction due to high density material in some post-implantation specimens, this was not evident in any of the specimens which simultaneously demonstrated sufficient saccular staining to allow volume measurement through the segmentation technique described.

4.4.4 Ductus reuniens

Ductus obstruction (Handzel et al., 2006), perhaps by otoconial debris (Hornibrook & Bird, 2017; Takano, Iguchi, Sakamoto, Yamane, & Anniko, 2013; Yamane et al., 2014; 2010) or adjacent fibrosis (Ishiyama et al., 2016)has been suggested by some to be an etiologic factor in the development of endolymphatic hydrops. While I was able to demonstrate in multiple instances a ductus reuniens that was occluded at its saccular orifice by material of high radiodensity this was found to be not responsible for the development of cochlear hydrops in the related work published by Smeds, et al (Smeds et al., 2015).

4.5 Conclusion

The combination of Amira-based image processing and Matlab-based computation (developed by Dr Luke Campbell) opens up significant possibilities in the analysis of the cochlea's response to implantation. Techniques developed in this chapter have been applied in published works using μCT (Smeds et al., 2015) as well as being expanded to other cross-sectional imaging modalities such as stacked conventional histology (Rowe et al., 2016) and Thin-Sheet LASER Imaging Microscopy (TSLIM) (Lo, Campbell, et al., 2017a).

5 Experiment 3 – Changes in Cochlear Vascular Permeability after Cochlear Implantation visualised using TSLIM

5.1 Introduction

Inflammation is associated with the cochlear response to injury, and has been observed in noise trauma (Hirose, Discolo, Keasler, & Ransohoff, 2005), ototoxicity (Sato, Shick, Ransohoff, & Hirose, 2009), antigen challenge (Satoh, Firestein, Billings, Harris, & Keithley, 2003), and inner ear surgery (Kel et al., 2013). This inflammation can be associated with loss of cochlear function that leads to a dilemma for cochlear implantation; patients with significant residual hearing may be ideal candidates for electroacoustic hearing, but the inflammation associated with implantation may deprive them of this possibility through a loss of hearing. In light of this, there have been efforts of reduce cochlear inflammation in CI surgery in the peri-operative period. The most widely studied approach has been the administration of corticosteroids. In order to optimise drug-regimes to control cochlear inflammation following CI, the time-course of the inflammatory response to this surgical procedure, and its location within the cochlea (relative to the original site of injury) must be understood. This will determine the ideal duration of drug treatment, and better define the regions of the cochlea that need to be targeted to protect hearing following surgical intervention. The aim of this project is to introduce a method where the cochlear inflammatory response can be semi-quantified within a 3D volumetric representation of the cochlea.

The stria vascularis is key to the generation and maintenance of the endocochlear potential (EP) and the cochlear endolymph necessary for hearing function. Derangements of function of the stria vascularis through perturbations in cochlear blood flow or the function of the blood-labyrinthine barrier (BLB) are implicated in many forms of sensorineural hearing loss, through failure of maintenance of the endocochlear potential (F. Zhang et al., 2013a), changes in endolymph volume (Sakagami et al., 1995), or the facilitation of passage of ototoxic compounds into the endolymphatic space (Dai & Steyger, 2008).

All components of the BLB have been found to be susceptible to insults of different kinds, be it acoustic trauma causing pericyte (PC) remodelling (Kel et al., 2013), inflammatory- or excitotoxic- induced down-regulation of tight-junction complexes in the strial capillary endothelium, excitotoxicity causing detachment of perivasacular resident macrophage-like melanocyte (PVM/M) processes from endothelial cells (F. Zhang, Zhang, Neng, & Shi, 2013b) or age-related changes in PC and PVM/M morphology and density (Neng et al., 2015). These changes can also result in increased permeability of the BLB complex to proteins, while via increased expression of proteins such as inter-cellular adhesion molecule-1 (ICAM1) , circulating leucocytes adhere to the ICAMs and extravasate into the tissue from where they may contribute directly to the inflammatory response or migrate into the cochlear scalae .

These changes within the lateral cochlear wall extend the inflammatory response beyond the initial site of injury, and this is thought to be the mechanism by which cochlear sensory cells are lost at locations remote to the site of lesion in

the days to weeks after cochlear implantation, particularly apical to the electrode (Eshraghi et al., 2005).

Evans Blue is a 980 Dalton azo-dye compound that binds irreversibly to albumin. It has been utilised for some time as a tracer for albumin; and thus plasma, loss from the intravascular compartment (Kruse & McMaster, 1949; Sutherland & Young, 1966). It is often quantified destructively via tissue digestion and then quantitative spectrophotometry, either directly or using fluorescence (Xu et al., 2001). Evans Blue fluorescent properties also allow localisation of tracer on confocal scanning laser microscopy (Abraham et al., 1996), conventional fluorescence microscopy (Cheol Hee Choi et al., 2012; Jang et al., 2011; Schmutzhard et al., 2012; T. Suzuki et al., 2008), or through Light-Sheet Fluorescence techniques as performed by our group.

Here we performed cochlear imaging of the distribution of a protein that extravasates in the presence of increased cochlear vascular permeability. This protein was administered intravenously, at varying times following the induction of cochlear inflammation in a guinea-pig model. The guinea-pig cochleae were harvested, imaged using thin sheet LASER imaging microscopy (TSLIM) and the resulting stacks of cross-sectional images reconstructed in three dimensions. This allowed a time-course of the vascular permeability (a surrogate of the acute inflammatory response) to be mapped across cochlear tonotopic place. In this study, CI surgery was the procedure used to initiate cochlear inflammation, with the cochlear response to a local application of lipopolysaccharide acting as a positive control.

5.2 Methods

Ethics approval for the described experiment was obtained from the Animal Research Ethics Committee of the Royal Victorian Eye and Ear Hospital. Guinea pigs were anaesthetised for all procedures using a combination of intramuscular injection of ketamine (60 mg/kg, Troy Laboratories Pty Ltd, Sydney, Australia) and xylazine (4 mg/kg, Troy Laboratories Pty Ltd) as per institutional protocol.

5.2.1 Timeline

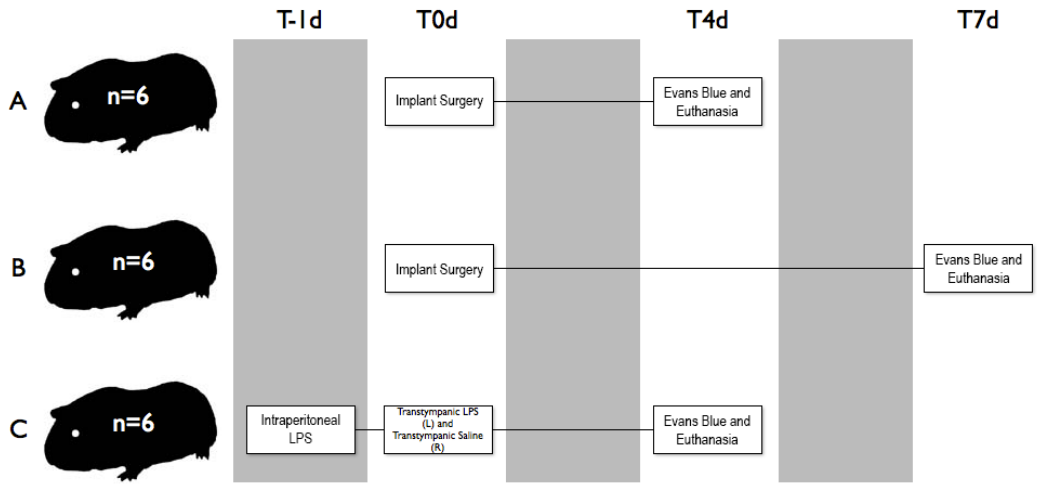

Figure 5-1 - Three groups were utilised for this experiment, as detailed in the timeline above. Two underwent implant surgery, whilst the third was designed to represent an 'inflamed' control through the use of bacterial lipopolysaccharide(LPS).

Three groups of animals were utilised as seen in Figure 5-1. Two groups underwent left-sided cochlear implantation using a silastic dummy-electrode, with the two groups differing according to the time until sacrifice and thus,

imaging. A third, inflammatory control group underwent sensitisation to Lipopolysaccharide (LPS) (0.8mg/kg bodyweight via intraperitoneal injection), one day prior to intratympanic injection of 0.1% LPS in the left ear and normal saline in the right ear. All injections were performed by a single operator (PS). All dummy electrodes were inserted by a single operator (Dr David P Rowe).

5.2.2 Evans Blue Administration

At the end of the experiment, animals were transferred anaesthetised to the operating table for intravascular administration of Evans Blue. The technique of administration is described in *Evans Blue Dye Administration* 2.1.7.

5.2.3 Specimen Preparation

After administration of Evans Blue dye, animals were euthanised and specimens harvested as described in 2.2.2 *Specimen Preparation for TSLIM*.

5.2.4 Imaging

The TSLIM apparatus is demonstrated diagrammatically in Figure 2-2 and is modelled on those described by Santi (Santi et al., 2018). The operating with respect to generating a three-dimensional dataset is described in detail in 2.3.1 *TSLIM Acquisition.*

Evans Blue extravasation was quantified by measuring its fluorescence on TSLIM.

TSLIM acquisitions were performed with a 640nm (+/- 2nm) bandpass filter (FB640-10 – ThorLabs, Newton, MA) to quantify Evans Blue using its primary emission peak when stimulated by a 532nm diode LASER. Sensor sensitivity was

set at ISO 1600, with a 2 second exposure. XYZ stitching of multiple acquisitions for each slice was performed to allow imaging of the entire cross-section of the cochlea using the confocal region of the LASER sheet. A second set of acquisitions was performed without an emission filter to allow imaging of anatomical details through tissue autofluorescence as demonstrated in Figure 5-2. Exposure settings for the unfiltered dataset were 1/30 of a second, again with sensitivity of ISO 1600. The CMOS camera was tethered to a desktop computer (Dell, Round Rock, USA) running custom LASER-, micropositioner- and camera-control software developed by Dr Luke Campbell. Slices were stitched in the X and Y dimension using a proprietary software (Matlab - MathWorks, Natick, USA) routine developed by Dr Luke Campbell, with the resulting file reduced in X and Y dimensions by 50% using batch image-processing software (Faststone Image Viewer; Faststone Soft Inc)

5.2.5 Data Extraction

The paired datasets were imported into Amira 5.6 (FEI Software, Hillsboro, USA) on an Apple Mac Pro (Apple Computer, Cupertino, USA) desktop computer running the Mac OS X 10.8.4 Operating System. Due to the large dimensions of each stitched slice, a single channel of data from each dataset was imported to minimise resulting file size and RAM usage. Luminance data was extracted from the Emission-filtered dataset, whilst the green channel of the RGBa unfiltered dataset was extracted as the best representation of tissue autofluorescence as stimulated by a 532nm LASER ((Santi et al., 2018)). Voxel dimensions (2µm x 2µm x 10µm – x:y:z) were the same for both datasets because of the identical stitching and slicing parameters.

5.2.6 Tonotopic Mapping

Tonotopic mapping relies on accurate measurement of the length of the organ of corti for each individual animal. In previous work, our group has utilised a Bezier spline constructed from points placed approximating the cuticular plate of the inner hair cells (IHCs) along the length of the organ of Corti from the hook region to the helicotrema (Smeds et al., 2015). 99 points were generally used to define this spline, with the interval between points tailored to the changing radius of curvature along the length of the cochlear spiral. A shorter interval between points was used apically because of the shorter radius of curvature. Once this spline had been defined, it was converted to a lineset defined by 300 equally spaced points. Frequency-place maps of the mammalian cochlea according to Greenwood (Greenwood, 1990) and Wada(Wada et al., 1998) see characteristic frequencies mapped to locations at proportions of the total length of the organ of corti, so division of the organ of Corti spline into equally spaced points means that a given point along the organ of Corti spline will represent a particular frequency despite variation in total length of the organ of Corti between animals. Examination of emission data from pilot animals had demonstrated the spiral limbus as a reliable location of Evans Blue extravasation and its presence alongside the full-length of the organ of Corti make it suitable for generating a tonotopic map using the same method.

Further BSplines were generated marking the positions of the Type 2 and Type 4 fibrocyte regions of the lateral wall of the cochlea ((Smeds et al., 2015)), having also been identified as areas of Evans Blue extravasation in pilot animals. A FilteredObliqueSlice module was used to view the dataset and place the points

defining the BSpline so that the start and end points of the respective splines exist at the same angle of rotation around the modiolus as the start and end points of the spline defining the tonotopic map.

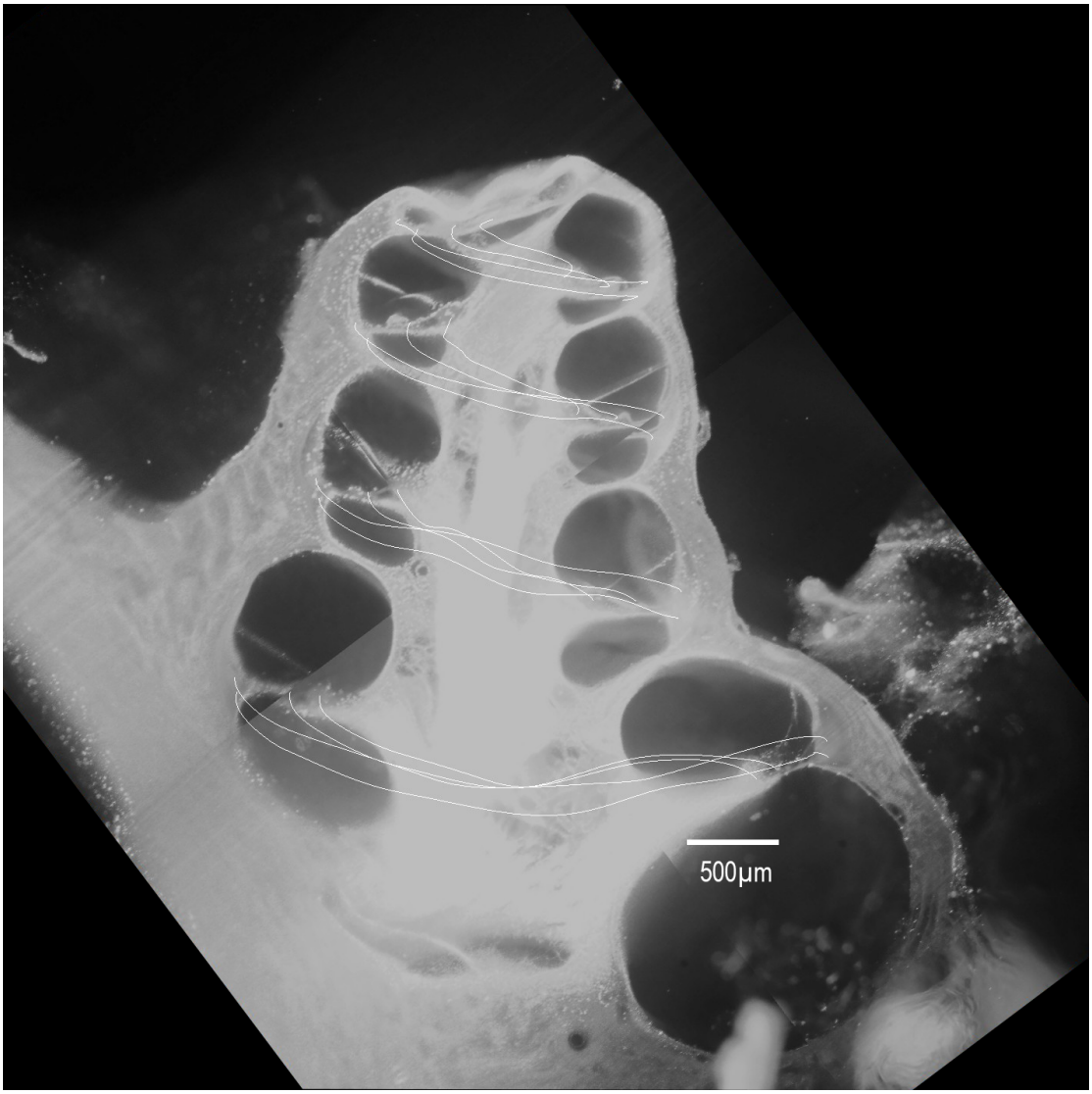

Figure 5-2 - Utilising the green channel from an unfiltered acquisition to gain anatomical information eases placement of points to make up a spline marking the location of anatomical regions along the length of the cochlear spiral

The defined BSplines were connected to LineSetProbe modules to determine the luminance value for the emission-filtered data at 300 points along the defined BSpline.

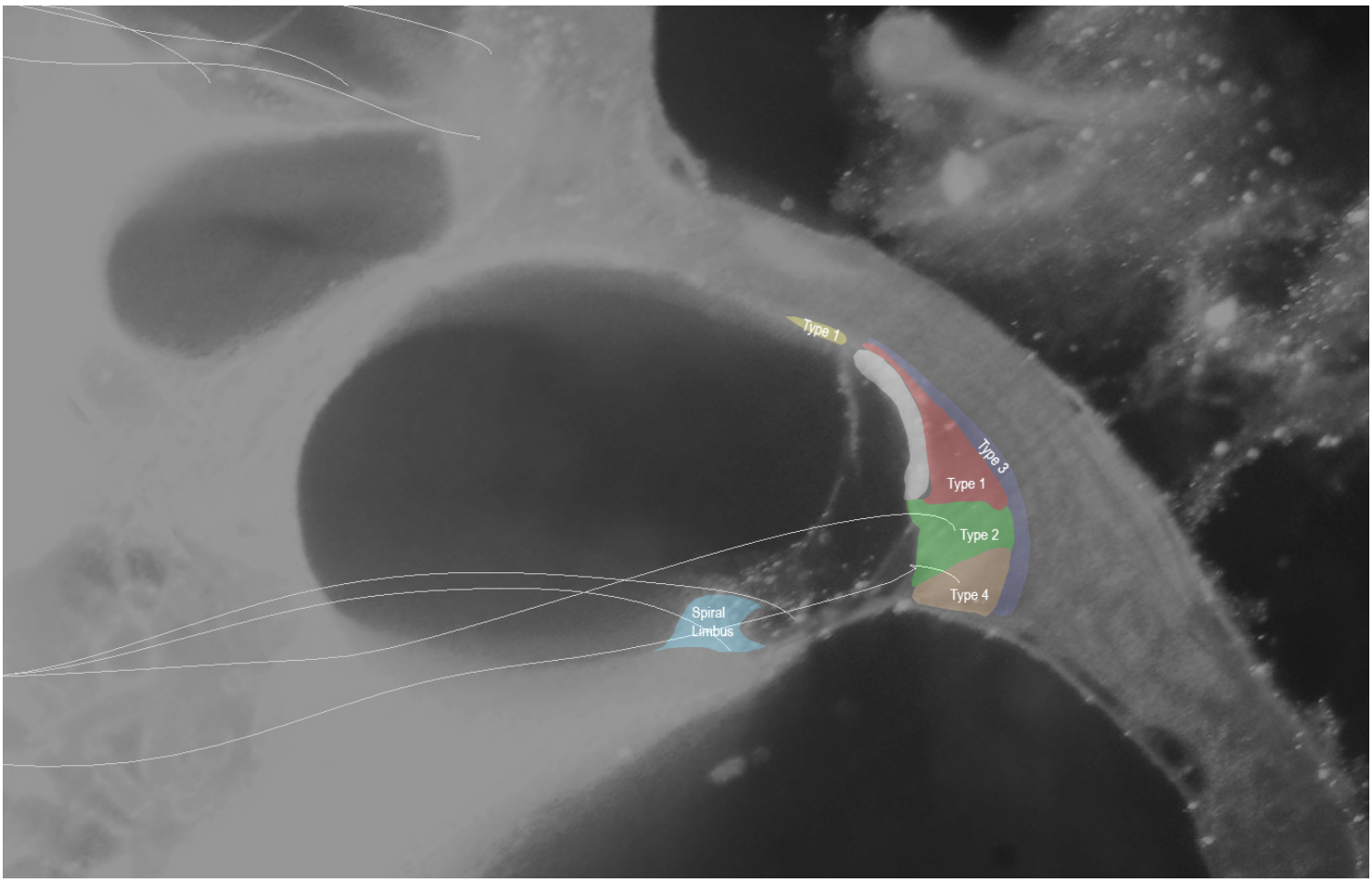

Figure 5-3 - Green channel from an unfiltered TSLIM RGBa acquisition, where tissue autofluorescence provides anatomical information. The fibrocyte populations of the spiral limbus and spiral ligament are marked and labelled. The stria vascularis is highlighted in white.

Table 5-1 - Tonotopic locations for a 300-point spline placed along the Organ of Corti, as derived from Wada's adaptation of Greenwood's equation.

Frequency (Hz)	PointID
32000	19
24000	36
16000	59
12000	76

8000	99
4000	139
2000	179
1000	219

.

5.2.7 Extraction of outliers and normalisation

Preliminary examination of the specimens saw variability in the degree of tissue autofluorescence in the unfiltered datasets. Outlying datasets were excluded by examining their emission data in Matlab. The mean tissue autofluorescence was calculated for each specimen using the 8-bit data (values 0..255) contained in the green channel from the unfiltered RGBa dataset at the 300 equidistant points defined by the BSpline placed along the otic capsule bone adjacent the Type 3 fibrocyte region. A specimen was excluded from analysis if its mean autofluorescence was less than 20% of the specimen within the group with the highest mean autofluorescence. The distal 50 points in the Bsplines; corresponding to a region well apical from the 1000Hz point in the tonotopic map were also excluded from analysis, as this point was fenestrated in some specimens to allow aspiration of air bubbles from the Spalteholz fluid.

At any point along the cochlear spiral, emission data was normalised using the intensity of autofluorescence of adjacent otic capsule bone to correct for LASER fall-off across the specimen. BSplines for the background bone autofluorescence and the Regions of Interest (ROI) were started and finished at the same point within the three-dimensional volume. This mean that numbered points within

the BSplines for each ROI occurred at the same place along the cochlear duct and thus the same point in the tonotopic map. Intensity of otic capsule bone adjacent the Type 3 fibrocyte region at the respective point along the spline was treated as background, with the intensity of the 640nm filtered emissions from the ROI divided by the green autofluorescence of the adjacent otic capsule bone as obtained from the green channel of the unfiltered RGBa dataset.

Utilisation of unfiltered autofluorescence data was hampered somewhat by scatter of the 532nm LASER by microscopic bubbles within the Spalteholz fluid, causing some undesired variability in the green values harvested from the RGBa dataset.

5.2.8 Quantitative Analysis

Descriptive statistics demonstrated that the fluorescence intensity datasets were non-parametric (Matlab). The existence of non-parametric data along with three matched groups saw the Friedman's One-Way Repeat Measures ANOVA utilised to detect an effect of animal group on fluorescence intensity. Friedman's Statistic (F_r) was converted to a p-value through the use of a lookup table considering numbers of subjects and repeated measures.

5.3 Results

Cochlear structure is apparent on the TSLIM images. In the whole-cochlear images presented in Figure 5-2, the 3D rendered images have been optically sectioned in the mid-modiolar plane. This provides a perspective on the

cochlear turns as they spiral around the modiolar axis, but also a microscopy-like image of the cochlear structure at the “surface” cut.

In unfiltered images, cochlear structure is apparent and the Evans Blue has been represented in red. The Evans Blue fluorescence is seen clearly within the blood vessels spiralling around the inner cochlear walls, providing evidence that the method developed here successfully detects this protein. Evans Blue signal is also apparent within the tissues of the cochlea.

In animals that had undergone cochlear implantation, the electrodes were removed prior to imaging because reflections and refraction by the silastic dummy electrode generated significant artefact when illuminated by the light sheet. The place of the implant is seen as an outline in the tissue reaction cast within scala tympani. Because a straight electrode was utilised, the electrodes were able to be moved during tissue processing without disrupting the surrounding cast. This reaction is apparent as a “tissue” of soft-tissue intensity on the TSLIM images, and is known to be thrombus and blood clot immediately after surgery, that has been invaded by macrophages and fibroblasts at one week after implantation(Kel et al., 2013).

5.3.1 Comparisons Between Ears

Friedman’s One-Way Repeat Measures ANOVA was utilised to detect group effects for different regions of interest.

5.3.2 LPS

Within the group of animals treated with intratympanic LPS, interaural differences were detected at all the characterised Regions of Interest. The Friedman statistics were sufficient for $p < 0.01$ for all these ROIs.

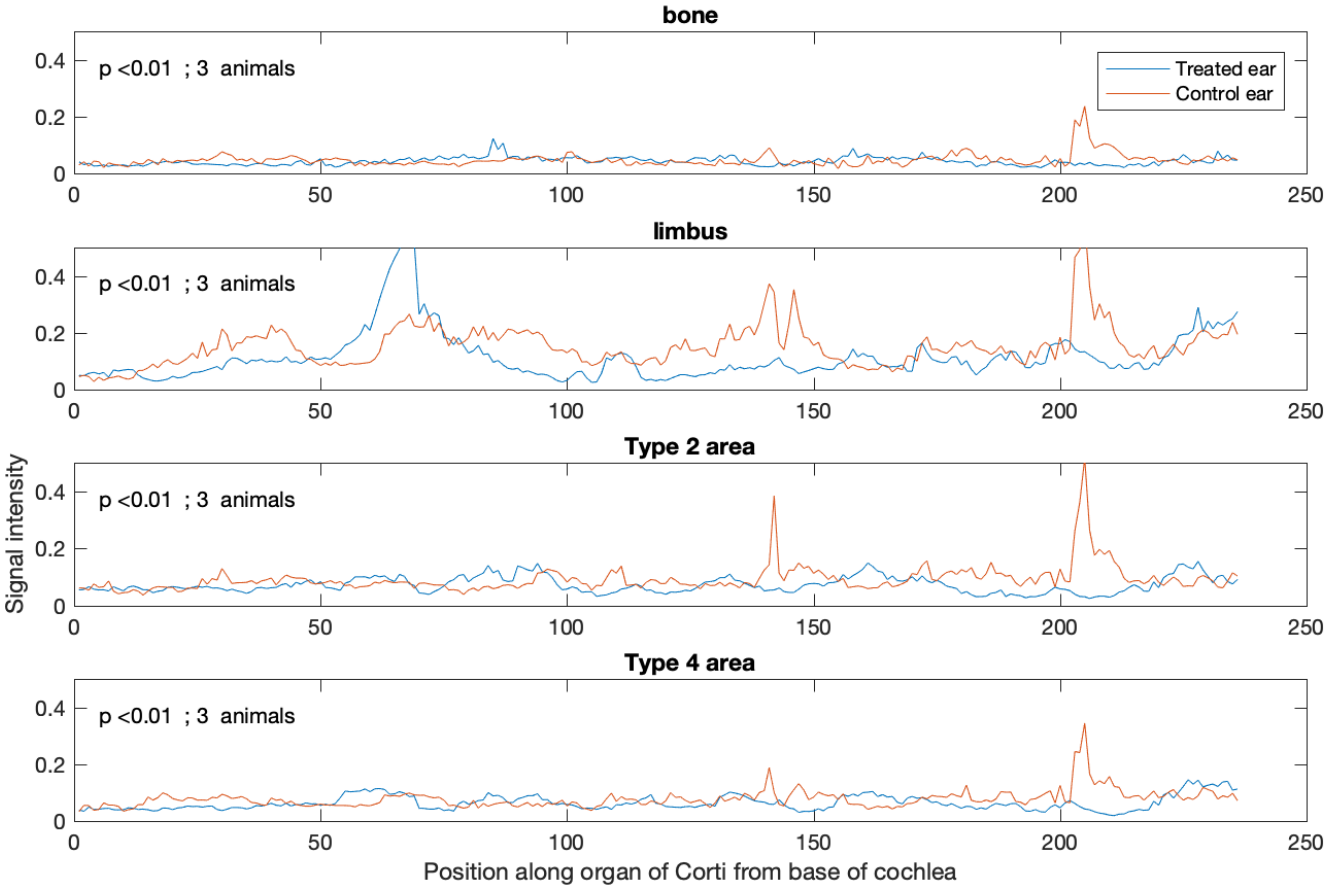

Figure 5-4 – LPS group mean normalised fluorescence for control (red) and treatment (blue) ears, with *p*-values derived from the Friedman Statistic (F_r)

5.3.3 Day 4

In the group of animals who received a dummy cochlear implant electrode and were sacrificed on the fourth post-operative day, interaural differences were detected by Friedman's one-way repeat measures ANOVA at all characterised ROIs, with Friedman's statistic sufficient to provide $p < 0.01$ at all ROIs. Distinct

increases in signal intensity were noted in the soft tissue ROIs around point 125-130, which with the utilised dummy electrode and the group's standard guinea-pig cochleostomy would be just apical to the tip of the electrode dummy(Smeds et al., 2015).

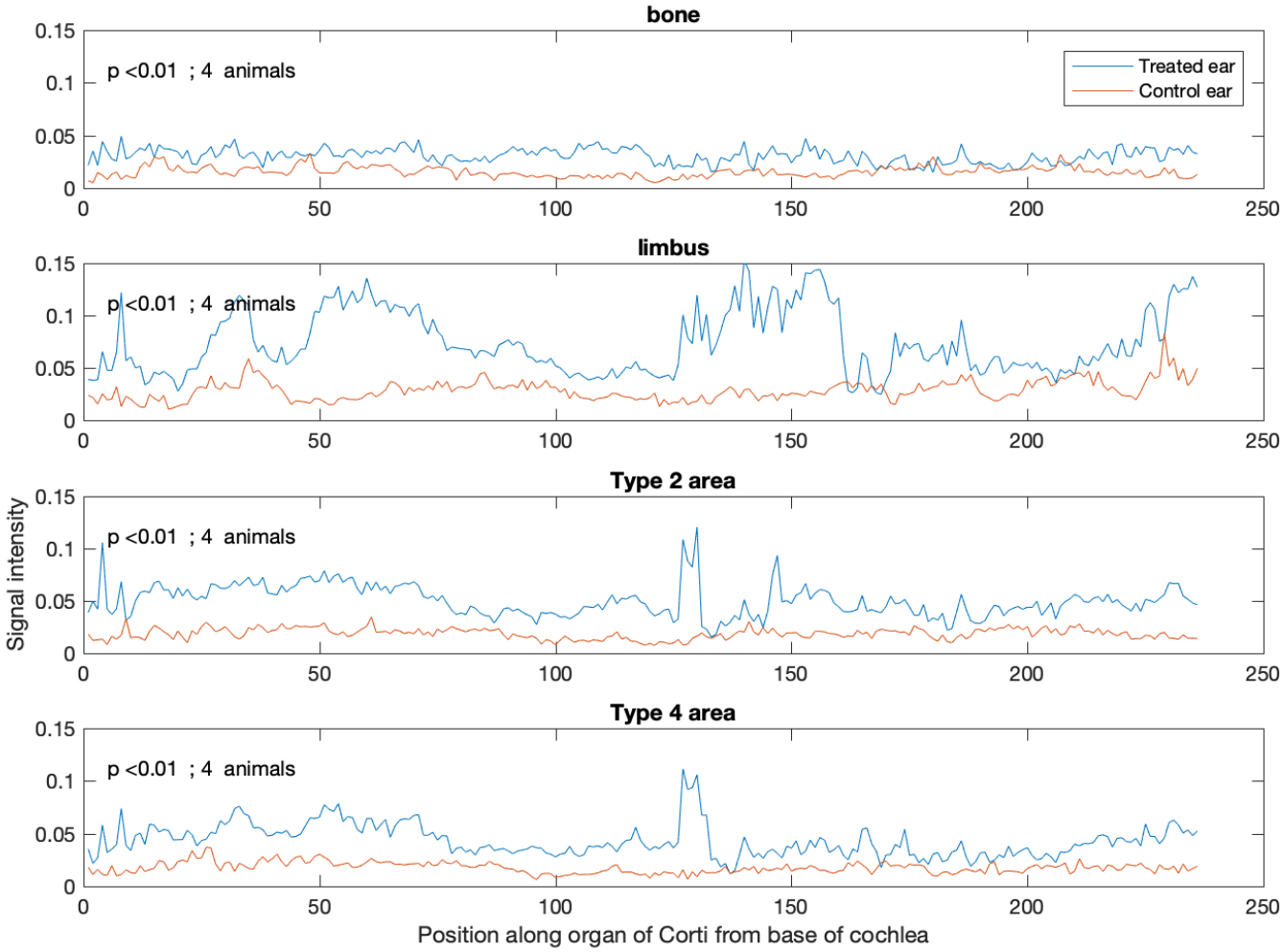

Figure 5-5 - Day 4 group mean normalised fluorescence for control (red) and treatment (blue) ears, with p-values derived from the Friedman Statistic (Fr)

5.3.4 Day 7

In the group of animals who received a dummy cochlear implant electrode and were sacrificed on the seventh post-operative day, an interaural difference was detected by Friedman's one-way repeat measures ANOVA only in the ROI of otic

capsule bone adjacent the Type 3 Fibrocyte region, with $p < 0.01$. No interaural difference was detectable at the ROIs corresponding to the spiral limbus, nor the

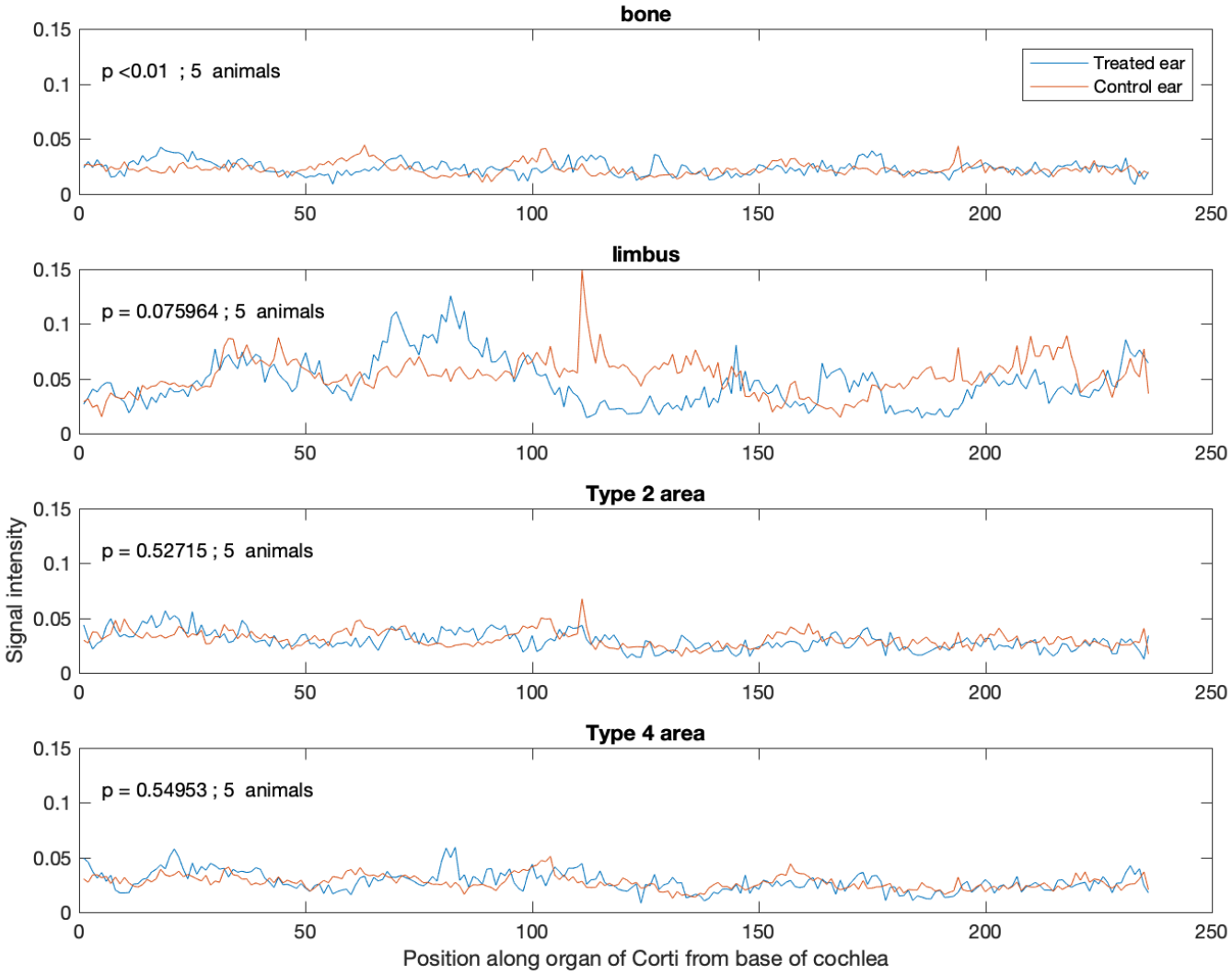

Figure 5-6 – Day 7 group mean normalised fluorescence for control (red) and treatment (blue) ears, with p-values derived from the Friedman Statistic (Fr)

Type 2 or Type 4 fibrocyte regions of the lateral cochlear wall.

5.3.5 Region of Interest

Examining the plots for the LPS group, high magnitude spikes are visible in the plots for the control animals, particularly around point 210, just basal to the tonotopic region of 1kHz. These spikes in the control data reached values of ~0.5, far in excess of the maximal values seen in the other experimental groups

where maxima were generally around 0.15. The effect of these data spikes on the Friedman Statistic is illustrated with supplemental plots below. The proportion of animals (y axis) in which fluorescence intensity of the treated ear exceeded that of the control ear by proportional criteria of 0.1-1 (y axis). Each line is data from a different experimental group (LPS, 4- or -7 day post cochlear implantation). Each subplot is data from a different ROI (a-d: bone, limbus, Type 2 area and Type 4 area).

It becomes apparent that a very small proportion of the LPS animals had a large proportion of data points where the treatment fluorescence intensity exceeded the control in any of the ROIs. The positioning of the '4 d' data points toward the top right corner of the same plots illustrates the more consistent increase in signal intensity seen in those treatment ears.

a)

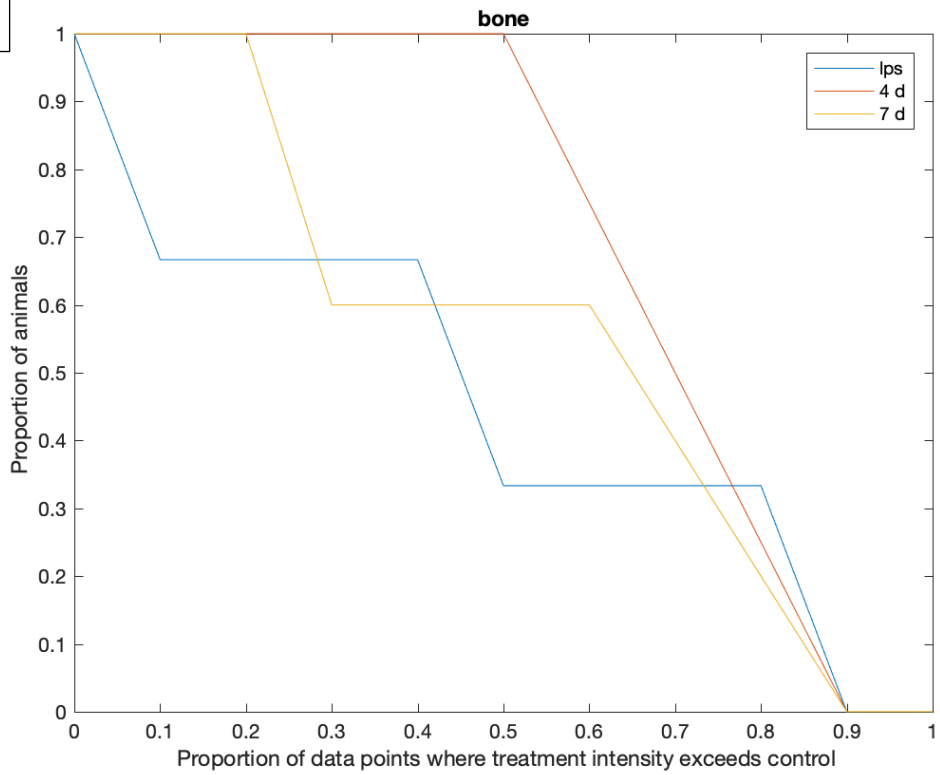
bone
lps
4 d
7 d
Proportion of animals
Proportion of data points where treatment intensity exceeds control
0
0.1
0.2
0.3
0.4
0.5
0.6
0.7
0.8
0.9
1

b)

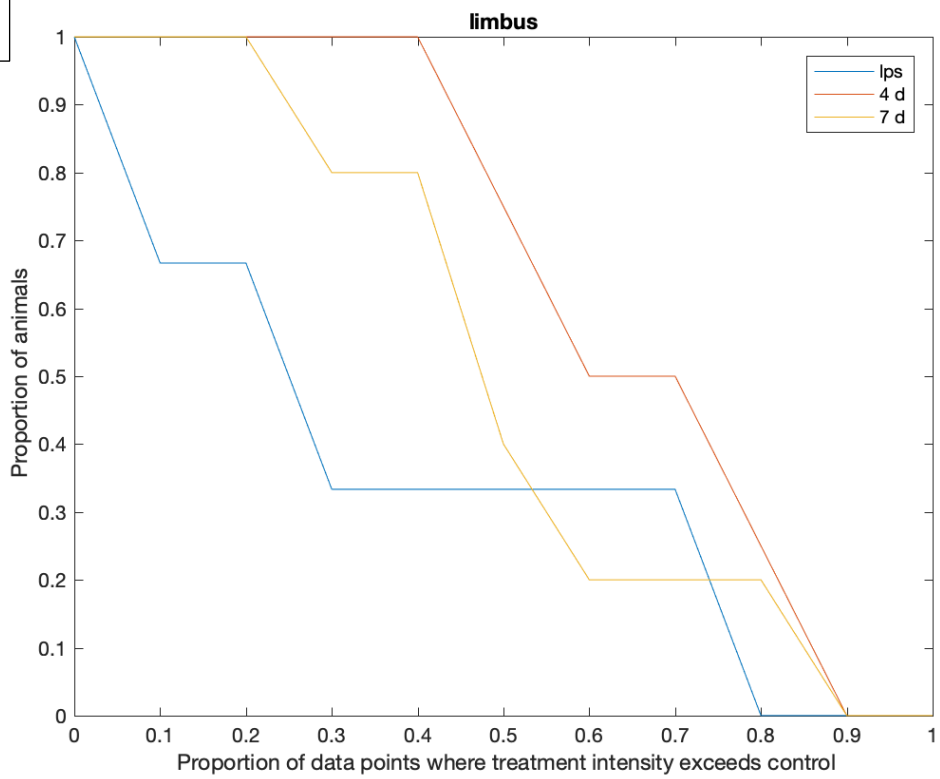
limbus
lps
4 d
7 d
Proportion of animals
Proportion of data points where treatment intensity exceeds control
0
0.1
0.2
0.3
0.4
0.5
0.6
0.7
0.8
0.9
1

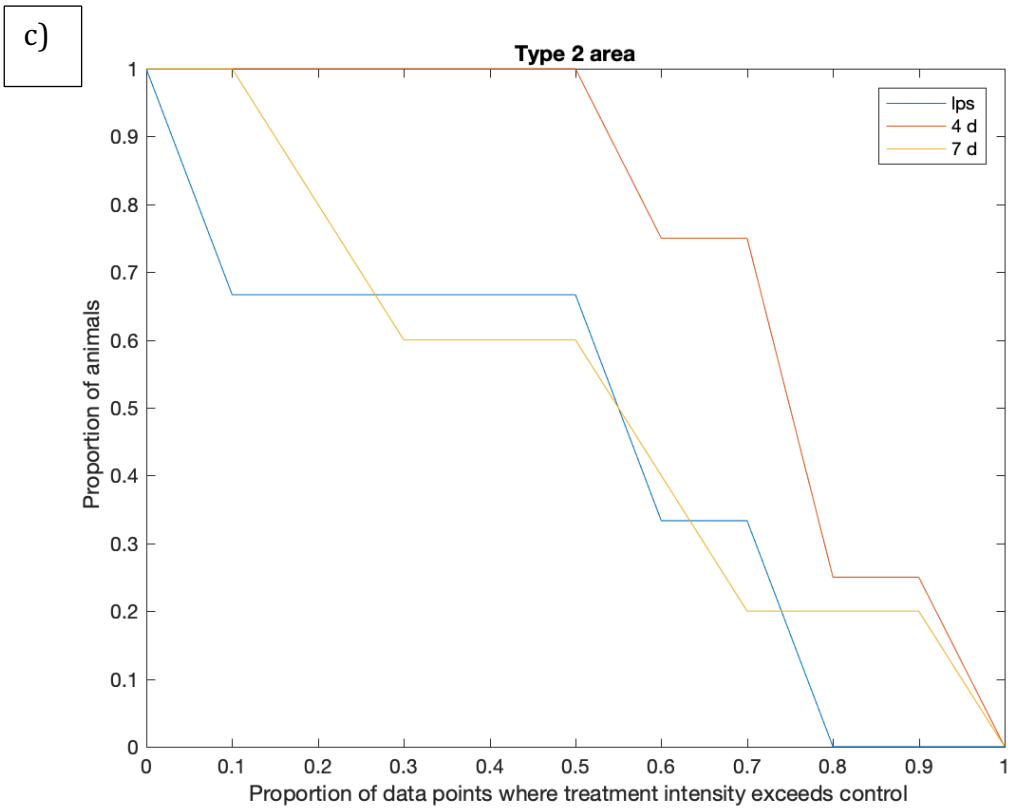

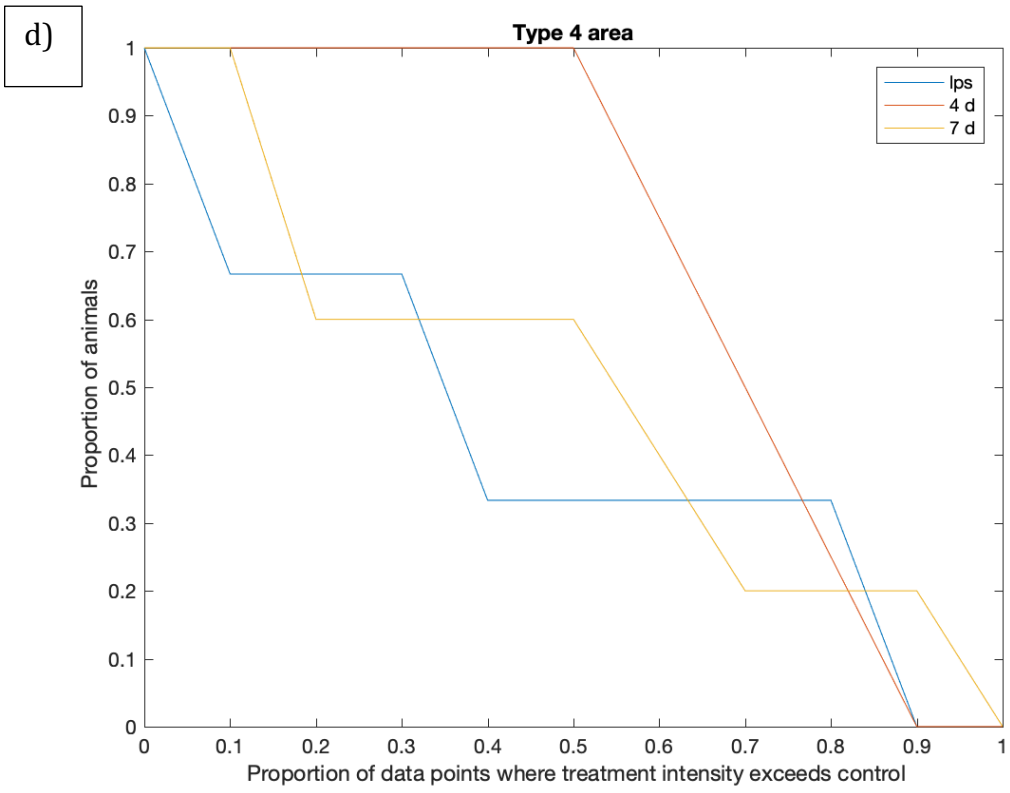

Figure 5-7 - The proportion of animals (y axis) in which fluorescence intensity of the treated ear exceeded that of the control ear by proportional criteria of 0.1-1 (y axis). Each line is data from a

different experimental group (LPS, 4- or -7 day post cochlear implantation). Each subplot is data from a different ROI (a-d: bone, limbus, Type 2 and Type 4 fibrocyte area).

5.4 Discussion

TSLIM acts as a 'non-destructive microtome' (Santi, 2011), allowing non-destructive optical sectioning of complex structures. Our TSLIM processes have been utilised for anatomical investigations(Lo, J, et al, 2017) of surgical technique as well as investigation of drug effects (Lo, Campbell, et al., 2017a), with further applications being currently explored. The use of TSLIM was in this experiment enhanced by addition of fluorescent probes that add physiological information to the anatomical information available using conventional TSLIM.

Quantitative analysis of changes in Evans Blue extravasation is made more difficult by the imperfect generation of a light sheet. The intensity of illumination at any point in the sheet varies because of a number of factors, including, but limited to: the inverse-square law as it pertains to any light source, fall-off across the specimens as photons interact with the specimen and the relationship between the specimen position and the confocal portion of the light sheet. The use of two light sheets aimed to obviate some of these issues, but introduced its own complications in accurate alignment of the two confocal regions.

A further issue identified during this experiment was the formation of microscopic bubbles within the Spalteholz Fluid carrier, which generated artefact particularly in unfiltered acquisitions. These bubbles enlarged with time

after specimen processing, reducing the quality of unfiltered acquisitions if the specimen was imaged more than a few days after processing. 640nm filtered acquisitions appeared much less susceptible to this process.

Evans Blue extravasation appears to be increased 4 days after cochlear implant surgery at a number of locations, particularly around the position of the tip of the electrode (Figure 5-5). These changes appear to normalise at the later timepoint (Figure 5-6). The plots of signal intensity for Type 2 and Type 4 fibrocyte regions at Day 4 appear very similar, with increased signal concentrated around the region of the cochleostomy and then distal to the predicted position of the electrode tip (Smeds et al., 2015).

The LPS data gave unexpected results, where although a significant Friedman statistic was obtained, the plots of signal intensity suggest a lower fluorescence in the ears that received intratympanic lipopolysaccharide. Generation of a florid inflammatory response to the intratympanic LPS may have been hampered by the use of a lower concentration of LPS used when compared to other animal hydrops experiments (Floc'h et al., 2013; J. Zhang et al., 2015).

Inconsistencies in tissue clearing and staining saw several animals excluded as outliers. Noise in the dataset appeared to disproportionately affect the LPS group, where large spikes in the data were associated with a significant Friedman statistic. Little difference between ears is evident on the plots at other areas, which raises the possibility that the Friedman Test has been affected by the quality of data from a small number of animals.

5.5 Conclusion

Qualitative and quantitative changes in vascular permeability to Evans Blue were demonstrable in an intact cochlea using TSLIM. This represents the first application of exogenous fluorescent dyes to add physiological information to the detailed anatomical information that has been demonstrated in the past. Careful attention to normalisation of fluorescence data was important to avoid interpreting changes in light sheet intensity across the specimen as changes in Evans Blue extravasation.

Significant changes in cochlear vascular permeability to Evans Blue were noted after cochlear implantation. These changes were most marked 4 days after electrode insertion, with no increased fluorescence present by Day 7.

6 Discussion

This thesis details our efforts to expand available modalities and capabilities of non-destructive evaluation of the cochlear response to injury.

With regards to OCT, this technique is widely utilised in ophthalmological practice, but has more recently evolved into a tool in hearing research. The excellent temporal resolution available with OCT has seen it utilised for real-time visualisation of basilar membrane vibrations in response to auditory stimuli, but ours is the first published use of OCT for evaluation of Reissner's membrane morphology and round window membrane thickness. Both these measures have helped us in our understanding of why our therapeutic approach could have caused an unexpected deterioration in hearing thresholds amongst our experimental animals. One of the articular barriers to application of OCT in the cochlea is bone, with the resulting compromise between imaging parameters; particularly depth of field (DOF) and the intactness of the specimen. We chose to perform OCT measurements in tissues that had already been decalcified, similar to other groups (Cho et al., 2015; Kakigi et al., 2013), which allowed us reasonable penetration of infrared light and resulting depth of field, but is a notable departure from the state of the tissue in life. Other authors have chosen to eliminate calcified bone scatter through surgical thinning, fenestration or complete removal (Gao et al., 2011; Iyer et al., 2016; Mohebbi et al., 2017; Sepehr et al., 2008), which limits the utility of observations due to either a lack of repeatability or the possibility of inducing hearing loss through powered bone removal techniques. True *in vivo* techniques have been limited to murine cochleae, with imaging across the intact, but relatively thin bone of the cochlear apex (G. S. Liu, Kim, Applegate, & Oghalai, 2017a; G. S. Liu et al., 2017b). Our

group utilised OCT to measure changes in round window membrane thickness after continuous drug delivery, while others utilise the RWM as an OCT-portal to the structures of the cochlear hook. It is this technique that currently displays most promise in clinical applicability of OCT to the human cochlea in vivo. The reliable measures of basilar membrane displacement seen in rodents earlier in OCT's application to the inner ear (Jawadi, Applegate, & Oghalai, 2016; N. C. Lin, Fallah, Strimbu, Hendon, & Olson, 2019) are now possible using endoscope mounted probes placed in at least the porcine round window niche (W. Kim, Kim, Oghalai, & Applegate, 2018). Our application of a commercially available retinal imaging device to inner ear imaging introduces some of its own issues, particularly with regards to measurements in different axes. The pixels generated by our 2D scanner were not isotropic, with consistent thickness measurements only possible if the imaging plane was repeated exactly. Newer scanners allow isotropic datasets, often with some downsampling required during processing. Adding additional optical elements into the imaging path as in our apparatus also has the potential for introduction of optical distortion to the acquired dataset.

μCT, while more typically utilised in materials sciences, is well established in the hearing research sector as a valuable tool for descriptive microanatomical research. Our work has expanded the utility of μCT in hearing research by adding a functional slant. Non-destructive visualisation of cochlear endolymphatic hydrops adds support for the existence of the entity of post-implantation hydrops as described previously on conventional histology. Continuous data also reveals that these hydropic changes are not necessarily

global. μCT has also allowed us to evaluate, in detail, the position, volume and relationships of the tissue response to implantation. This makes osmium-enhanced μCT a viable option in the trials of therapeutic measures designed to modulate the tissue response to implantation. Furthermore, we are now able to eliminate tissue processing as a source of false intracochlear trauma, such as OSL fractures. As obtainable spatial resolutions in μCT have improved with time and technological advance, so have those in clinical CT apparatus. Flat panel detector clinical CT has evolved steadily, with c-arm angiographic systems able to produce datasets with 140μm side length voxels. While this spatial resolution is coarse when compared to the submicron resolution available in commercial μCT equipment, this represents an improvement on available clinical multi-slice systems in terms of voxel dimension. Susceptibility to beam-hardening artefact and some degradation in soft tissue contrast is evident due to the use of lower energy photons in flat panel systems. The difference in acquisition pattern also leads to different effective doses between the two techniques. Flat-panel systems delivery demonstrably less radiation to the eyes and lens(Kennedy et al., 2016), where multi-slice helical acquisitions relatively spare the pituitary. The higher dose at the pituitary in an intact head can be explained by its location at the radiation isocentre of the arc-shaped acquisition pattern (Piergallini et al., 2018). Radiation doses absorbed during small animal μCT are several magnitudes higher than either clinical technique, which raises concerns for the repeated imaging of small animals in a research context as well as clinical utility. Both multi-slice helical techniques and flat-panel acquisitions today delivery doses of approximately 1mSv (Piergallini et al., 2018). Bone absorbed doses in small animals will differ according to scanning parameters, but are often in the

order of 10cGy (Johnstone & Bazalova-Carter, 2018) (or 100mSv, equivalent to 50 years of background radiation exposure) per acquisition volume. The difference in acquisition duration is even more stark, with μCT acquisitions measured in hours depending on the exposure time and number of tomographic projections acquired.

TSLIM is a further modality that allows us to generate volumetric datasets in a non-destructive manner. Both are ex-vivo techniques, but TSLIM opens up new possibilities in adding the LASER fluorophore localisation techniques utilised in LSCM to a larger and intact tissue volume. TSLIM techniques could be utilised in re-examination of the issues raised in Experiment 1, where antibodies to myosin VIIa were utilised to identify intact hair cell stereocilia via immunofluorescence and LSCM. This change in technique could obviate the need for dissection of the cochlear duct from the bony cochlea, with improvements in intact yield predictable, empirically. This increased specimen yield could be expected to be particularly significant in regions of the cochlea where whole-mount specimens are most difficult to dissect, such as the hook region of the basal turn of the cochlea. A combination of sterocilia immunofluorescence and filtering of the fluorescent output would generate a highly specific dataset with the possibility of whole organ hair cell counts and even automated counting in high quality datasets.

One caveat when considering TSLIM for quantitative purposes such as hair cell counts is the issue of data continuity. TSLIM, unlike μCT acquired using a flat panel detector, is not necessarily a continuous dataset. The degree of continuity will be determined by the interval between acquired slices *z*, as well as the

optical properties of the generated light sheet and the position of the structure of interest with respect to the confocal region of the light sheet. The light sheet used to optically section the specimen is thin, but not perfectly planar. The sheet is hyperbolic in dimension (Weber & Huisken, 2011), such that the end of the sheet adjacent either projecting objective is much thicker than the beam waist where the two light sheets intersect. The thickness of the optical section thus varies in the *z* dimension depending on position between the projecting objectives. The portion of the optical slice illuminated by the light sheets in their confocal region is more intensely illuminated and has better spatial resolution, but the thickness of the beam waist means that slicing intervals have to be reduced to obtain anything resembling a continuous dataset.

Discontinuous data has the potential to introduce inconsistencies in procedures such as hair cell counts via stereocilia immunofluorescence because the structures to be counted are approaching the spatial resolution of the imaging technique and are oriented in the plane of the light sheet in all but the cochlear hook. Sterocilia could foreseeably fall between optical slices if they are in the region of the beam waist and the dimension of the beam waist is substantially less than the slice interval. This problem could be reduced by changing mounting techniques so that basal plane of the cochlea (Verbist et al., 2010) is coaxial with the light sheet, but may introduce some degradation of counting in the hook region as the axis of the basilar membrane turns approximately 90 degrees as it turns over the round window membrane.

Widespread tissue autofluorescence, typically in response to green-yellow LASERs of approximately 532nm wavelength allows the anatomical imaging

possible with TSLIM (Lo, Sale, et al., 2017b), with authors using this anatomical information to examine cell density in cochlear compartments or identify hair cell loss (Schmitz, Johnson, & Santi, 2014). Application of techniques more historically seen in LSCM broadens the application of TSLIM to three-dimensional evaluation of normal and deranged physiology. The third experiment in this thesis uses the fluorescent properties of a heavily albumin-bound tracer to identify changes in vascular permeability to albumin, but more complex immunofluorescence protocols are also being applied to TSLIM. Early work by our group, currently in press, sees immunofluorescence used to localise glucocorticoid receptor (GR) expression throughout the cochlea. Similar immunofluorescence techniques could see three-dimensional assessment of ribbon synapse density evaluated across a whole cochlea after noise trauma or evaluation of cochlea-wide gene-product expression after different methods of introduction of gene therapies. The major advantage being the ability to provide location- and thus frequency-specific information in hearing sciences and to do so in a non-destructive manner. Our group is in the process of expanding fluorophores and beamlines utilised to allow true three-dimensional assessment of cochlear pathophysiology in animal models and we expect rapid uptake of these techniques by other researchers once the capabilities of these techniques become widely known.

High resolution whole-cochlear imaging in humans is a highly sought-after process, but at this time begets further qualification: ex-vivo or in-vivo. In-vivo imaging relies on ever-improving clinical imaging techniques, which will be limited by human anatomical characteristics, radiation safety and duration of

scan. The only technique used in this thesis that has potential application to the human cochlea in-vivo is OCT, applied endoscopically through an intact Round Window Membrane. Ex-vivo imaging of the human cochlea expands the possibilities significantly, with all of the utilised techniques similarly applicable to the human otic capsule with modifications in specimen preparation and imaging parameters.

Each of the techniques studies has inherent advantages and disadvantages, but all have a niche in cochlear imaging in which they excel. Picking the right tool for the job at hand is a major consideration when considering non-destructive imaging techniques for evaluation of cochlear anatomy, physiology and pathology.

7 Appendix

7.1 Non Local Means Filtering

Image denoising algorithms have traditionally relied on systematic, but isolated examination of the pixel region immediately surrounding an area of noise. The result being that fine details and textures are treated as noise and thus suppressed in the resulting, denoised image.

A recently developed method of denoising extends consideration to larger portions, or even the whole image, when denoising. The Non Local Means (NLM) methods (Buades A, et al, 2005) still utilise averaging of other pixels(q_x) within an image to denoise a given pixel(j), but the contribution of these other pixels to the average is weighted according to the similarity of the neighbourhood surrounding the pixel (q_x) to the neighbourhood surrounding (j). This is particularly useful when denoising images containing repeated, periodic patterns or textures.

Figure 7-1 - When denoising pixel p, pixels q1 and q2 will be given greater weight than q3 because their neighbourhoods are more similar to the neighbourhood surrounding p. Adapted from Buades, et al (Buades, Morel, & Coll, 2005).

Although μCT images of cochleae do not contain periodic textures, if one considers a pixel from a section through a thin structure such as Reissner's Membrane, the similarity of the neighbourhoods surrounding other pixels along Reissner's Membrane will provide weighting which will help preserve this structure in the denoised image. Fine structure preservation has thus become a significant driver for integration of NLM techniques into medical imaging (Dutta J, et al, 2013) and imaging-based research (Chen KC, et al, 2018)

Depending on the dimensions of the neighbourhood utilised for each (q_x) and the dimensions of the search window around (j) for which (q_x) will be considered, this process can be very computationally intensive because of the large number of weightings calculated for each pixel to be denoised. Amira's implementation of NLM denoising delegates this large number of relatively simple, repeated calculations to a General-Purpose Computing on Graphics Processing Units (GPGPU) capable graphic card, whose large number of processing units ('cores') (generally greater than 1000) allow simultaneous performance of simple tasks at a much higher rate than a computers Central Processing Unit (CPU), which contains smaller numbers of more versatile cores.

8 References

Abraham, C. S., Deli, M. A., Joo, F., Megyeri, P., & Torpier, G. (1996). Intracarotid tumor necrosis factor-alpha administration increases the blood-brain barrier permeability in cerebral cortex of the newborn pig: quantitative aspects of double-labelling studies and confocal laser scanning analysis. *Neuroscience Letters*, *208*(2), 85–88.

Agterberg, M. J. H., Versnel, H., van Dijk, L. M., de Groot, J. C. M. J., & Klis, S. F. L. (2009). Enhanced Survival of Spiral Ganglion Cells After Cessation of Treatment with Brain-Derived Neurotrophic Factor in Deafened Guinea Pigs. *Journal of the Association for Research in Otolaryngology*, *10*(3), 355–367. http://doi.org/10.1007/s10162-009-0170-2

Albers, F. W., De Groot, J. C., Veldman, J. E., & Huizing, E. H. (1988). Ultrastructure of the organ of Corti in experimental hydrops. *Acta Oto-Laryngologica*, *105*(3-4), 281–291.

Anniko, M., & Lundquist, P. G. (1977). The influence of different fixatives and osmolality on the ultrastructure of the cochlear neuroepithelium. *Archives of Otorhinolaryngology*, *218*(1-2), 67–78. http://doi.org/10.1007/BF00469735

Bachor, E., & Karmody, C. S. (1995). Endolymphatic hydrops in children. *ORL; Journal for Oto-Rhino-Laryngology and Its Related Specialties*, *57*(3), 129–134. http://doi.org/10.1159/000276725

Bánfi, B., Malgrange, B., Knisz, J., Steger, K., Dubois-Dauphin, M., & Krause, K.-H. (2004). NOX3, a Superoxide-generating NADPH Oxidase of the Inner Ear. *Journal of Biological Chemistry*, *279*(44), 46065–46072. http://doi.org/10.1074/jbc.M403046200

Becker, K., Jährling, N., Saghafi, S., & Dodt, H.-U. (2013). Ultramicroscopy: Light-Sheet-Based Microscopy for Imaging Centimeter-Sized Objects with Micrometer Resolution. *Cold Spring Harbor Protocols*, *2013*(8), pdb.top076539–11. http://doi.org/10.1101/pdb.top076539

Bedard, K., & Krause, K.-H. (2007). The NOX Family of ROS-Generating NADPH Oxidases: Physiology and Pathophysiology. *Physiological Reviews*, *87*(1), 245–313. http://doi.org/10.1152/physrev.00044.2005

Beister, M., Kolditz, D., & Kalender, W. A. (2012). Iterative reconstruction methods in X-ray CT. *Physica Medica*, *28*(2), 94–108. http://doi.org/10.1016/j.ejmp.2012.01.003

Belal, A., & Antunez, J. C. (1980). Pathology of endolymphatic hydrops. *The Journal of Laryngology and Otology, 94*, 1231-1240.

Belden, C. J., Weg, N., Minor, L. B., & Zinreich, S. J. (2003). CT evaluation of bone dehiscence of the superior semicircular canal as a cause of sound- and/or pressure-induced vertigo. *Radiology*, *226*(2), 337–343. http://doi.org/10.1148/radiol.2262010897

Boas, F. E., & Fleischmann, D. (2012). CT artifacts: causes and reduction techniques. *Imaging in Medicine*, *4*(2), 229–240. http://doi.org/10.2217/iim.12.13

Bobbin, R. P., Jastreboff, P. J., Fallon, M., & Littman, T. (1990). Nimodipine, an L-channel Ca2+ antagonist, reverses the negative summating potential recorded from the guinea pig cochlea. *Hearing Research*, *46*(3), 277–287.

Bohne, B. A., & Harding, G. W. (1997). Processing and analyzing the mouse temporal bone to identify gross, cellular and subcellular pathology. *Hearing Research*, *109*(1-2), 34–45.

Böttger, E. C., & Schacht, J. (2013). The mitochondrion: A perpetrator of acquired hearing loss. *Hearing Research*, *303*(C), 12–19. http://doi.org/10.1016/j.heares.2013.01.006

Brown, D. J., Chihara, Y., & Wang, Y. (2013). Changes in utricular function during artificial endolymph injections in guinea pigs. *Hearing Research*, *304*(C), 70–76. http://doi.org/10.1016/j.heares.2013.05.011

Brunschwig, A. S., & Salt, A. N. (1997). Fixation-induced shrinkage of Reissner's membrane and its potential influence on the assessment of endolymph volume. *Hearing Research*, *114*(1-2), 62–68.

Buades, A., Morel, J. M., & Coll, B. (2005). A non-local algorithm for image denoising, 1–6.

Burghard, A., Lenarz, T., Kral, A., & Paasche, G. (2014). Insertion site and sealing technique affect residual hearing and tissue formation after cochlear implantation. *Hearing Research*, *312*(C), 21–27. http://doi.org/10.1016/j.heares.2014.02.002

Buytaert, J. A. N., Johnson, S. B., Dierick, M., Salih, W. H. M., & Santi, P. A. (2013). MicroCT versus sTSLIM 3D Imaging of the Mouse Cochlea. *Journal of Histochemistry & Cytochemistry*, *61*(5), 382–395. http://doi.org/10.1369/0022155413478613

Canlon, B., Meltser, I., Johansson, P., & Tahera, Y. (2007). Glucocorticoid receptors modulate auditory sensitivity to acoustic trauma. *Hearing Research*, *226*(1-2), 61–69. http://doi.org/10.1016/j.heares.2006.05.009

Cayé Thomasen, P., Wagner, N., Engmér, C., Laurell, G., Bagger-Sjöbäck, D., & Thomsen, J. (2009). An animal model for continuous drug administration to the inner ear. *Audiological Medicine*, *2*(3), 174–178. http://doi.org/10.1080/16513860410018006

Cheng, P. M., Romero, M., & Duddalwar, V. A. (2014). Pulmonary pseudoemboli: a new artifact arising from a commercial metal artifact reduction algorithm for computed tomographic image reconstruction. *Journal of Computer Assisted Tomography*, *38*(2), 159–162. http://doi.org/10.1097/RCT.0b013e3182aac5de

Cho, N. H., Lee, J. W., Cho, J.-H., Kim, J., Jang, J. H., & Jung, W. (2015). Evaluation of the usefulness of three-dimensional optical coherence tomography in a guinea pig model of endolymphatic hydrops induced by surgical obliteration of the endolymphatic duct. *Journal of Biomedical Optics*, *20*(3), 036009. http://doi.org/10.1117/1.JBO.20.3.036009

Choi, Cheol Hee, Jang, C. H., Cho, Y. B., Jo, S. Y., Kim, M. Y., & Park, B. Y. (2012). Matrix metalloproteinase inhibitor attenuates cochlear lateral wall damage induced by intratympanic instillation of endotoxin. *International Journal of Pediatric Otorhinolaryngology*, *76*(4), 544–548. http://doi.org/10.1016/j.ijporl.2012.01.013

Choi, Chul-Hee, & Oghalai, J. S. (2005). Predicting the effect of post-implant cochlear fibrosis on residual hearing. *Hearing Research*, *205*(1-2), 193–200. http://doi.org/10.1016/j.heares.2005.03.018

Choudhury, N., Zeng, Y., Fridberger, A., Chen, F., Zha, D., Nuttall, A. L., & Wang, R. K. (2011). Imaging vibration of the cochlear partition of an excised guinea pig cochlea using phase-sensitive Fourier domain optical coherence tomography. In J. G. Fujimoto, J. A. Izatt, & V. V. Tuchin (Eds.), (Vol. 7889, pp. 788930–4). Presented at the SPIE BiOS, SPIE. http://doi.org/10.1117/12.875534

Ciuman, R. R. (2008). Stria vascularis and vestibular dark cells: characterisation of main structures responsible for inner-ear homeostasis, and their pathophysiological relations. *The Journal of Laryngology & Otology*, *123*(02), 151–12. http://doi.org/10.1017/S0022215108002624

Cohen-Salmon, M., Regnault, B., Cayet, N., Caille, D., Demuth, K., Hardelin, J.-P., et al. (2007). Connexin30 deficiency causes instrastrial fluid-blood barrier disruption within the cochlear stria vascularis. *Proceedings of the National Academy of Sciences of the United States of America*, *104*(15), 6229–6234. http://doi.org/10.1073/pnas.0605108104

Conlon, B. J. (2000). Electrocochleography in the Diagnosis of Meniere's Disease. *Acta Oto-Laryngologica*, *120*(4), 480–483. http://doi.org/10.1080/000164800750045965

Connolly, T. M., Eastwood, H., Kel, G., Lisnichuk, H., Richardson, R., & O'Leary, S. (2011). Pre-Operative Intravenous Dexamethasone Prevents Auditory Threshold Shift in a Guinea Pig Model of Cochlear Implantation. *Audiology and Neurotology*, *16*(3), 137–144. http://doi.org/10.1159/000314757

Cook-Mills, J. M. (2006). Hydrogen peroxide activation of endothelial cell-associated MMPs during VCAM-1-dependent leukocyte migration. *Cellular and Molecular Biology (Noisy-Le-Grand, France)*, *52*(4), 8–16.

Cunningham, L. L., & Tucci, D. L. (2015). Restoring Synaptic Connections in the Inner Ear after Noise Damage. *New England Journal of Medicine*, *372*(2), 181–182. http://doi.org/10.1056/NEJMcibr1413201

Curthoys, I. S., Uzun-Coruhlu, H., Wong, C. C., Jones, A. S., & Bradshaw, A. P. (2009). The configuration and attachment of the utricular and saccular maculae to the temporal bone. New evidence from microtomography-CT studies of the membranous labyrinth. *Annals of the New York Academy of Sciences*, *1164*(1), 13–18. http://doi.org/10.1111/j.1749-6632.2008.03729.x

Dai, C. F., & Steyger, P. S. (2008). A systemic gentamicin pathway across the stria vascularis. *Hearing Research*, *235*(1-2), 114–124. http://doi.org/10.1016/j.heares.2007.10.010

Davis, R. L. (2016). Gradients of Neurotrophins, Ion Channels, and Tuning in the Cochlea. *The Neuroscientist*, *9*(5), 311–316. http://doi.org/10.1177/1073858403251986

DeCicco, M., Hoffer, M., Kopke, R., Wester, D., Allen, K., Gottshall, K., & O'Leary, M. (1998). Round-Window Microcatheter-Administered Microdose Gentamicin: Results from Treatment of Tinnitus Associated with Menière's Disease. *The International Tinnitus Journal*, *4*(2), 141–143.

Donnelly, N., Bibas, A., Jiang, D., Bamiou, D.-E., Santulli, C., Jeronimidis, G., & Fitzgerald-O'Connor, A. (2009). Effect of cochlear implant electrode insertion on middle-ear function as measured by intra-operative laser Doppler vibrometry. *The Journal of Laryngology & Otology*, *123*(07), 723–8. http://doi.org/10.1017/S0022215109004290

Dunnebier, E. A., Segenhout, J. M., Wit, H. P., & Albers, F. W. (1997). Two-phase endolymphatic hydrops: a new dynamic guinea pig model. *Acta Oto-Laryngologica*, *117*(1), 13–19.

Egami, N., Kakigi, A., Sakamoto, T., Takeda, T., Hyodo, M., & Yamasoba, T. (2013). Morphological and functional changes in a new animal model of Ménière’s disease. *Laboratory Investigation*, *93*(9), 1001–1011. http://doi.org/10.1038/labinvest.2013.91

Endo, T., Nakagawa, T., Kita, T., Iguchi, F., Kim, T.-S., Tamura, T., et al. (2005). Novel strategy for treatment of inner ears using a biodegradable gel. *The Laryngoscope*, *115*(11), 2016–2020. http://doi.org/10.1097/01.mlg.0000183020.32435.59

Engmér, C., Laurell, G., Bagger-Sjöbäck, D., & Rask-Andersen, H. (2008). Immunodefense of the Round Window. *The Laryngoscope*, *118*(6), 1057–1062. http://doi.org/10.1097/MLG.0b013e31816b30b0

Engstrom, B., Hillerdal, M., & Hillerdal, G. (1990). Preservation of the human cochlea with two different fixatives. *Acta Oto-Laryngologica. Supplementum*, *470*, 31–33.

Eshraghi, A. A., Polak, M., He, J., Telischi, F. F., Balkany, T. J., & Van De Water, T. R. (2005). Pattern of hearing loss in a rat model of cochlear implantation trauma. *Otology & Neurotology*, *26*(3), 442–7– discussion 447.

Farhadi, M., Jalessi, M., Salehian, P., Ghavi, F. F., Emamjomeh, H., Mirzadeh, H., et al. (2013). Dexamethasone eluting cochlear implant: Histological study in animal model. *Cochlear Implants International*, *14*(1), 45–50. http://doi.org/10.1179/1754762811Y.0000000024

Fetoni, A. R., Ralli, M., Sergi, B., & Parrilla, C. (2009). Protective effects of N-acetylcysteine on noise-induced hearing loss in guinea pigs. *Acta Otorhinolaryngologica Italia, 29(*2), 70-75.

Floc'h, J. L., Tan, W., Telang, R. S., Vlajkovic, S. M., Nuttall, A., Rooney, W. D., et al. (2013). Markers of cochlear inflammation using MRI. *Journal of Magnetic Resonance Imaging*, *39*(1), 150–161. http://doi.org/10.1002/jmri.24144

Fukuoka, H., Tsukada, K., Miyagawa, M., Oguchi, T., Takumi, Y., Sugiura, M., et al. (2010). Semi-quantitative evaluation of endolymphatic hydrops by bilateral intratympanic gadolinium-based contrast agent (GBCA) administration with MRI for Meniere's disease. *Acta Oto-Laryngologica*, *130*(1), 10–16. http://doi.org/10.3109/00016480902858881

Gao, S. S., Xia, A., Yuan, T., Raphael, P. D., Shelton, R. L., Applegate, B. E., & Oghalai, J. S. (2011). Quantitative imaging of cochlear soft tissues in wild-type and hearing-impaired transgenic mice by spectral domain optical coherence tomography. *Optics Express*, *19*(16), 15415–15428. http://doi.org/10.1364/OE.19.015415

Gibson, W. P. R. (2009). A comparison of two methods of using transtympanic electrocochleography for the diagnosis of Meniere's disease: click summating potential/action potential ratio measurements and tone burst summating potential measurements. *Acta Oto-Laryngologica*, *129*(sup560), 38–42. http://doi.org/10.1080/00016480902729843

Gillespie, L. N., Clark, G. M., Bartlett, P. F., & Marzella, P. L. (2003). BDNF-induced survival of auditory neurons in vivo: Cessation of treatment leads to accelerated loss of survival effects. *Journal of Neuroscience Research*, *71*(6), 785–790. http://doi.org/10.1002/jnr.10542

Goycoolea, M. V., & Lundman, L. (1997). Round window membrane. Structure function and permeability: a review. *Microscopy Research and Technique*, *36*(3), 201–211. http://doi.org/10.1002/(SICI)1097-0029(19970201)36:3<201::AID-JEMT8>3.0.CO;2-R

Greenwood, D. D. (1990). A cochlear frequency-position function for several species--29 years later. *The Journal of the Acoustical Society of America*, *87*(6), 2592–2605. http://doi.org/10.1121/1.399052

Handzel, O., Burgess, B. J., & Nadol, J. B. J. (2006). Histopathology of the peripheral vestibular system after cochlear implantation in the human. *Otology & Neurotology*, *27*(1), 57–64.

Hellström, S., Johansson, U., & Anniko, M. (1988). Structure of the Round Window Membrane. *Acta Oto-Laryngologica*, *105*(5 supp 457), 33–42. http://doi.org/10.3109/00016488809138882

Hirose, K., Discolo, C. M., Keasler, J. R., & Ransohoff, R. (2005). Mononuclear phagocytes migrate into the murine cochlea after acoustic trauma. *The Journal of Comparative Neurology*, *489*(2), 180–194. http://doi.org/10.1002/cne.20619

Honda, K., Noguchi, Y., Kawashima, Y., Takahashi, M., Nishio, A., & Kitamura, K. (2015). Ex vivo visualization of the mouse otoconial layer compared with micro-computed tomography. *Otology & Neurotology*, *36*(2), 311–317. http://doi.org/10.1097/MAO.0000000000000376

Hong, S. H., Park, S. K., Cho, Y.-S., Lee, H.-S., Kim, K. R., Kim, M. G., & Chung, W.-H. (2006). Gentamicin induced nitric oxide-related oxidative damages on vestibular afferents in the guinea pig. *Hearing Research*, *211*(1-2), 46–53. http://doi.org/10.1016/j.heares.2005.08.009

Horner, K. C., Guilhaume, A., & Cazals, Y. (1988). Atrophy of middle and short stereocilia on outer hair cells of guinea pig cochleas with experimentally induced hydrops. *Hearing Research*, *32*(1), 41–48.

Hornibrook, J., & Bird, P. (2017). A New Theory for Ménière's Disease: Detached Saccular Otoconia. *Otolaryngology--Head and Neck Surgery*, *156*(2), 350–352. http://doi.org/10.1177/0194599816675843

Huang, D., Swanson, E. A., Lin, C. P., Schuman, J. S., Stinson, W. G., Chang, W., et al. (1991). Optical coherence tomography. *Science (New York, N.Y.)*, *254*(5035), 1178–1181.

Huber, A. M., Hoon, S. J., Sharouz, B., Daniel, B., & Albrecht, E. (2010). The Influence of a Cochlear Implant Electrode on the Mechanical Function of the Inner Ear. *Otology & Neurotology*, *31*(3), 512–518. http://doi.org/10.1097/MAO.0b013e3181ca372b

Hukee, M. J., & Duvall, A. J. (1985). Cochlear vessel permeability to horseradish peroxidase in the normal and acoustically traumatized chinchilla: a reevaluation. *Ann Otol Rhinol Laryngol*, *94*(3), 297–303.

Iida, T., Teranishi, M., Yoshida, T., Otake, H., Sone, M., Kato, M., et al. (2013). Magnetic resonance imaging of the inner ear after both intratympanic and intravenous gadolinium injections. *Acta Oto-Laryngologica*, *133*(5), 434–438. http://doi.org/10.3109/00016489.2012.753640

Ikeda, K., Morizono, T., & Takasaka, T. (1991). Otic preparations altered permeability and thickness of the round window membrane of the chinchilla. *ORL; Journal for Oto-Rhino-Laryngology and Its Related Specialties*, *53*(2), 91–93. http://doi.org/10.1159/000276195

Ishiyama, A., Doherty, J., Ishiyama, G., Quesnel, A. M., Lopez, I., & Linthicum, F. H. (2016). Post Hybrid Cochlear Implant Hearing Loss and Endolymphatic Hydrops. *Otology & Neurotology*, *37*(10), 1516–1521. http://doi.org/10.1097/MAO.0000000000001199

Iyer, J. S., Batts, S. A., Chu, K. K., Sahin, M. I., Leung, H. M., Tearney, G. J., & Stankovic, K. M. (2016). Micro-optical coherence tomography of the mammalian cochlea. *Scientific Reports*, *6*(1), 33288–10. http://doi.org/10.1038/srep33288

James, D. P., Eastwood, H., Richardson, R. T., & O'Leary, S. J. (2008). Effects of Round Window Dexamethasone on Residual Hearing in a Guinea Pig Model of Cochlear Implantation. *Audiology and Neurotology*, *13*(2), 86–96. http://doi.org/10.1159/000111780

Jang, C. H., Cho, Y. B., Kim, J. S., Cho, S. W., Yang, H. C., Jung, K. H., et al. (2011). Effect of Ginkgo biloba extract on endotoxin-induced labyrinthitis. *International Journal of Pediatric Otorhinolaryngology*, *75*(7), 905–909. http://doi.org/10.1016/j.ijporl.2011.04.003

Jawadi, Z., Applegate, B. E., & Oghalai, J. S. (2016). Optical Coherence Tomography to Measure Sound-Induced Motions Within the Mouse Organ of Corti In Vivo. *Methods in Molecular Biology*, *1427*, 449–462. http://doi.org/10.1007/978-1-4939-3615-1_24

Jenison, G. L., Bobbin, R. P., & Thalmann, R. (1985). Potassium-induced release of endogenous amino acids in the guinea pig cochlea. *Journal of Neurochemistry*, *44*(6), 1845–1853.

Jia, X.-H., Liang, Q., Chi, Z.-C., Dai, P.-D., Zhang, T.-Y., & Wang, T.-F. (2012). [Morphological changes associated with low-tone hearing loss in guinea pig models of early endolymphatic hydrops]. *Sheng Li Xue Bao : [Acta Physiologica Sinica]*, *64*(1), 48–54.

Johnstone, C. D., & Bazalova-Carter, M. (2018). MicroCT imaging dose to mouse organs using a validated Monte Carlo model of the small animal radiation research platform (SARRP). *Physics in Medicine and Biology*, *63*(11), 115012. http://doi.org/10.1088/1361-6560/aac335

Juhn, S. K., Kim, B.-H., Schachern, P., Tsuprun, V., & Adams, G. L. (2016). The Effects of Bacterial Endotoxin on Cochlear Function and the Blood Labyrinth Barrier. *Otolaryngology -- Head and Neck Surgery*, *131*(2), P145–P145. http://doi.org/10.1016/j.otohns.2004.06.237

Kakigi, A., Takubo, Y., Egami, N., Kashio, A., Ushio, M., Sakamoto, T., et al. (2013). Evaluation of the Internal Structure of Normal and Pathological Guinea Pig Cochleae Using Optical Coherence Tomography. *Audiology and Neurotology*, *18*(5), 335–343. http://doi.org/10.1159/000354620

Karnovsky, M. J. (1965). A formaldehyde-glutaraldehyde fixative of high osmolality for use in electron microscopy. *The Journal of Cell Biology*, *27*(1), 137A–138A.

Kel, G. E., Tan, J., Eastwood, H. T., Wongprasartsuk, S., & O'Leary, S. J. (2013). Early cochlear response and ICAM-1 expression to cochlear implantation. *Otology & Neurotology*, *34*(9), 1595–1602. http://doi.org/10.1097/MAO.0b013e31828f4929

Kennedy, T. A., Connell, N., Szczykutowicz, T., Schafer, S., Royalty, K., Nace, S., et al. (2016). Flat-Panel CT for Cochlear Implant Electrode Imaging. *Otology & Neurotology*, *37*(10), 1646–1653. http://doi.org/10.1097/MAO.0000000000001216

Kiefer, J., Böhnke, F., Adunka, O., & Arnold, W. (2006). Representation of acoustic signals in the human cochlea in presence of a cochlear implant electrode. *Hearing Research*, *221*(1-2), 36–43. http://doi.org/10.1016/j.heares.2006.07.013

Kim, W., Kim, S., Oghalai, J. S., & Applegate, B. E. (2018). Endoscopic optical coherence tomography enables morphological and subnanometer vibratory imaging of the porcine cochlea through the round window. *Optics Letters*, *43*(9), 1966–1969. http://doi.org/10.1364/OL.43.001966

Kimura, R. S., Schuknecht, H. F. (1970). The ultrastructure of the human stria vascularis. Part I. *Acta Oto-Laryngologica 69*(1-6), 415-427.

Kimura, R. S., Schuknecht, H. F., Ota, C. Y., & Jones, D. D. (1980). Obliteration of the ductus reuniens. *Acta Oto-Laryngologica*, *89*(3-4), 295–309. http://doi.org/10.3109/00016488009127141

King, E. B., Salt, A. N., Kel, G. E., Eastwood, H. T., & O'Leary, S. J. (2013). Gentamicin administration on the stapes footplate causes greater hearing loss and vestibulotoxicity than round window administration in guinea pigs.

Hearing Research, *304*(C), 159–166. http://doi.org/10.1016/j.heares.2013.07.013

Konishi, S. (1977). The ductus reuniens and utriculo-endolymphatic valve in the presence of endolymphatic hydrops in guinea-pigs. *The Journal of Laryngology & Otology*, *91*(12), 1033–1045.

Kopecky, B., Santi, P., Johnson, S., Schmitz, H., & Fritzsch, B. (2011). Conditional deletion of N-Myc disrupts neurosensory and non-sensory development of the ear. *Developmental Dynamics*, *240*(6), 1373–1390. http://doi.org/10.1002/dvdy.22620

Kruse, H., & McMaster, P. D. (1949). The distribution and storage of blue antigenic azoproteins in the tissues of mice. *The Journal of Experimental Medicine*, *90*(5), 425–446. http://doi.org/10.1084/jem.90.5.425

Landry, T. G., Wise, A. K., Fallon, J. B., & Shepherd, R. K. (2011). Spiral ganglion neuron survival and function in the deafened cochlea following chronic neurotrophic treatment. *Hearing Research*, *282*(1-2), 303–313. http://doi.org/10.1016/j.heares.2011.06.007

Lautermann, J., Crann, S. A., McLaren, J., Schacht, J., & Kruszka, P. (n.d.). Glutathione-dependent antioxidant systems in the mammalian inner ear: effects of aging, ototoxic drugs and noise. *Hearing Research*. http://doi.org/10.1016/S0378-5955(97)00154-8

Lefebvre, P. P., & Staecker, H. (2002). Steroid perfusion of the inner ear for sudden sensorineural hearing loss after failure of conventional therapy: a pilot study. *Acta Oto-Laryngologica*, *122*(7), 698–702.

Lenoir, M., & Puel, J. L. (1987). Dose-dependent changes in the rat cochlea following aminoglycoside intoxication. II. Histological study. *Hearing Research*, *26*(2), 199–209.

Li, H., & Steyger, P. S. (2011). Systemic aminoglycosides are trafficked via endolymph into cochlear hair cells. *Scientific Reports*, *1*, 159. http://doi.org/10.1038/srep00159

Lim, D. J. (1980). Cochlear anatomy related to cochlear micromechanics. A review. *The Journal of the Acoustical Society of America*, *67*(5), 1686–1695.

Lin, N. C., Fallah, E., Strimbu, C. E., Hendon, C. P., & Olson, E. S. (2019). Scanning optical coherence tomography probe for in vivo imaging and displacement measurements in the cochlea. *Biomedical Optics Express*, *10*(2), 1032. http://doi.org/10.1364/BOE.10.001032

Linder, T. E., Ma, F., & Huber, A. (2003). Round window atresia and its effect on sound transmission. *Otology & Neurotology*, *24*(2), 259–263.

Liu, G. S., Kim, J., Applegate, B. E., & Oghalai, J. S. (2017a). Computer-aided detection and quantification of endolymphatic hydrops within the mouse cochlea in vivo using optical coherence tomography. *Journal of Biomedical Optics*, *22*(7), 76002. http://doi.org/10.1117/1.JBO.22.7.076002

Liu, G. S., Zhu, M. H., Kim, J., Raphael, P., Applegate, B. E., & Oghalai, J. S. (2017b). ELHnet: a convolutional neural network for classifying cochlear endolymphatic hydrops imaged with optical coherence tomography. *Biomedical Optics Express*, *8*(10), 4579. http://doi.org/10.1364/BOE.8.004579

Liu, X., Zheng, G., Wu, Y., Shen, X., Jing, J., Yu, T., et al. (2013). NeuroToxicology Lead exposure results in hearing loss and disruption of the cochlear blood–labyrinth barrier and the protective role of iron supplement. *Neurotoxicology*, *39*, 173–181. http://doi.org/10.1016/j.neuro.2013.10.002

Lo, J., Campbell, L., Sale, P., Chambers, S., Hampson, A., Eastwood, H., & O'Leary, S. (2017a). The Role of Preoperative Steroids in Atraumatic Cochlear Implantation Surgery. *Otology & Neurotology*, *38*(8), 1118–1124. http://doi.org/10.1097/MAO.0000000000001505

Lo, J., Sale, P., Wijewickrema, S., Campbell, L., Eastwood, H., & O'Leary, S. J. (2017b). Defining the Hook Region Anatomy of the Guinea Pig Cochlea for Modeling of Inner Ear Surgery. *Otology & Neurotology*, *38*(6), e179–e187. http://doi.org/10.1097/MAO.0000000000001446

Lundman, L., Bagger-Sjoback, D., Holmquist, L., & Juhn, S. (1989). Round window membrane permeability. An in vitro model. *Acta Otolaryngol Suppl*, *457*, 73–77.

Mertz, J., & Kim, J. (2010). Scanning light-sheet microscopy in the whole mouse brain with HiLo background rejection. *Journal of Biomedical Optics*, *15*(1), 016027–7. http://doi.org/10.1117/1.3324890

Miller, J. M., Chi, D. H., O'Keeffe, L. J., Kruszka, P., Raphael, Y., & Altschuler, R. A. (n.d.). Neurotrophins can enhance spiral ganglion cell survival after inner hair cell loss. *The Laryngoscope*, *15*(4/5), 631–643. http://doi.org/10.1016/s0736-5748(96)00117-7

Mohebbi, S., Mirsalehi, M., Kahrs, L.-A., Ortmaier, T., Lenarz, T., & Majdani, O. (2017). Experimental Visualization of Labyrinthine Structure with Optical Coherence Tomography. *Iranian Journal of Otorhinolaryngology*, *29*(90), 5–9.

Morawski, K., Telischi, F. F., Merchant, F., Abiy, L. W., Lisowska, G., & Namyslowski, G. (2003). Role of mannitol in reducing postischemic changes in distortion-product otoacoustic emissions (DPOAEs): a rabbit

model. *The Laryngoscope*, *113*(9), 1615–1622. http://doi.org/10.1097/00005537-200309000-00039

Morsbach, F., Bickelhaupt, S., Wanner, G. A., Krauss, A., Schmidt, B., & Alkadhi, H. (2013a). Reduction of Metal Artifacts from Hip Prostheses on CT Images of the Pelvis: Value of Iterative Reconstructions. *Radiology*, *268*(1), 237–244. http://doi.org/10.1148/radiol.13122089

Morsbach, F., Wurnig, M., Kunz, D. M., Krauss, A., Schmidt, B., Kollias, S. S., & Alkadhi, H. (2013b). Metal artefact reduction from dental hardware in carotid CT angiography using iterative reconstructions. *European Radiology*, *23*(10), 2687–2694. http://doi.org/10.1007/s00330-013-2885-z

Mujica-Mota, M. A., Lehnert, S., Devic, S., Gasbarrino, K., & Daniel, S. J. (2014). Mechanisms of radiation-induced sensorineural hearing loss and radioprotection. *Hearing Research*, *312*(C), 60–68. http://doi.org/10.1016/j.heares.2014.03.003

Mukherjee, P., Uzun-Coruhlu, H., Curthoys, I. S., Jones, A. S., Bradshaw, A. P., & Pohl, D. V. (2011). Three-dimensional analysis of the vestibular end organs in relation to the stapes footplate and piston placement. *Otology & Neurotology*, *32*(3), 367–372. http://doi.org/10.1097/MAO.0b013e3182096ddd

Nadol, J. B. J., & Burgess, B. (1985). A study of postmortem autolysis in the human organ of Corti. *Journal of Comparative Neurology*, *237*(3), 333–342. http://doi.org/10.1002/cne.902370305

Naganawa, S., Yamazaki, M., Kawai, H., Bokura, K., Iida, T., Sone, M., & Nakashima, T. (2014). MR Imaging of Ménière's Disease after Combined Intratympanic and Intravenous Injection of Gadolinium using HYDROPS2. *Magnetic Resonance in Medical Sciences*, *13*(2), 133–137. http://doi.org/10.2463/mrms.2013-0061

Nageris, B. I., Attias, J., Shemesh, R., Hod, R., & Preis, M. (2012). Effect of cochlear window fixation on air- and bone-conduction thresholds. *Otology & Neurotology*, *33*(9), 1679–1684. http://doi.org/10.1097/MAO.0b013e31826dbabb

Nakashima, T., Naganawa, S., Pyykkö, I., Gibson, W. P. R., Sone, M., Nakata, S., & Teranishi, M. (2009). Grading of endolymphatic hydrops using magnetic resonance imaging. *Acta Oto-Laryngologica*, *129*(sup560), 5–8. http://doi.org/10.1080/00016480902729827

Neng, L., Zhang, F., Kachelmeier, A., & Shi, X. (2012). Endothelial Cell, Pericyte, and Perivascular Resident Macrophage-Type Melanocyte Interactions Regulate Cochlear Intrastrial Fluid–Blood Barrier Permeability. *Journal of the Association for Research in Otolaryngology*, *14*(2), 175–185. http://doi.org/10.1007/s10162-012-0365-9

Neng, L., Zhang, J., Yang, J., Zhang, F., Lopez, I. A., Dong, M., & Shi, X. (2015). Structural changes in thestrial blood–labyrinth barrier of aged C57BL/6 mice. *Cell and Tissue Research*, *361*(3), 685–696. http://doi.org/10.1007/s00441-015-2147-2

Nielson, A. J., & Griffith, W. P. (2017). Tissue fixation by osmium tetroxide. A possible role for proteins. *Journal of Histochemistry & Cytochemistry*, *27*(5), 997–999. http://doi.org/10.1177/27.5.479559

Nomura, Y., Hara, M., Funai, H., & Okuno, T. (1987). Endolymphatic hydrops in perilymphatic fistula. *Acta Oto-Laryngologica*, *103*(5-6), 469–476.

Nordang, L., Linder, B., & Anniko, M. (2003). Morphologic changes in round window membrane after topical hydrocortisone and dexamethasone treatment. *Otology & Neurotology*, *24*(2), 339–343.

Noushi, F., Richardson, R. T., Hardman, J., Clark, G., & O'Leary, S. (2005). Delivery of neurotrophin-3 to the cochlea using alginate beads. *Otology & Neurotology*, *26*(3), 528–533.

O'Leary, S. J., Monksfield, P., Kel, G., Connolly, T., Souter, M. A., Chang, A., Marovic, P., O'Leary, J. S., Richardson, R., & Eastwood, H. (2013a). Relations between cochlear histopathology and hearing loss in experimental cochlear implantation. *Hearing Research*, *298*(C), 27–35. http://doi.org/10.1016/j.heares.2013.01.012

O'Leary, S. J., Monksfield, P., Kel, G., Connolly, T., Souter, M. A., Chang, A., Marovic, P., O'Leary, J. S., Richardson, R., & Eastwood, H. (2013b). Relations between cochlear histopathology and hearing loss in experimental cochlear implantation. *Hearing Research*, *298*(C), 27–35. http://doi.org/10.1016/j.heares.2013.01.012

Ohinata, Y., Miller, J. M., Altschuler, R. A., & Schacht, J. (2000). Intense noise induces formation of vasoactive lipid peroxidation products in the cochlea. *Brain Research*, *878*(1-2), 163–173. http://doi.org/10.1016/s0006-8993(00)02733-5

Ohinata, Y., Yamasoba, T., Schacht, J., & Miller, J. M. (n.d.). Glutathione limits noise-induced hearing loss. *Hearing Research*, *146*(1-2), 28–34. http://doi.org/10.1016/S0378-5955(00)00096-4

Ohlemiller, K. K., Wright, J. S., & Dugan, L. L. (1999). Early elevation of cochlear reactive oxygen species following noise exposure. *Audiology and Neurotology*, *4*(5), 229–236. http://doi.org/10.1159/000013846

Osborne, M. P., & Comis, S. D. (1990). High resolution scanning electron microscopy of stereocilia in the cochlea of normal, postmortem, and drug-treated guinea pigs. *Journal of Electron Microscopy Technique*, *15*(3), 245–260. http://doi.org/10.1002/jemt.1060150305

Osborne, M. P., Comis, S. D., Johnson, A. P., & Jeffries, D. R. (1989). Post-mortem changes in hair bundles of the guinea pig and human cochlea studied by high-resolution scanning microscopy. *Acta Oto-Laryngologica*, *108*(3-4), 217–226.

Pau, H. W., Just, T., Bornitz, M., Lasurashvilli, N., & Zahnert, T. (2007). Noise Exposure of the Inner Ear During Drilling a Cochleostomy for Cochlear Implantation. *The Laryngoscope*, *117*(3), 535–540. http://doi.org/10.1097/MLG.0b013e31802f4169

Pierce, N. E., & Antonelli, P. J. (2012). Endolymphatic hydrops perspectives 2012. *Current Opinion in Otolaryngology & Head and Neck Surgery*, *20*(5), 416–419. http://doi.org/10.1097/MOO.0b013e328357a6c8

Piergallini, L., Scola, E., Tuscano, B., Brambilla, R., Campoleoni, M., Raimondi, G., et al. (2018). Flat-panel CT versus 128-slice CT in temporal bone imaging: Assessment of image quality and radiation dose. *European Journal of Radiology*, *106*, 106–113. http://doi.org/10.1016/j.ejrad.2018.07.013

Piu, F., Wang, X., Fernandez, R., Dellamary, L., Harrop, A., Ye, Q., et al. (2011). OTO-104: a sustained-release dexamethasone hydrogel for the treatment of otic disorders. *Otology & Neurotology*, *32*(1), 171–179. http://doi.org/10.1097/MAO.0b013e3182009d29

Plontke, S. K., Glien, A., Rahne, T., Mäder, K., & Salt, A. N. (2014). Controlled release dexamethasone implants in the round window niche for salvage treatment of idiopathic sudden sensorineural hearing loss. *Otology & Neurotology*, *35*(7), 1168–1171. http://doi.org/10.1097/MAO.0000000000000434

Plontke, S. K., Zimmermann, R., Zenner, H.-P., & Löwenheim, H. (2006). Technical note on microcatheter implantation for local inner ear drug delivery: surgical technique and safety aspects. *Otology & Neurotology*, *27*(7), 912–917. http://doi.org/10.1097/01.mao.0000235310.72442.4e

Postnov, A., Zarowski, A., De Clerck, N., Vanpoucke, F., Offeciers, F. E., Van Dyck, D., & Peeters, S. (2006). High resolution micro-CT scanning as an innovatory tool for evaluation of the surgical positioning of cochlear implant electrodes. *Acta Oto-Laryngologica*, *126*(5), 467–474. http://doi.org/10.1080/00016480500437377

Pyykkö, I., Nakashima, T., Yoshida, T., Zou, J., & Naganawa, S. (2013). Ménière's disease: a reappraisal supported by a variable latency of symptoms and the MRI visualisation of endolymphatic hydrops. *BMJ Open*, *3*(2), e001555–10. http://doi.org/10.1136/bmjopen-2012-001555

Pyykkö, I., Zou, J., Poe, D., Nakashima, T., & Naganawa, S. (2010). Magnetic resonance imaging of the inner ear in Meniere's disease. *Otolaryngologic*

Clinics of North America, *43*(5), 1059–1080. http://doi.org/10.1016/j.otc.2010.06.001

Ramamoorthy, S., Zhang, Y., Petrie, T., Chen, F., Subhash, H. M., Choudhury, N., et al. (2013). Measurement of in vivobasal-turn vibrations of the organ of Corti using phase-sensitive Fourier domain optical coherence tomography. In N. Kollias, B. Choi, H. Zeng, H. W. Kang, B. E. Knudsen, B. J. Wong, et al. (Eds.), (Vol. 8565, pp. 85651V–5). Presented at the SPIE BiOS, SPIE. http://doi.org/10.1117/12.2009260

Ramekers, D., Versnel, H., Strahl, S. B., Klis, S. F. L., & Grolman, W. (2015). Temporary Neurotrophin Treatment Prevents Deafness-Induced Auditory Nerve Degeneration and Preserves Function. *The Journal of Neuroscience*, *35*(36), 12331–12345. http://doi.org/10.1523/JNEUROSCI.0096-15.2015

Rask-Andersen, H., Bredberg, G., Lyttkens, L., & Lööf, G. (1981). The function of the endolymphatic duct--an experimental study using ionic lanthanum as a tracer: a preliminary report. *Annals of the New York Academy of Sciences*, *374*(1 Vestibular an), 11–19. http://doi.org/10.1111/j.1749-6632.1981.tb30855.x

Rawson, R. A. (1943). The binding of T-1824 and structurally related diazo dyes by the plasma proteins. *American Journal of Physiology*, *138*(5), 708–717. http://doi.org/10.1152/ajplegacy.1943.138.5.708

Reale, E., Luciano, L., Franke, K., Pannese, E., Wermbter, G., & Iurato, S. (1975). Intercellular junctions in the vascular stria and spiral ligament. *Journal of Ultrastructure Research*, *53*(3), 284–297. http://doi.org/10.1016/S0022-5320(75)80030-X

Robertson, D., & Paki, B. (2002). Role of L-type Ca2+ channels in transmitter release from mammalian inner hair cells. II. Single-neuron activity. *Journal of Neurophysiology*, *87*(6), 2734–2740. http://doi.org/10.1152/jn.2002.87.6.2734

Roland, J. T., Jr. (2005). A Model for Cochlear Implant Electrode Insertion and Force Evaluation: Results with a New Electrode Design and Insertion Technique. *The Laryngoscope*, *115*(8), 1325–1339. http://doi.org/10.1097/01.mlg.0000167993.05007.35

Rosowski, J. J., Songer, J. E., Nakajima, H. H., Brinsko, K. M., & Merchant, S. N. (2004). Clinical, experimental, and theoretical investigations of the effect of superior semicircular canal dehiscence on hearing mechanisms. *Otology & Neurotology*, *25*(3), 323–332. http://doi.org/10.1097/00129492-200405000-00021

Ross, M. D., Nuttall, A. L., & Wright, C. G. (1977). Horseradish peroxidase acute ototoxicity and the uptake and movement of the peroxidase in the

auditory system of the guinea pig. *Acta Oto-Laryngologica*, *84*(1-6), 187–201.

Rowe, D., Chambers, S., Hampson, A., Eastwood, H., Campbell, L., & O'Leary, S. (2016). Delayed low frequency hearing loss caused by cochlear implantation interventions via the round window but not cochleostomy. *Hearing Research*, *333*, 49–57. http://doi.org/10.1016/j.heares.2015.12.012

Ruhl, D. S., Hong, S. S., & Littlefield, P. D. (2013). Lessons learned in otologic surgery: 30 years of malpractice cases in the United States. *Otology & Neurotology*, *34*(7), 1173–1179. http://doi.org/10.1097/MAO.0b013e318298a8fb

Rutledge, L. J. (1969). Histologic study of the perfused human temporal bone. *The Laryngoscope*, *79*(12), 2104–2125. http://doi.org/10.1288/00005537-196912000-00006

Sakagami, M., Tomiyama, S., Fukazawa, K., Umemoto, M., & Kubo, T. (1995). Vascular permeability of the stria vascularis and morphology of the endolymphatic sac in two types of experimental endolymphatic hydrops. *Annals of Otology, Rhinology & Laryngology*, *104*(3), 210–217. http://doi.org/10.1177/000348949510400306

Salt, A. N. (2004). Acute endolymphatic hydrops generated by exposure of the ear to nontraumatic low-frequency tones. *Journal of the Association for Research in Otolaryngology*, *5*(2), 203–214. http://doi.org/10.1007/s10162-003-4032-z

Salt, A. N., Hartsock, J., Plontke, S., LeBel, C., & Piu, F. (2011). Distribution of dexamethasone and preservation of inner ear function following intratympanic delivery of a gel-based formulation. *Audiology & Neurotology*, *16*(5), 323–335. http://doi.org/10.1159/000322504

Santi, P. A. (2011). Light Sheet Fluorescence Microscopy. *Journal of Histochemistry & Cytochemistry*, *59*(2), 129–138. http://doi.org/10.1369/0022155410394857

Santi, P. A., Johnson, S. B., Hillenbrand, M., Grandpre, P. Z., Glass, T. J., & Leger, J. R. (2018). Thin-sheet laser imaging microscopy for optical sectioning of thick tissues. *Doi.org*, *46*(4), 287–294. http://doi.org/10.2144/000113087

Santos-Sacchi, J., & Marovitz, W. F. (1980). An evaluation of normal strial capillary transport using the electron-opaque tracers ferritin and iron dextran. *Acta Oto-Laryngologica*, *89*(1-2), 12–26.

Sato, E., Shick, H. E., Ransohoff, R. M., & Hirose, K. (2009). Expression of Fractalkine Receptor CX3CR1 on Cochlear Macrophages Influences Survival of Hair Cells Following Ototoxic Injury. *Journal of the Association*

for Research in Otolaryngology, *11*(2), 223–234. http://doi.org/10.1007/s10162-009-0198-3

Satoh, H., Firestein, G. S., Billings, P. B., Harris, J. P., & Keithley, E. M. (2003). Proinflammatory Cytokine Expression in the Endolymphatic Sac During Inner Ear Inflammation. *Journal of the Association for Research in Otolaryngology*, *4*(2), 139–147. http://doi.org/10.1007/s10162-002-3025-7

Schacht, P., Johnson, S. B., & Santi, P. A. (2010). Implementation of a continuous scanning procedure and a line scan camera for thin-sheet laser imaging microscopy. *Biomedical Optics Express*, *1*(2), 598–609. http://doi.org/10.1364/BOE.1.000598

Schmitz, H. M., Johnson, S. B., & Santi, P. A. (2014). Kanamycin-Furosemide Ototoxicity in the Mouse Cochlea. *Otolaryngology -- Head and Neck Surgery*, *150*(4), 666–672. http://doi.org/10.1177/0194599813519071

Schmutzhard, J., Kositz, C. H., Glueckert, R., Schmutzhard, E., Schrott-Fischer, A., & Lackner, P. (2012). Apoptosis of the fibrocytes type 1 in the spiral ligament and blood labyrinth barrier disturbance cause hearing impairment in murine cerebral malaria. *Malaria Journal*, *11*(1), 30. http://doi.org/10.1186/1475-2875-11-30

Schröter, T. J., Johnson, S. B., John, K., & Santi, P. A. (2012). Scanning thin-sheet laser imaging microscopy (sTSLIM) with structured illumination and HiLo background rejection. *Biomedical Optics Express*, *3*(1), 170–177. http://doi.org/10.1364/BOE.3.000170

Seo, Y. J., Kim, J., Choi, J. Y., & Lee, W. S. (2013). Visualization of endolymphatic hydrops and correlation with audio-vestibular functional testing in patients with definite Meniere's disease. *Auris Nasus Larynx*, *40*(2), 25–30. http://doi.org/10.1016/j.anl.2012.07.009

Sepehr, A., Djalilian, H. R., Chang, J. E., Chen, Z., & Wong, B. J. F. (2008). Optical Coherence Tomography of the Cochlea in the Porcine Model. *The Laryngoscope*, *118*(8), 1449–1451. http://doi.org/10.1097/MLG.0b013e318173dd6c

Shepherd, R. K., Clark, G. M., & Black, R. C. (1983). Chronic electrical stimulation of the auditory nerve in cats. Physiological and histopathological results. *Acta Oto-Laryngologica. Supplementum*, *399*, 19–31.

Shepherd, R. K., Coco, A., Epp, S. B., & Crook, J. M. (2005). Chronic depolarization enhances the trophic effects of brain-derived neurotrophic factor in rescuing auditory neurons following a sensorineural hearing loss. *The Journal of Comparative Neurology*, *486*(2), 145–158. http://doi.org/10.1002/cne.20564

Shimono, M., Teranishi, M., Yoshida, T., Kato, M., Sano, R., Otake, H., et al. (2013). Endolymphatic hydrops revealed by magnetic resonance imaging in patients with acute low-tone sensorineural hearing loss. *Otology & Neurotology*, *34*(7), 1241–1246. http://doi.org/10.1097/MAO.0b013e3182990e81

Silverstein, H., Arruda, J., Rosenberg, S. I., Deems, D., & Hester, T. O. (1999). Direct round window membrane application of gentamicin in the treatment of Meniere's disease. *Otolaryngology -- Head and Neck Surgery*, *120*(5), 649–655. http://doi.org/10.1053/hn.1999.v120.a91763

Sly, D. J., Campbell, L., Uschakov, A., Saief, S. T., Lam, M., & O'Leary, S. J. (2016). Applying Neurotrophins to the Round Window Rescues Auditory Function and Reduces Inner Hair Cell Synaptopathy After Noise-induced Hearing Loss. *Otology & Neurotology*, *37*(9), 1223–1230. http://doi.org/10.1097/MAO.0000000000001191

Sly, D. J., Hampson, A. J., Minter, R. L., Heffer, L. F., Li, J., Millard, R. E., et al. (2012). Brain-derived neurotrophic factor modulates auditory function in the hearing cochlea. *Journal of the Association for Research in Otolaryngology : JARO*, *13*(1), 1–16. http://doi.org/10.1007/s10162-011-0297-9

Smeds, H., Eastwood, H. T., Hampson, A. J., Sale, P., Campbell, L. J., Arhatari, B. D., et al. (2015). Endolymphatic hydrops is prevalent in the first weeks following cochlear implantation. *Hearing Research*, *327*(C), 48–57. http://doi.org/10.1016/j.heares.2015.04.017

Smith, L. P., Eshraghi, A. A., Whitley, D. E., Van De Water, T. R., & Balkany, T. J. (2009). Induction of localized cochlear hypothermia. *Acta Oto-Laryngologica*, *127*(3), 228–233. http://doi.org/10.1080/00016480600794487

Spicer, S. S., & Schulte, B. A. (1996). The fine structure of spiral ligament cells relates to ion return to the stria and varies with place-frequency. *Hearing Research*, *100*(1-2), 80–100. http://doi.org/10.1016/0378-5955(96)00106-2

Staecker, H., Galinovic-Schwartz, V., Liu, W., Lefebvre, P., Kopke, R., Malgrange, B., et al. (1996a). The role of the neurotrophins in maturation and maintenance of postnatal auditory innervation. *The American Journal of Otology*, *17*(3), 486–492.

Staecker, H., Kopke, R., Malgrange, B., Lefebvre, P., & Van De Water, T. R. (1996b). NT-3 and/or BDNF therapy prevents loss of auditory neurons following loss of hair cells. *NeuroReport*, *7*(4), 889–894.

Staecker, H., Van De Water, T. R., Lefebvre, P. P., Liu, W., Moghadassi, M., Galinovic-Schwartz, V., et al. (1996c). NGF, BDNF and NT-3 play unique roles in the in vitro development and patterning of innervation of the

mammalian inner ear. *Brain Research. Developmental Brain Research*, *92*(1), 49–60.

Steinke, H., & Wolff, W. (2001). A modified Spalteholz technique with preservation of the histology. *Annals of Anatomy*, *183*(1), 91–95. http://doi.org/10.1016/S0940-9602(01)80020-0

Subhash, H. M., Davila, V., Sun, H., Nguyen-Huynh, A. T., Nuttall, A. L., & Wang, R. K. (2010). Volumetric in vivo imaging of intracochlear microstructures in mice by high-speed spectral domain optical coherence tomography. *Journal of Biomedical Optics*, *15*(3), 036024. http://doi.org/10.1117/1.3456554.2

Sutherland, T. M., & Young, D. A. (1966). Increased permeability of the capillaries of the rat heart to plasma albumin with asphyxiation and with perfusion. *The Journal of Physiology*, *183*(1), 112–122.

Suzuki, M., Yamasoba, T., Ishibashi, T., Miller, J. M., & Kaga, K. (2002). Effect of noise exposure on blood-labyrinth barrier in guinea pigs. *Hearing Research*, *164*(1-2), 12–18.

Suzuki, T., Matsunami, T., Hisa, Y., Takata, K., Takamatsu, T., & Oyamada, M. (2008). Roles of gap junctions in glucose transport from glucose transporter 1-positive to -negative cells in the lateral wall of the rat cochlea. *Histochemistry and Cell Biology*, *131*(1), 89–102. http://doi.org/10.1007/s00418-008-0502-z

Tabuchi, K., Nishimura, B., Nakamagoe, M., Hayashi, K., Nakayama, M., & Hara, A. (2011). Ototoxicity: Mechanisms of Cochlear Impairment and its Prevention. *Current Medicinal Chemistry*, *18*(31), 4866–4871. http://doi.org/10.2174/092986711797535254

Tagaya, M., Yamazaki, M., Teranishi, M., Naganawa, S., Yoshida, T., Otake, H., et al. (2010). Endolymphatic hydrops and blood–labyrinth barrier in Ménière's disease. *Acta Oto-Laryngologica*, *131*(5), 474–479. http://doi.org/10.3109/00016489.2010.534114

Takahashi, T., Kimura, R. S., & Ewertson, H. W. (1970). The ultrastructure of the spiral ligament in the Rhesus monkey. *Acta Oto-Laryngologica*, *69*(1-6), 46–60.

Takano, S., Iguchi, H., Sakamoto, H., Yamane, H., & Anniko, M. (2013). Blockage pattern of longitudinal flow in Meniere's disease. *Acta Oto-Laryngologica*, *133*(7), 1–7. http://doi.org/10.3109/00016489.2013.771409

Takumida, M., Akagi, N., & Anniko, M. (2009). A new animal model for Ménière's disease. *Acta Oto-Laryngologica*, *128*(3), 263–271. http://doi.org/10.1080/00016480701497436

Tien, H.-C., & Linthicum, F. H., Jr. (2016). Histopathologic Changes in the Vestibule after Cochlear Implantation. *Otolaryngology -- Head and Neck Surgery*, *127*(4), 260–264. http://doi.org/10.1067/mhn.2002.128555

Tona, Y., Sakamoto, T., Nakagawa, T., Adachi, T., Taniguchi, M., Torii, H., et al. (2014). In vivo imaging of mouse cochlea by optical coherence tomography. *Otology & Neurotology*, *35*(2), e84–9. http://doi.org/10.1097/MAO.0000000000000252

Tsuji, J., & Liberman, M. C. (1997). Intracellular labeling of auditory nerve fibers in guinea pig: central and peripheral projections. *The Journal of Comparative Neurology*, *381*(2), 188–202.

Uzun, H., Curthoys, I. S., & Jones, A. S. (2009). A new approach to visualizing the membranous structures of the inner ear – high resolution X-ray micro-tomography. *Acta Oto-Laryngologica*, *127*(6), 568–573. http://doi.org/10.1080/00016480600951509

Vanspauwen, R., Salembier, L., van den Hauwe, L., Parizel, P., Wuyts, F. L., & Van de Heyning, P. H. (2006). Posterior semicircular canal dehiscence: value of VEMP and multidetector CT. *B-Ent*, *2*(3), 141–145.

Verbist, B. M., Skinner, M. W., Cohen, L. T., Leake, P. A., James, C., Boex, C., et al. (2010). Consensus Panel on a Cochlear Coordinate System Applicable in Histologic, Physiologic, and Radiologic Studies of the Human Cochlea. *Otology & Neurotology*, *31*(5), 722–730. http://doi.org/10.1097/MAO.0b013e3181d279e0

Vivero, R. J., Joseph, D. E., Angeli, S., He, J., Chen, S., Eshraghi, A. A., et al. (2008). Dexamethasone Base Conserves Hearing from Electrode Trauma-Induced Hearing Loss. *The Laryngoscope*, *118*(11), 2028–2035. http://doi.org/10.1097/MLG.0b013e31818173ec

Vlajkovic, S. M., Lin, S. C.-Y., Wong, A. C. Y., Wackrow, B., & Thorne, P. R. (2013). Noise-induced changes in expression levels of NADPH oxidases in the cochlea. *Hearing Research*, *304*(c), 145–152. http://doi.org/10.1016/j.heares.2013.07.012

Voie, A. H. (2001). Imaging the intact guinea pig tympanic bulla by orthogonal-plane fluorescence optical sectioning microscopy. *Hearing Research*, *171*(1), 119–128. http://doi.org/10.1016/S0378-5955(02)00493-8

Wada, H., Sugawara, M., Kobayashi, T., Hozawa, K., & Takasaka, T. (1998). Measurement of guinea pig basilar membrane using computer-aided three-dimensional reconstruction system. *Hearing Research*, *120*(1-2), 1–6. http://doi.org/10.1016/s0378-5955(98)00007-0

Wagner, N., Cayé Thomasen, P., Laurell, G., Bagger-Sjöbäck, D., & Thomsen, J. (2005). Cochlear hair cell loss in single-dose versus

continuous round window administration of gentamicin. *Acta Oto-Laryngologica*, *125*(4), 340–345. http://doi.org/10.1080/00016480510026881

Wan, G., Gómez-Casati, M. E., Gigliello, A. R., Liberman, M. C., & Corfas, G. (2014). Neurotrophin-3 regulates ribbon synapse density in the cochlea and induces synapse regeneration after acoustic trauma. *eLife*, *3*, 1479. http://doi.org/10.7554/eLife.03564

Wang, H., Yin, S., Yu, Z., Huang, Y., & Wang, J. (2011). Dynamic changes in hair cell stereocilia and cochlear transduction after noise exposure. *Biochemical and Biophysical Research Communications*, *409*(4), 616–621. http://doi.org/10.1016/j.bbrc.2011.05.049

Warmerdam, T. J., Schröder, F. H. H. J., Wit, H. P., & Albers, F. W. J. (2003). Perilymphatic and endolymphatic pressures during endolymphatic hydrops. *European Archives of Oto-Rhino-Laryngology*, *260*(1), 9–11. http://doi.org/10.1007/s00405-002-0518-2

Weber, M., & Huisken, J. (2011). Light sheet microscopy for real-time developmental biology. *Current Opinion in Genetics & Development*, *21*(5), 566–572. http://doi.org/10.1016/j.gde.2011.09.009

Wimmer, W., Bell, B., Huth, M. E., Weisstanner, C., Gerber, N., Kompis, M., et al. (2014). Cone beam and micro-computed tomography validation of manual array insertion for minimally invasive cochlear implantation. *Audiology & Neurotology*, *19*(1), 22–30. http://doi.org/10.1159/000356165

Winther, F. O. (1971). The permeability of the guinea pig cochlear capillaries to horseradish peroxidase. *Zeitschrift Für Zellforschung Und Mikroskopische Anatomie (Vienna, Austria : 1948)*, *114*(2), 193–202.

Wong, B. (2004). Imaging the internal structure of the rat cochlea using optical coherence tomography at 0.827 µm and 1.3 µm. *Otolaryngology -- Head and Neck Surgery*, *130*(3), 334–338. http://doi.org/10.1016/j.otohns.2003.11.007

Wong, B. J. F., de Boer, J. F., Park, B. H., Chen, Z., & Nelson, J. S. (2000). Optical coherence tomography of the rat cochlea. *Journal of Biomedical Optics*, *5*(4), 367–370. http://doi.org/10.1117/1.1310165

Wright, A. (1980). Scanning electron microscopy of the human cochlea--postmortem autolysis artefacts. *Archives of Otorhinolaryngology*, *228*(1), 1–6.

Xenellis, J. E., Linthicum, F. H., Jr, Webster, P., & Lopez, R. (2004). Basilar Membrane Displacement Related to Endolymphatic Sac Volume. *The Laryngoscope*, *114*(11), 1953–1959. http://doi.org/10.1097/01.mlg.0000147927.98766.e1

Xu, Q., Qaum, T., & Adamis, A. P. (2001). Sensitive blood-retinal barrier breakdown quantitation using Evans blue. *Investigative Ophthalmology & Visual Science*, *42*(3), 789–794.

Yamane, H., Iguchi, H., Konishi, K., Sakamaoto, H., Wada, T., Fujioka, T., et al. (2014). Three-dimensional cone beam computed tomography imaging of the membranous labyrinth in patients with Meniere's disease. *Acta Oto-Laryngologica*, *134*(09-10), 000–000. http://doi.org/10.3109/00016489.2014.913315

Yamane, H., Takayama, M., Sunami, K., Sakamoto, H., Imoto, T., & Anniko, M. (2010). Blockage of reuniting duct in Meniere's disease. *Acta Oto-Laryngologica*, *130*(2), 233–239. http://doi.org/10.3109/00016480903096648

Zhang, F., Dai, M., Neng, L., Zhang, J. H., Zhi, Z., Fridberger, A., & Shi, X. (2013a). Perivascular macrophage-like melanocyte responsiveness to acoustic trauma—a salient feature of strial barrier associated hearing loss. *The FASEB Journal*, *27*(9), 3730–3740. http://doi.org/10.1096/fj.13-232892

Zhang, F., Zhang, J., Neng, L., & Shi, X. (2013b). Characterization and Inflammatory Response of Perivascular-Resident Macrophage-Like Melanocytes in the Vestibular System. *Journal of the Association for Research in Otolaryngology : JARO*, *14*(5), 635–643. http://doi.org/10.1007/s10162-013-0403-2

Zhang, J., Chen, S., Hou, Z., Cai, J., Dong, M., & Shi, X. (2015). Lipopolysaccharide-induced middle ear inflammation disrupts the cochlear intra-strial fluid-blood barrier through down-regulation of tight junction proteins. *PLoS ONE*, *10*(3), e0122572–20. http://doi.org/10.1371/journal.pone.0122572

Zhang, S. Y., Robertson, D., Yates, G., & Everett, A. (1999). Role of L-type Ca(2+) channels in transmitter release from mammalian inner hair cells I. Gross sound-evoked potentials. *Journal of Neurophysiology*, *82*(6), 3307–3315. http://doi.org/10.1152/jn.1999.82.6.3307

Zou, J., Poe, D., Bjelke, B., & Pyykkö, I. (2009). Visualization of inner ear disorders with MRI in vivo: from animal models to human application. *Acta Oto-Laryngologica*, *129*(sup560), 22–31. http://doi.org/10.1080/00016480902729850

Zou, J., Pyykkö, I., Bretlau, P., Klason, T., & Bjelke, B. (2003). In vivo visualization of endolymphatic hydrops in guinea pigs: magnetic resonance imaging evaluation at 4.7 tesla. *Annals of Otology, Rhinology & Laryngology*, *112*(12), 1059–1065. http://doi.org/10.1177/000348940311201212